SHAPING, TUNING, AND PLAYING NANODRUMS: TOWARDS SCALABLE AND HIGH QUALITY FACTOR GRAPHENE NANOELECTROMECHANICAL SYSTEMS

by

DAVID JOSEPH MILLER

A DISSERTATION

Presented to the Department of Physics
and the Graduate School of the University of Oregon
in partial fulfillment of the requirements
for the degree of
Doctor of Philosophy

June 2020

DISSERTATION APPROVAL PAGE

Student: David Joseph Miller

Title: Shaping, Tuning, and Playing Nanodrums: Towards Scalable and High Quality Factor Graphene Nanoelectromechanical Systems

This dissertation has been accepted and approved in partial fulfillment of the requirements for the Doctor of Philosophy degree in the Department of Physics by:

Brian Smith	Chairperson
Benjamín Alemán	Advisor
Hailin Wang	Core Member
Mark Lonergan	Institutional Representative

and

Kate Mondloch	Interim Vice Provost and Dean of the Graduate School

Original approval signatures are on file with the University of Oregon Graduate School.

Degree awarded June 2020

DISSERTATION ABSTRACT

David Joseph Miller

Doctor of Philosophy

Department of Physics

June 2020

Title: Shaping, Tuning, and Playing Nanodrums: Towards Scalable and High Quality Factor Graphene Nanoelectromechanical Systems.

Nanomechanical systems (NEMS) are some of humankinds most exquisite sensors of mass and force and have enabled the transduction of physical phenomena down to the single-phonon level. Despite incredible progress on the overall properties of mechanical resonators, development of large-scale arrays is only now beginning to be explored. Such arrays could be transformative in basic science, allowing for realization of topological metamaterials and studies of networks, and for applied devices, such as next-generation mass spectrometers and thermal imaging cameras. To make a NEMS array viable for these applications however, each NEMS device must have several desirable properties. First, all devices must have high mechanical quality factors (Q) combined with low mass, for high sensitivity. This requires both a fundamental knowledge of the origin of mechanical dissipation and viable engineering methods to maximize the Q for a given mass. Second, devices must have scalable control methods for tuning the frequency and exciting motion. No such devices that meet these requirements exist today and applications for NEMS arrays remain limited.

Graphene NEMS have the potential to meet these needs, if some fundamental challenges can be addressed. Although graphene NEMS have low mass, they also have a

relatively low Q. Furthermore, engineering methods to modify the shape of graphene NEMS are limited, making it difficult to tune and enhance their properties. Finally, like all other NEMS, tuning and control methods that scale to large arrays are sorely lacking.

In this work, we will begin to address these needs in graphene NEMS through a compendium of studies. We will first use shape engineering to enhance the properties of graphene NEMS. Then, we will present a detailed study of the Q and demonstrate methods to enhance it. Finally, we will study actuation and control methods for graphene NEMS, including demonstration of an electo-optic method that is truly scalable. Together, these studies pave the way for future work on large-scale arrays of NEMS.

This dissertation includes previously published and unpublished co-authored material.

CURRICULUM VITAE

NAME OF AUTHOR: David Joseph Miller

GRADUATE AND UNDERGRADUATE SCHOOLS ATTENDED:

University of Oregon, Eugene, OR
California Polytechnic State University, San Luis Obispo, CA

DEGREES AWARDED:

Doctor of Philosophy, Physics, 2020, University of Oregon
Masters of Science, Physics, 2020, University of Oregon
Bachelor of Science, Physics, 2013, California Polytechnic State University

AREAS OF SPECIAL INTEREST:

Nanotechnology
Nanoelectromechanical systems (NEMS)
Nanofabrication
Instrumentation

PROFESSIONAL EXPERIENCE:

Graduate Research Assistant, Alemán Lab, University of Oregon, Eugene, Oregon, 2014-2020

Graduate Teaching Fellow, Department of Physics, University of Oregon, Eugene, 2013-14

GRANTS, AWARDS, AND HONORS:

OMQ Emanuel Scholarship, 2020

Best student talk, OMQ Fall Symposium, 2019

Special OPPS Travel and Research Award, 2019

Best Student talk, Pacific Northwest Optics Conference, 2017

Weiser Qualifier Exam Prize, 2014

PUBLICATIONS:

Miller, D., Blaikie, A. & Alemán, B. J. Nonvolatile Rewritable Frequency Tuning of a Nanoelectromechanical Resonator Using Photoinduced Doping. *Nano Lett.* **20**, 2378-2386 (2020)

Miller, D. & Alemán, B. Spatially resolved optical excitation of mechanical modes in graphene NEMS. *Appl. Phys. Lett.* **115**, 193102 (2019)

Blaikie, A., Miller, D. & Alemán, B. J. A fast and sensitive room-temperature graphene nanomechanical bolometer. *Nat. Commun.* **10**, 4726 (2019)

Ziegler, J., Klaiss, R., Blaikie, A., Miller, D., Horowitz, V. R. & Alemán, B. J. Deterministic Quantum Emitter Formation in Hexagonal Boron Nitride via Controlled Edge Creation. *Nano Lett.* **19**, 2121–2127 (2019)

Miller, D., Blaikie, A., Carter, B. & Aleman, B. Engineering the Modal Shape of Graphene Nanoelectromechanical Systems Using Focused Ion Beam Milling. *2018 IEEE 13th Nanotechnol. Mater. Devices Conf.* 1–4 (2018)

Leonhardt, E. J., Van Raden, J. M., Miller, D., Zakharov, L. N., Alemán, B. & Jasti, R. A Bottom-Up Approach to Solution-Processed, Atomically Precise Graphitic Cylinders on Graphite. *Nano Lett.* **18**, 7991–7997 (2018)

Ziegler, J., Blaikie, A., Fathalizadeh, A., Miller, D., Yasin, F. S., Williams, K., Mohrhardt, J., McMorran, B. J., Zettl, A. & Alemán, B. Single-Photon Emitters in Boron Nitride Nanococoons. *Nano Lett.* **18**, 2683–2688 (2018)

Miller, D. & Alemán, B. Shape tailoring to enhance and tune the properties of graphene nanomechanical resonators. *2D Mater.* **4**, (2017)

Alduino, C. *et. al.* CUORE-0 detector: Design, construction and operation. *J. Instrum.* **11**, (2016)

ACKNOWLEDGMENTS

First and foremost, I would like to thank my advisor Professor Benjamín Alemán for guiding me through the journey that is a Physics Ph.D. Your knowledge of science and writing enabled me to grow as a scientist and it has been a pleasure being one of your first graduate students. Also thanks to my undergraduate mentors, Professor Thomas Gutierrez at Cal Poly SLO and Professor Stuart Freedman at UC Berkeley, who got me started on thinking about physics graduate school.

My labmates throughout this time have been instrumental in keeping me sane and helping me do good science. Andrew, Josh, Kara, Rudy, Rachael, and Brittany, you all made coming to work something I looked forward to at least most days. I can't imagine having better colleagues.

Much of this work was supported by the staff of the TSA. Cliff Dax, John Boosinger, and Kris Johnson especially were always extremely generous with their time and helped me immensely building various scientific apparatus. The nanodrums studied in this work were all made and characterized in CAMCOR and would not be possible without many excellent staff members. I especially want to thank Kurt Langworthy. It was always a pleasure chatting with you while you distracted me from my SEM time, whether it was about what tools were down or our latest plans outdoors.

The friends I've made during grad school have made the last 2,434 days (but who's counting?) some of the most fulfilling of my life. I don't know how I would have survived my first year without the Binney crew of Ben, Kentaro, John, Savannah, Jordan, Andy, and Fehmi, among others. To the permanent members of the Farmhouse, Caleb, Julian, and Ian. We've had too many great times to even try to recount specific time. Suffice to say, the

Farmhouse has felt like home for the last 6 years and our time together will stick with me throughout my life. Finally, thanks to all the friends I've skied, biked, climbed, backpacked, and done all sorts of outdoors shenanigans with. I cannot wait to continue scaling mountains and ripping down hills with all you.

This journey to a Ph.D. would not have been possible with loving and inspiring parents. Mom and Dad, thank you for always being there to support me, before, during, and after my time at UO. Finally, thank you to my wonderful partner and adventure buddy Anna. You've been with me for all the work in this dissertation and at least some of it belongs to you. Thank you for all the love and support you've given me over the years.

TABLE OF CONTENTS

Chapter Page

Chapter Page

Chapter Page

Chapter Page

LIST OF FIGURES

Figure Page

Figure Page

Figure Page

CHAPTER I

INTRODUCTION

1.1 Historical Perspective

Figure 1.1: Mechanical systems throughout history. (a) Bronze gear fragment recovered from the ancient Greek Antikythera mechanism*. (b) Diagram of a pendulum clock†. (c) Partially completed piece of Charles Babbages' analytical engine‡.

Mechanical systems have existed at the cutting edge of science and technology for millennia. The ancient Greek Antikythera mechanism(1), dating to the 2nd century BC, used a complex mechanism of bronze gears to predict astronomical phenomena and is considered to be the first analog computer. Mechanical clocks improved the accuracy of timekeeping from 15 minutes to 15 seconds, an improvement by almost

*The Antikythera mechanism (Fragment A – front); visible is the largest gear in the mechanism, approximately 14 centimetres (5.5 in) in diameter, by Marsyas, Wikipedia, is licensed under CC BY 2.5

† The first pendulum clock, invented by Christiaan Huygens in 1656, by Christiaan Huygens, Wikipedia, Public Domain

‡Trial model of a part of the Analytical Engine, built by Babbage, as displayed at the Science Museum (London), by Bruno Barral, Wikipedia, is licensed under CC BY-SA 2.5

two-orders of magnitude, ushering in the era of precision timekeeping. More recently, a wide assortment of mechanical computing devices emerged near the turn of the 20th century including Charles Babbage's analytical engine, considered to be the first design of a general-purpose computer(2). On the scientific side, Einstein and de Haas(3) used a suspended slug of ferromagnetic material driven at its mechanical resonance frequency to confirm Ampère's hypothesis that magnetism arises from circulating charge.

Like the pendulum clock and the Einstein de Haas experiment, a large subset of mechanical systems are based on mechanical resonance. In the simplified description of mechanical resonator, a freely suspended element with mass m and spring constant k has a natural frequency $\omega_0 \approx \sqrt{k/m}$. The dissipation of the system is given by the parameter β, which is the exponential time-constant giving the damping rate of an undriven oscillator. A key figure of merit is the quality factor, defined as a ratio of the stored energy (W) to the energy lost (ΔW) for every oscillation cycle, $Q = 2\pi \frac{W}{\Delta W} \approx \frac{\omega_0}{2\beta}$. Across nearly all mechanical resonators, with dimensions ranging from the nanoscale ($Volume \sim 10^{-21}$ m^3) to the macroscale(4) ($Volume \sim 10$ m^3), the goal is to measure a perturbation on the dynamics of the oscillator before it decoheres and correlate this perturbation to a some physical phenomena. This perturbation could be an added mass(5) (the basis for nanomechanical mass spectrometry) a force gradient (leading to various types of atomic force microscopy such as electric force microscopy(6)), or coupling to external or internal degrees of freedom(7) (such as a neighboring resonator). The indiscriminate response of the mechanical resonator to these perturbations is best illustrated in their use to detect fundamental physics in vastly different domains. For example mechanical resonators have been used both in experiments measuring quantum fluctuations(8) and gravitational waves from

astronomical[§] sources(4). Some recent theoretical proposals have even suggested that entangled mechanical resonators held in a gravitational field could be used to study quantum gravity(9), which remains an open question in theoretical physics.

As a result of the silicon revolution and the associated planar device processing techniques, mechanical systems have been fabricated in increasingly diminutive sizes. These so-called microelectromechanical systems (MEMS) are extremely low mass and thus respond strongly to extremely small perturbations. Furthermore, due to their small size, they require low power to operate and are robust against large g-forces. These properties have allowed MEMS to become ubiquitous in many applications that power modern technology. Some examples include airbag sensors, gyroscopes, and timing chips, among others(10).

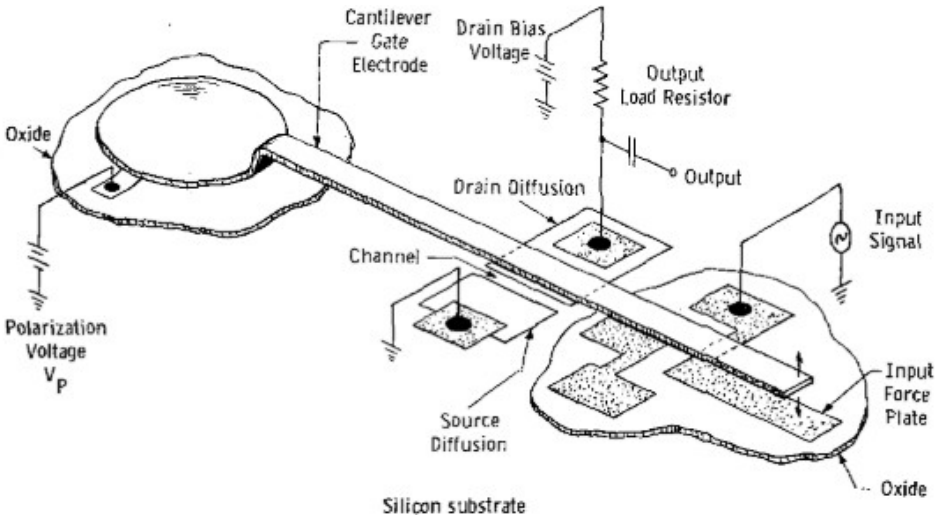

Figure 1.2: Diagram of the resonant gate transistor, an early MEMS device, taken from(11).

Likewise, resonant MEMS have proven to be highly powerful instruments. The first example of these was the resonant gate transistor (RGT), invented in 1964 by Harvey

[§]Despite his claims, Jospeh Weber's attempts at resonant detection of gravitational waves were a failure. In 2017, LIGO successfully detected gravitation waves. Although the test mirrors in the LIGO interferometers are ultra-high quality factor mechanical resonators, the detection mechanism itself does not rely on mechanical resonance.

Nathanson and coworkers, where a cantilevered metallic beam acted as the gate electrode in a field-effect transistor(11) (See Figure 1.2). The cantilever was held at a bias voltage ($V_{\%\&}$) some distance (d) over a microfabricated field effect transistor, with $V_{\%\&}$ and d determining the conductance in the channel. An input periodic signal ($V_{/\&}$) with frequency ω was coupled to the cantilever through a metallic electrode at the tip. $V_{/\&}$ induced mechanical vibrations at frequency ω, which are only large when ω is resonant with the cantilever's mechanical resonance frequency ($f_{\$}$). These vibrations modulated the gate voltage in the field-effect transistor and thus the output current. Varying $V_{\%\&}$ allowed a small amount of tuning of $f_{\$}$ to control the center frequency of the passband. This system was proposed as an extremely sensitive (for the time) bandpass filter, with the width and location passband determined by the frequency and quality factor of the cantilever.

With remarkable prescience, the inventors of the original RGT identified two crucial problems that had to be overcome for broader adoption, which continue to plague microscopic mechanical resonators today:

1. **Control and enhancement of the mechanical quality factor:** The Q determined the width and selectivity of the passband in the RGT and increasing it would allow for highly selective filters.
2. **Control of f_0:** Variability in $f_{\$}$ of the microfabricated beams limits the yield in arrays of RGTs. Although $V_{\%\&}$ can be used to fine-tune $f_{\$}$. A separate voltage source is required for each beam, limiting scalability.

The field of MEMS has advanced significantly since the demonstration of the RGT. This is perhaps best illustrated by the atomic force microscope(12) (AFM), which uses a tiny cantilever driven on resonance to create a topographic map of a surface. Modern AFMs are sensitive enough to image the double-helix structure of DNA(13) or even molecular structures(14). Advanced nanofabrication techniques have allowed the dimensions of MEMS to be pushed even deeper into the nanoscale. Nanoelectromechanical systems(15) (NEMS) represent a further evolution of MEMS and have had a wide-ranging scientific impact. Such tiny devices have enabled studies

of macroscopic quantum mechanics(16), mass sensing(17), and ultra-high resolution magnetic imaging(18). On the extreme end of downsized mechanical resonators are low-dimensional materials, such as suspended carbon nanotubes(19) and graphene sheets(20). These “atomic-scale” devices represent the ultimate limit of how small a mechanical resonator can be made.

Much like their nanoelectronic counterparts, the power of NEMS rapidly grows as the number of devices is scaled up to large arrays(21). Such large device arrays are extremely interesting from both a fundamental and applied perspective. On the applied side, resonant sensing benefits greatly from large arrays. For example, in NEMS neutral-particle mass spectrometry(22) (NEMS-MS), neutral analytes are adsorbed by a NEMS device, which changes its frequency. This change in frequency can be correlated with the adsorbed mass, allowing for an exquisitely sensitive scale that can detect neutral particles, unlike traditional mass spectrometry. Although a single NEMS-based mass sensor is powerful(17), arrays have similarly excellent mass sensitivities but much larger cross-sectional areas, greatly increasing the throughput of NEMS-MS.

Another sensing technique that could potentially be revolutionized with NEMS is thermal infrared imaging. In traditional thermal sensors, called microbolometers, thermal (i.e. 8-12 μm) light changes the resistance in a thermally isolated suspended structure(23). Sensitive measurement of this resistance change allows for an image to be formed by measuring the resistance change in all devices (which can be 1024×1024 in modern microbolometer arrays). These traditional microbolometers have fundamental limitations when it comes to their bandwidth (~60 Hz) and temperature-of-operation (around room-temperature). A NEMS approach, similar to mass sensing, correlates incident radiation with a thermally induced change in the resonance frequency of a device(24). Such devices would be much more robust to extra heating and could operate at much faster speeds.

On the more fundamental side, NEMS arrays are interesting for studies of non-linear physics and synchronized oscillators. Even small NEMS arrays with local coupling have been shown to have highly exotic states(25). By scaling up such small coupled arrays, it could be possible to model highly-synchronized networks, such as those seen in complex biological systems like the brain(26).

For continued evolution of NEMS arrays, the same challenges previously identified by the inventers of the resonant gate transistor must be met. Mainly, we would like very high-Q NEMS with a controllable frequency capability. The high-Q increases the overall sensitivity of a device. It also increases the number of devices that can be multiplexed, for easier readout(27). A controllable frequency allows for the initial state of a device to be set and allows for tunable coupling between devices in a nanomechanical network. It is also highly important to be able to tune the frequency to offset fabrication imperfections(28). Furthermore, it is highly desirable such devices have a low mass and a large surface-volume ratio, since these increase the capture cross section, the minimum pixel size, the thermal mass, and the degree of non-linear coupling(29) between neighboring resonators. Despite their promise, NEMS arrays are still in their infancy and applications are limited. This is due to a lack of systems which simultaneously meet all the needs identified above. In this work, we will demonstrate progress towards achieving NEMS arrays using graphene NEMS, which we show could have the desirable combination of low-mass, high-Q, and programmable frequency.

1.2 Modern NEMS and the Pursuit of Low Mass and High Q

As described above, high-Q and low mass is desirable across a range of NEMS application and the simultaneous pursuit of low-mass and a high mechanical quality factor has driven the field of NEMS in recent years. Both of these quantities are important across a wide range of applications. A low mass reduces the inertia in the mechanical systems, increasing its sensitivity to small perturbations due to external forces(18, 30, 31) or masses(22, 27, 32, 33). Meanwhile, a high Q protects these perturbations from decoherence, making them easier to detect. This is reflected in

the expressions for the minimum detectable mass of a mechanical resonator, $\delta m_{min} \propto \frac{k_B T}{\omega^2 x_{max}}$ where m is the resonator mass, and the thermal-noise limited minimum detectable force, $\delta F_{min} = \sqrt{8\pi k_B T m_{eff} f_0 / Q}$, where T is the temperature, m_{eff} is the effective mass of the mode(14), and k_B is Boltzmann's constant. Both these expressions require high Q and low mass to reach the highest sensitivity(14). Furthermore, both these quantities are of crucial importance as mechanical systems are increasingly studied in the realm of quantum mechanics. For example, the zero-point motion of an oscillator(34) is given by $z_{zpf} = \sqrt{\hbar Q / (2\pi m f_0)}$ while the number of coherent oscillations(35) is $N = Q f_0 \hbar / k_B T$.

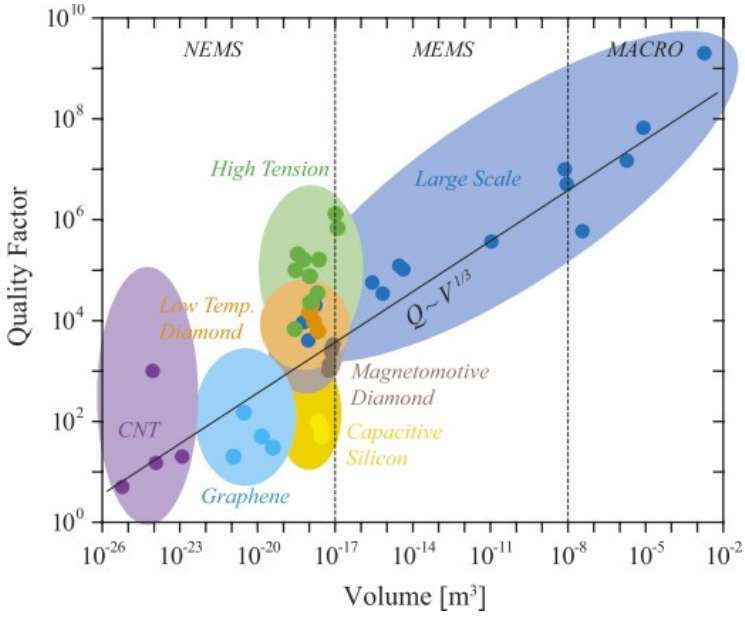

Figure 1.3: Quality factor vs. device volume, taken from(36)

A major limitation in these goals is a heuristic volumetric dependence of $Q \sim V^{-2/3}$ (or $Q \sim m^{-2/3}$) (shown in Figure 1.3) that has been observed over a wide range of length scales and materials(36). As such, the highest mechanical quality factors have typically been achieved in large, macroscopic mechanical resonators, which have extremely large masses. A significant exception to this trend comes in the form of

high-tension silicon-nitride (SiN) strings and membranes. First demonstrated in 2006(37), high-tension SiN strings can have Q's of a few-hundred thousand, several orders-of-magnitude higher than other similarly sized NEMS devices.

Since this initial work, the theory of dissipation dilution(38, 39) (DDT) has emerged to describe the origin of the high Q in SiN NEMS. In essence, DDT notices that although the vast majority of elastic energy is stored in the lossless elongational potential energy, the bending potential energy is lossy and leads to dissipation. This means that increasing the elongational energy, through either stress or large sizes, or reducing the bending energy via reduced thickness, can lead to exceptionally high Q. To date, the highest recording quality factors in NEMS of $Q \sim 10^{9} - 10^{10}$ have occurred in heavily engineered SiN devices(34, 35, 40, 41), making these the most promising candidates for high-resolution sensing(30) and studies of quantum nanomechanics(42). Still, these devices are much larger (mm-scale) and heavier than atomic-scale NEMS, making them infeasible for arrays.

In stark contrast are low-dimensional materials, such as 1D carbon nanotubes(19) and 2D graphene sheets(20). Such devices have femtogram masses typically have lateral dimensions <10 μm. However, these devices have extremely low quality factors of $10^{6} - 10^{7}$ compared to other $Q > 10^{8}$ for other NEMS devices(36) and $Q > 10^{10}$ for SiN NEMS, which greatly limits the promise of low-dimensional NEMS. Still, graphene has many desirable properties making it worthwhile to study and exceptionally exciting if the Q can be improved. For example, 2D NEMS have area mass densities 100 times lower than SiN, increasing the ultimate sensitivity in mass and force sensing. Furthermore, graphene is an excellent electrical conductor(43), making NEMS feasible without extra metallization, as is the case with SiN NEMS(44).

1.3 Graphene NEMS

Graphene, a two-dimensional layer of carbon atoms, has energized the field of physics since its isolation in 2004(43). This is due to a unique set of high electrical and thermal conductivity(43, 45–47), high mechanical strength(48, 49), relatively high

and broadband optical absorption(50), in addition to many others. This combination of properties has made graphene desirable as the motional element in NEMS. The first realization of a graphene NEMS occurred in 2007 when Bunch and coworkers(51) exfoliated graphene sheets over trenches etched into SiO_2 (See Figure 1.4). The devices were actuated with both optical and electronic methods and transduced using optical interferometry. These graphene NEMS had resonance frequencies in the tens of MHz and importantly, the resonance frequency could be tuned by several-hundred percent, significantly more than in other NEMS materials(52).

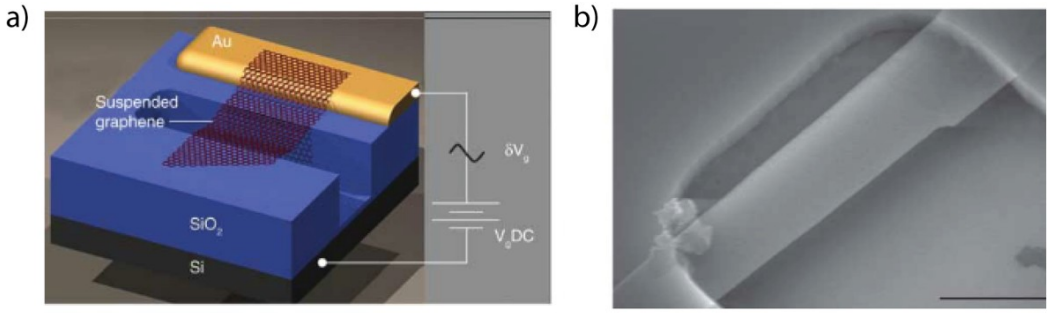

Figure 1.4: Early graphene NEMS. (a) Diagram of electrically connected graphene NEMS suspended over a trench. (b) SEM image of a graphene flake suspended over a cavity etched into SiO_2. Both images are taken from(20).

Following the demonstration of chemical vapor deposition (CVD) growth of graphene on copper foil(53), Van der Zande and co-workers demonstrated large-scale arrays of CVD graphene NEMS(54), including square drumheads and lithographically defined beams. These devices showed remarkably higher quality factors at 10 K, 10^+ times higher than the room-temperature values of the Q. Since these initial studies, the graphene NEMS community has sub-divided into groups primarily focused on studying fundamental nanoscale physics at low temperatures and those studying the applications and properties of room-temperature graphene NEMS.

The pursuit of graphene NEMS at low temperatures has been lucrative. Cooling to the millikelvin regime allows for capacitive coupling to superconducting cavities for transduction(55, 56), allowing for ultra-sensitive readout of mechanical motion. Furthermore, graphene NEMS can have quality factors exceeding 10^6 at cryogenic

temperatures of ~10 mK(57), allowing for studies of non-linear dissipation mechanisms(57, 58). Despite these advances, several open questions and challenges remain, including what drives the high-quality factor at cryogenic temperature in graphene NEMS.

Room-temperature studies of graphene NEMS on the other hand have been primarily concerned with elucidating the properties of the ultra-thin sheets and readying them for technological applications(46, 59–61). For many of these applications, a high-Q is highly desirable since it increases the sensitivity. For the remainder of this thesis, we will be concerned with the properties of room-temperature CVD graphene NEMS, which differ considerably from their low-temperature counterparts.

One key advantage that graphene NEMS have over other materials is potentially efficient control methods. The resonance frequency of graphene NEMS can be readily controlled using electrostatic gating(62) or heating(63). Furthermore, recent studies in supported graphene have shown the charge-neutrality point can be tuned using photoinduced doping(64). This method could allow for controlling the resonance frequency, similar to an electrostatic gate voltage, but would be reversable. However, studies of this effect are lacking.

1.3.1 Quality Factor in Room-Temperature Graphene NEMS

As discussed earlier, the Q plays a critical role in determining the efficacy of a nanomechanical system, both for single device and array applications. Early results showed that graphene NEMS have quality factors(20) of $Q \sim 10^{8} - 10^{+}$. This is in contrast to similarly-sized SiN beams(65) that have $Q \sim 10^{=}$. Barton et. al.(66) showed that the Q in monolayer CVD graphene drumheads obeyed a size-dependence, with $Q \propto a$, with $Q \sim 2400$ for $a = 11.25$ μm (See Figure 1.5). Furthermore, they showed that the Q of higher-order modes slightly decreased, similar to silicon-nitride devices(44). However, they were unable to ascertain the origin of the damping mechanisms, or why the Q is so much lower than in other nanomechanical systems.

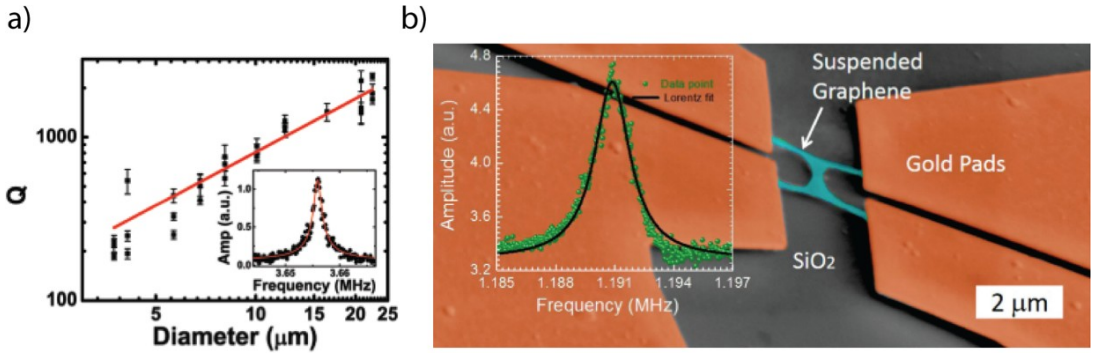

Figure 1.5: Quality factor in graphene NEMS. (a) Size-dependent quality factor in monolayer CVD graphene. Taken from(66) (b) SEM image and resonance curve of graphene 'H' beam with Q~$10^{"}$. Image taken from(67)

Since this early work, some efforts have been made to increase the Q in graphene NEMS. Oshidari et. al.(68) showed than by straining a few-layer, ~10 μm long graphene beam, the resonance frequency could be increased by a factor of 3 with the Q increasing from ~300 to ~7700, which they attributed to the additional tension. Kumar and Bhaskaran(67) demonstrated ~2 μm long graphene 'H' beams fabricated with electron-beam lithography and reactive ion etching that had Q~1500. The origin of the low Q in graphene NEMS is still not well understood, although there are hints it obeys the same general trends as SiN NEMS(65), and no significant effort has been devoted to improve it. The time is ripe for a unifying theory to guide effort to increase the Q in graphene NEMS

1.4 Outline of Thesis

As discussed above, graphene NEMS offer a suite of exciting properties but have been limited by low quality factors and relatively little study of control methods which might be useful for NEMS arrays. This thesis will present a compendium of studies beginning to overcome these challenges, laying the groundwork for applications of graphene NEMS arrays. In essence, we wish to answer the same fundamental challenges laid out by the inventors of the RGT; increase the Q and control of $f_{\$}$.

Chapter II is devoted to the general theoretical framework used in this thesis.

Chapter III will describe the general experimental methods used in this work. Both the fabrication process, optical measurement methods, and electronic actuation methods will be discussed.

Chapter IV is based on work co-authored with Benjamín Alemán(69). In this work, we demonstrate the use of focused ion beam milling to craft graphene NEMS with various non-standard geometries, including triangular cantilevers and crosses, and measure their properties. We find that the quality factor can be improved by a factor of 20. These devices also display greatly increased force-sensitivity due to the combination of increased Q and reduced mass. This approach opens up a unique, currently inaccessible regime in graphene nanomechanics, one characterized by low strain, low frequency, small mass, and high Q, and facilitates tailoring of non-linearity and damping in mechanical structures composed of graphene.

Chapter V is based on work co-authored with Andrew Blaikie, Brittany Carter, and Benjamín Alemán(70). Here, we show that Focused Ion Beam (FIB) milling is a high-yield means to engineer the shape of graphene NEMS, which in turn modifies their mode shape. We describe the specialized cutting methods necessary to achieve complex geometries such as beams, tapered beams, and trampolines. We measure the mode shapes using optical interferometry and show that they are consistent with membrane theory. This work is an enabling step for future work which relies on well-defined mode shapes, such as mass spectrometry.

Chapter VI is based on currently unpublished work co-authored with Andrew Blaikie, Brittany Carter, Jayson Paulose, and Benjamín Alemán. Here, we perform a large-scale study of the quality factor in suspended graphene drumheads. We find that the quality factor in these graphene drumheads agrees with the predictions of a corrugation corrected theory of dissipation dilution when size, stress, and mode number are varied. Furthermore, we use Ga^+ irradiation to increase the stress and reduce wrinkles in suspended graphene, improving the quality factor by over an order of magnitude. Moreover, this corrugation corrected theory of dissipation dilution

predicts if dominant bending losses could be suppressed, quality factors above one million at room temperature could be achieved.

Chapter VII is based on work co-authored with Benjamín Alemán(71). In this work, we combine scanning optical interferometry and spatially-resolved optical actuation to determine how spatially localized the opto-thermal drive force is in graphene NEMS. We use a force density model to infer that the drive force is spatially localized to about the size of the laser spot, allowing us to selectively excite and suppress degenerate modes. These results offer a powerful approach to image and actuate any arbitrary high-order mode of a 2D NEMS.

Chapter VIII is based on work co-authored with Andrew Blaikie, and Benjamín Alemán(72). In this work, we demonstrate an electro-optic tuning method for graphene NEMS that has a persistence time of several days and can repeatedly write and erase the state of a single device with a high degree of precision. We show the scalability of this technique by aligning the frequencies of several devices and discuss potential implications of this tuning method for both single devices and as a means to program graphene NEMS arrays.

Chapter IX contains the overall conclusions from this thesis and will discuss the future work this thesis enables.

CHAPTER II

THEORETICAL BACKGROUND

2.1 From a Continuous Body to a Harmonic Oscillator

To study the behavior of mechanical oscillators, it is useful to first reduce their motion to that of a damped harmonic oscillator, which gives us the tools to understand their quality factors, mode shapes, and resonance frequencies. The Euler-Bernoulli beam equation describes the dynamic motion of mechanical systems across vastly different length scales, ranging from bridges to nanoscopic mechanical resonators(14), however, it is not written in a form that resembles the damped harmonic oscillator. For the two-dimensional mechanical structures considered in this work, the driven, damped Euler-Bernoulli beam equation describes the out-of-plane displacement $u(x, y, t)$ and is written as,

$$\rho \frac{\partial^2 u(x, y, t)}{\partial t^2} + \kappa \nabla^4 u(x, y, t) + \Gamma \frac{\partial u}{\partial t} - T \nabla^2 u(x, y, t) = F_z(x, y, t) \quad (2.1)$$

where ρ is the 2D mass density, $\kappa = EI$ is the bending stiffness (E is the elastic modulus and I is the moment of inertia), T is the tension, $F_z(x, y, t) = f(x, y)\cos(\omega t)$ is a spatially-dependent driving force density, and Γ is the linear damping coefficient due to extrinsic sources of damping(36).

If we assume that the all the vibrational motion is occurring in a single eigenmode of a circular plate, i.e. $u(x, y, t) \rightarrow a_n(t)\phi_n(r, \theta)$, we can recover the equation for a driven damped harmonic oscillator by multiplying Eq. 2.1 by the mode-shape $\phi_n(r, \theta)$ and integrating by parts over the dimensions of the structure, with the boundary conditions for a fully-clamped circular plate, $\phi_n(r = a) = \nabla\phi_n(r = a) = 0$. This yields a set of effective parameters(14),

$$\ddot{a}_n(t) + \frac{\Gamma_{344}}{m_{344}} \dot{a}_n(t) + \left(\frac{k_{6,344}}{m_{344}} + \frac{k_{n,344}}{m_{344}}\right) a_n(t) = F_{344} \cos(\omega t) \quad (2.2)$$

$$m_{344} = \rho a^2 \int_0^{2\pi} d\theta \int_0^a s\, ds\, \phi_n^2(s, \theta) \quad (2.3)$$

$$\Gamma_{344} = \Gamma a^{+} \int_{0}^{+\infty} d\theta \int_{0}^{1} s\,ds\,\phi_{n}^{+}(s,\theta) \tag{2.4}$$

$$k_{6,344} = \frac{\kappa}{a^{+}} \int_{0}^{+\infty} d\theta \int_{0}^{1} s\,ds\,\nabla \phi_{n\cdots}(s,\theta)\,\nabla \phi_{n\cdots}(s,\theta) \tag{2.5}$$

$$k_{n,344} = -T \int_{0}^{+\infty} d\theta \int_{0}^{1} s\,ds\,\nabla^{+}\phi_{n\cdots}(s,\theta)\phi_{n\cdots}(s,\theta) \tag{2.6}$$

$$F_{344} = a^{+} \int_{0}^{+\infty} d\theta \int_{0}^{1} s\,ds f(r,\theta)\phi_{n\cdots}(s,\theta) \tag{2.7}$$

where $k_{6,344}$ and $k_{n,344}$ are taken to be the plate and membrane spring constants for the mode $\phi_{n\cdots}$. The mode number is dropped on the effective parameters for brevity. We can re-write this in the form of the driven-damped harmonic oscillator,

$$a_{n\cdots}(t) + 2\beta a_{n\cdots}(t) + \omega_{n\cdots}^{2} a_{n\cdots}(t) = \frac{F_{abc}}{m_{abc}} cos(\omega t) \tag{2.8}$$

where $\omega_{0}^{+} = \frac{k_{n,abc}}{m_{abc}} + \frac{k_{6,abc}}{m_{abc}} = \omega_{6}^{+} + \omega_{n}^{+}$ and $\beta = \frac{A_{abc}}{2m_{abc}}$. We can solve this for the amplitude in the quasi steady-state in the complex regime by letting $a(t) \rightarrow Re\{z(t)\}$ and assuming the solution $z_{n\cdots}(t) = z_{n\cdots}(\omega)exp(i\omega t)$,

$$-z_{n\cdots}(\omega)\omega^{2} + z_{n\cdots}(\omega)2\beta i\omega + z_{n\cdots}(\omega)\omega_{n}^{2} = F_{abc} \tag{2.9}$$

$$z_{n\cdots}(\omega) = \frac{F_{abc}}{(\omega_{0}^{2} - \omega^{2}) + 2i\beta\omega} \tag{2.10}$$

Taking the amplitude and complex phase, we arrive at the standard equations for the driven-damped harmonic oscillator,

$$\mathrm{abs}(z_{n\cdots}) = R(\omega) = \frac{F_{344}/m_{344}}{\sqrt{(\omega_{0}^{2} - \omega^{2})^{2} + 4\beta^{2}\omega^{2}}} \tag{2.11}$$

$$\arg(z_{BC}) = \Theta(\omega) = \tan^{-1}\left(\frac{2\beta\omega}{\omega^{2} - \omega_{0}^{2}}\right) \tag{2.12}$$

The true resonance frequency (i.e. the frequency where $R(\omega)$ is maximized) of the system is given by $\omega_{D} = \omega_{0}\sqrt{1 - \frac{1}{2}\left(\frac{1}{Q}\right)^{2}}$, where $Q = \frac{\omega_{n}}{2\beta}$. For the devices studied in this work, $\frac{1}{2}\left(\frac{1}{Q}\right)^{2} < 10^{-3}$ so $\omega_{D} \approx \omega_{0}$. As such, the resonance frequency will refer to ω_{0} or $f_{0} = \omega_{0}/2\pi$ rather than ω_{D} for the remainder of this thesis.

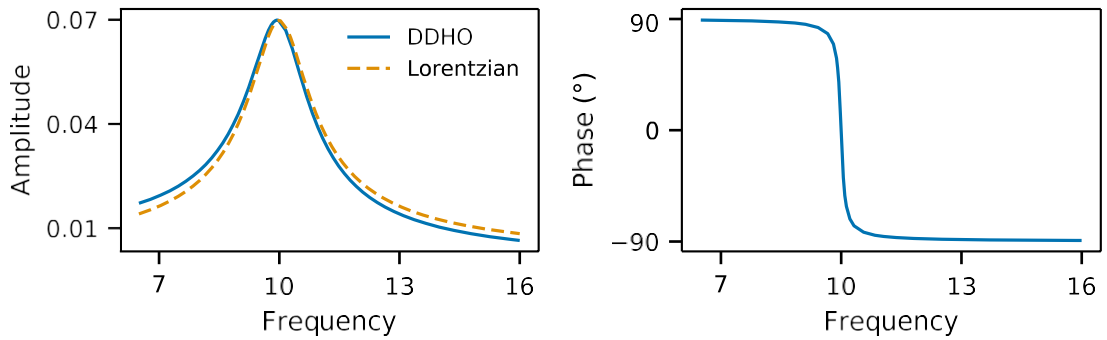

Figure 2.1: Amplitude (left) and phase (right) for the amplitude response of a driven damped harmonic oscillator with a $Q = 7$. For comparison, the amplitude of a Lorentzian lineshape is shown in the dashed orange line

We now prove that Q as defined above is the mechanical quality factor, which is defined by the ratio of energy stored over an oscillation cycle at resonance to the dissipated energy, $Q = 2\pi\frac{\text{Energy}}{\text{Energy lost per cycle}}$. We can solve for this by looking at Eq. 2.8 in the undriven case with an initial displacement (i.e. $F_{\text{drive}} = 0$). We solve this in the complex domain with trial solution of $z_{\text{trial}} = z_0 exp(ibt)$,

$$-b^2 + \frac{ib\omega_0}{Q} + \omega_0^2 = 0 \tag{2.13}$$

$$b = \frac{\frac{i\omega_0}{Q} \pm \sqrt{-\left(\frac{\omega_0}{Q}\right)^2 + 4\omega_0^2}}{2} \tag{2.14}$$

In the limit of high-Q, which is the case for the devices studied in this thesis, $4\omega_0^2 \gg \left(\frac{\omega_0}{Q}\right)^2$, so $b = \frac{i\omega_0}{2Q} \pm \omega_0$. The term under the square root is real as long as $Q > \frac{1}{2}$ allowing us to write $z_{\text{free}} = z_0 \exp\left(-\frac{\omega_0}{2Q}t\right)\cos(\omega_0 t)$. The energy of the resonator on resonance is thus $W = \frac{1}{2}m_{\text{eff}}\omega_0^2 z_0^2$. Meanwhile the energy lost over a cycle is

$$\Delta W = \frac{1}{2}m_{\text{eff}}\left(\frac{\omega_0}{Q}\right)z_0^2 \quad \frac{1}{2}m_{\text{eff}}\omega_0^2 \quad \exp\left(-\frac{\pi}{Q}\right)z_0^2 \approx m_{\text{eff}}\omega_0^2 z_0^2\frac{\pi}{Q} \tag{2.15}$$

thus, $2\pi\frac{\text{Energy}}{\text{Energy lost per cycle}} \approx Q$.

We finally will note that in the high Q limit near the resonance ω_0, $\omega \approx \omega_0$ and Eq. 2.11 can be approximated by a Lorentzian lineshape (shown in Figure 2.1),

$$z_{mn}(\omega) = \frac{F_{344}/2\omega_0}{\sqrt{(\omega_0 - \omega)^2 + \left(\frac{\omega_0}{2Q}\right)^2}} \tag{2.16}$$

2.2 Mode Shapes

For many applications including mass sensing(32) and for understanding(39) the Q, the precise shape of the mechanical modes is important. The set of eigenfunctions $\phi_{mn}(r,\theta)$ defining the mechanical mode shape and resonance frequencies ω_{mn} can be found by solving the homogenous part of Eq. 2.1. with the boundary conditions defined above,

$$\frac{1}{a_{mn}(t)}\rho\frac{\partial^2 a_{mn}(t)}{\partial t^2} + \frac{1}{\phi_{mn}(r,\theta)}\kappa\nabla^2\phi_{mn}(r,\theta) + \frac{1}{a_{mn}(t)}\Gamma\frac{\partial a_{mn}}{\partial t} - \frac{1}{\phi_{mn}(r,\theta)}T\nabla^2\phi_{mn}(r,\theta) = 0 \tag{2.17}$$

Separating variables and looking at the spatial and time equations,

$$\nabla^2\phi_{mn}(s,\theta) - \frac{Ta^2}{\kappa}\nabla^2\phi_{mn}(s,\theta) + \frac{\rho}{\kappa}\omega_{mn}^2 a^2\phi(s,\theta) = 0 \tag{2.18}$$

where $s = \frac{D}{I}$ We first look in the limit $Ta^2 \gg \kappa$, which is applicable for most of this work. In this limit, Eq. 2.18 can be approximated as a membrane rather than a plate, with mode functions given by,

$$\phi_{mn}(s,\theta) \propto J_m[\alpha_{mn}s]\cos(m\theta) \tag{2.19}$$

where $m \geq 0$, $n \geq 1$, and α_{mn} is the n^{th} solution to the equation $J_m(s) = 0$. The first few values of α_{mn} are $\alpha_{01} = 2.405$, $\alpha_{11} = 3.832$, $\alpha_{21} = 5.136$, etc... The resonance frequencies of the circular membrane can be found by inserting Eq. 2.19. into Eq. 2.18. Doing this, we find a set of resonance frequencies for the mechanical modes,

$$\omega_{mn} = \frac{\alpha_{mn}}{a}\sqrt{\frac{\overline{T}}{\rho}} \tag{2.20}$$

The first several mode shapes for a circular membrane are shown in Figure 2.2.

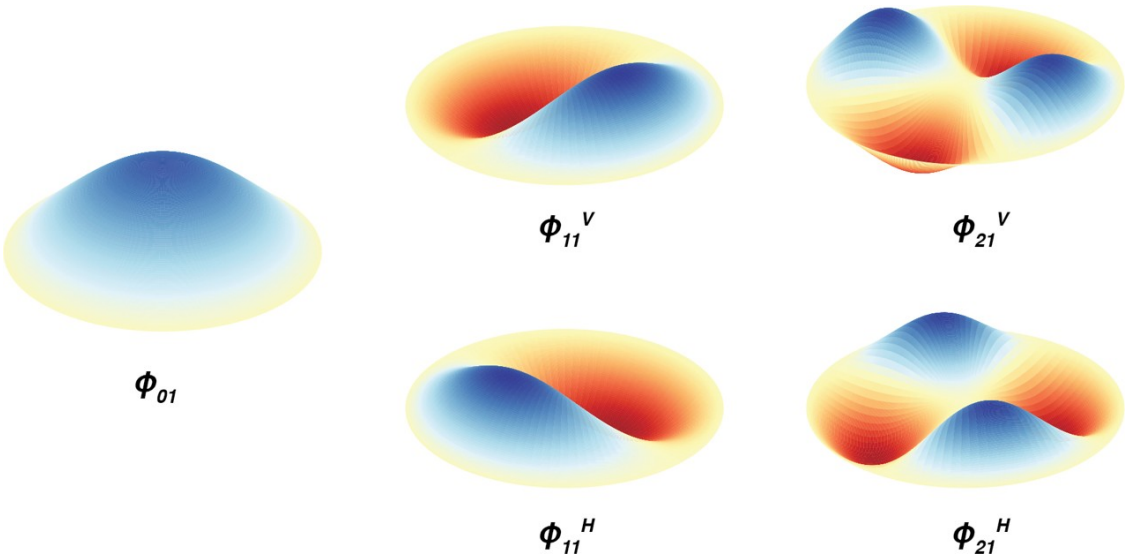

Figure 2.2: First 5 mechanical modes of a circular membrane. The horizontally and vertically polarized degenerate modes are indicated with either an 'H' or a 'V'.

Although the membrane solution is appropriate for most of this work, the study presented in Chapter VI requires a more detailed analysis of the exact solution of the mode shape. The full solution to Eq. 2.18 can be found as follows(73). Factoring the operator in Eq. 2.18 gives,

$$(\nabla^{+} + \eta^{+}_{\blacksquare\blacksquare})(\nabla^{+} - \xi^{+}_{\blacksquare\blacksquare})\phi_{\blacksquare\blacksquare} = 0 \tag{2.21}$$

where,

$$\eta^{+}_{\blacksquare} = \frac{Ta^{+}}{2\kappa}\left(1 + \sqrt{1 + \frac{4\omega^{+}_{\blacksquare}\rho\kappa}{Ta^{+}}}\right) \tag{2.22}$$

$$\xi^{+}_{\blacksquare} = \frac{Ta^{+}}{2\kappa}\left(1 + \sqrt{1 + \frac{4\omega^{+}_{\blacksquare}\rho\kappa}{Ta^{+}}}\right) \tag{2.23}$$

and

$$\xi^{+}_{\blacksquare\blacksquare} - \eta^{+}_{\blacksquare\blacksquare} = \frac{Ta^{+}}{\kappa} \equiv \frac{1}{\lambda^{+}} \tag{2.24}$$

The parameter λ is proportional to the ratio of energy stored in tension to that stored in bending and is a measure of whether a thin plate will behave more like a plate (e.g. out-of-plane internal stresses) or a membrane (e.g. in-plane internal stresses only). The solution to Eq. 2.21 is the sum of the solution to the following differential equations,

$$(\nabla^+ + \eta^+_{!\cdot\cdot})\phi_{\mathbf{I}} = 0 \tag{2.25}$$

$$(\nabla^+ - \xi^+_{!\cdot\cdot})\phi_{3} = 0 \tag{2.26}$$

where ϕ_{I} describes the mode shape of the mode shape around the antinodes and ϕ_3 describes that near the edge. Solving these equations with the boundary conditions $\phi_{!\cdot\cdot}(r=a) = \nabla\phi_{!\cdot\cdot}(r=a) = 0$, we find

$$\phi_{\mathrm{I}} = C \times J_{!}[\eta_{!\cdot\cdot} s]\cos(m\theta) \tag{2.27}$$

$$\phi_{3} = -C \times \frac{J_{!}[\eta_{!\cdot\cdot}]}{I_{!}[\xi_{!\cdot\cdot}]} I_{!}[\xi_{!\cdot\cdot} s]\cos(m\theta) \tag{2.28}$$

with the overall solution given by,

$$\phi_{!\cdot\cdot}(s,\theta) = C \times \mathrm{o}J_{!}[\eta_{!\cdot\cdot} s] - \frac{J_{!}[\eta_{!\cdot\cdot}]}{I_{!}[\xi_{!\cdot\cdot}]} I_{!}[\xi_{!\cdot\cdot} s]\mathrm{p}\cos(m\theta) \tag{2.29}$$

and the constants $\eta_{!\cdot\cdot}$ and $\xi_{!\cdot\cdot}$ determined from the n^{th} solution to the equation,

$$\eta_{!\cdot\cdot}\frac{J_{!}\mathrm{J}8[\eta_{!\cdot\cdot}]}{J_{!}[\eta_{!\cdot\cdot}]} + \blacksquare_{!\cdot\cdot}\frac{I_{!}\mathrm{J}8[\xi_{!\cdot\cdot}]}{I_{!}[\xi_{!\cdot\cdot}]} = 0 \tag{2.30}$$

We numerically evaluate Eq. 2.24 and Eq. 2.30 to find $\eta_{!\cdot\cdot}(\lambda)$ and $\xi_{!\cdot\cdot}(\lambda)$ (Figure 2.3). As $\lambda \to 0, \eta_{!\cdot\cdot} \to \alpha_{!\cdot\cdot}$ and $\xi_{!\cdot\cdot} \to 1/\lambda$ and the membrane approximation is recovered.

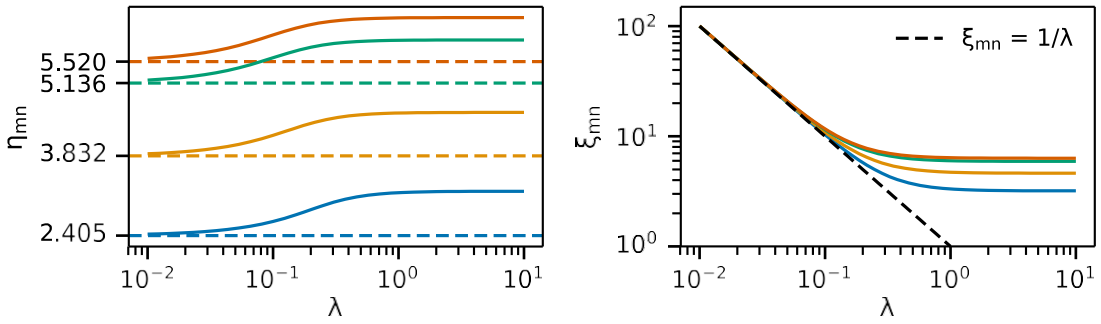

Figure 2.3: Numerically tabulated values of η_{*+} (left) and ξ_{*+} (right) for the first several mechanical modes. For small values of λ, $\eta_{*+} \to \alpha_{*+}$ and $\xi_{*+} \to \lambda$.

We compare the membrane approximation and the exact plate solution for $\phi_{\$8}$ in Figure 2.4. Both solutions are similar near the central antinode. At the boundaries, the plate solutions bend within a length scale determined by λ (insets) to satisfy the boundary condition $\nabla\phi(r = a) = 0$. As λ becomes smaller, the plate solution approaches the membrane solution but with an extremely large curvature near the clamped edge. This high curvature can lead to additional loss in NEMS(38).

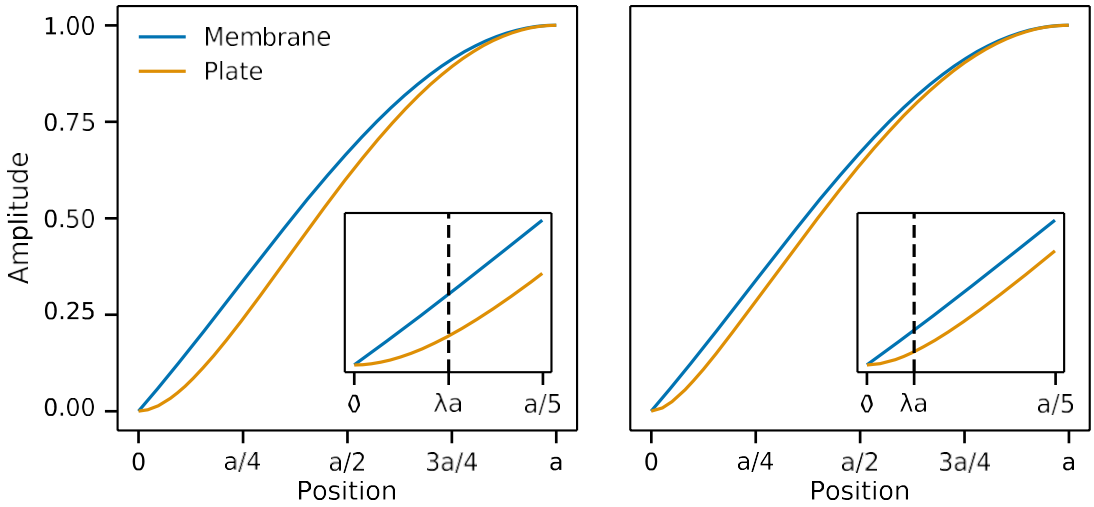

Figure 2.4: Mode shapes for circular plates and membranes. $\phi_{,-}$ for a value of $\lambda = .1$ (left) and $\lambda = .05$ with the insets showing the behavior near the clamped edge. The mode shape for a membrane (Eq. 2.19) and plate (Eq. 2.29) are shown.

2.3 Dissipation Dilution

Perhaps the most exciting development in the field of nanomechanics in recent years has been the emergence of dissipation dilution theory (DDT) as a guiding principle to both explain and engineer the quality factor in NEMS(34, 35, 38–41). Although DDT has been used to understand the Q in a wide range of NEMS materials, it has not yet been applied to graphene. In the Zener theory of dissipation in an anelastic material(36), damping is not linear but occurs due to a phase-lag between stress and strain. In this model, the elastic modulus is replaced by a complex valued function, $E \rightarrow E(1 + i\delta)$. Here, δ is a relatively frequency-independent constant that arises from internal loss. Putting this into Eq. 2.1, we arrive at the following equation of motion,

$$a_{!''}(t) + \omega_6^{+}(1 + i\delta)a_{!''}(t) + \omega_!^{+}a_{!''}(t) = \frac{F_{344}}{m_{344}}cos(\omega t) \tag{2.31}$$

Solving this similarly to the linearly-damped case, we obtain a solution slightly different than the damped harmonic oscillator,

$$z_{!''}(\omega) = \frac{F_{344}}{(\omega_\$^{+} - \omega^{+}) + \delta\frac{i\omega_6^{+}}{\omega_\$^{+}}\omega_\$^{+}} \tag{2.32}$$

with ω_6 and $\omega_\$$ the same as defined earlier. However, if make the approximation $\omega \approx \omega_\$$, we obtain a Lorentzian response,

$$A_{!''}(\omega) = \frac{K_{\%\&\&}/+*_!}{L(*_! - *) - J\,0P - \frac{\#}{-/_!}*_!Q} \tag{2.33}$$

and can now make the correspondence between the quality factor of the intrinsically damped oscillator and the linearly-damped harmonic oscillator,

$$Q = \frac{1}{\delta}\frac{\omega^{+} + \omega_!^{+}}{\omega_6^{+}} = Q_{1"R}\frac{\omega^{+} + \omega_!^{+}}{\omega_6^{+}} = Q_{1"R}\,o1 \quad \frac{k_!}{k_6}p = D_\# Q_{1"R} \tag{2.34}$$

where $Q_{1"R} = \frac{8}{p}$ is the intrinsic material quality factor and $D_\#$ is called the dilution factor. A similar result may be obtained from energetics(40), directly solving for $Q = 2\pi\frac{C}{FC}$. An approximate analytic form of Eq. 2.34 can be evaluated using Eq. 2.5 and Eq. 2.6 in the membrane limit of $\lambda \ll 1$ (See Section B.1 for the full derivation),

$$Q \approx Q_{1"R}\frac{1 + \lambda^{+}\alpha_{!''}^{+}}{\lambda(1 + \alpha_!^{+}\lambda)}p \tag{2.35}$$

This expression is similar to those found for square membranes(44) and strings(38). We plot $D_\#$ for the first 3 modes of a circular membrane vs. λ in Figure 2.5 for both exact solution (Eq. 2.34), which we find with numeric integration, and the analytic approximation in Eq. 2.35.

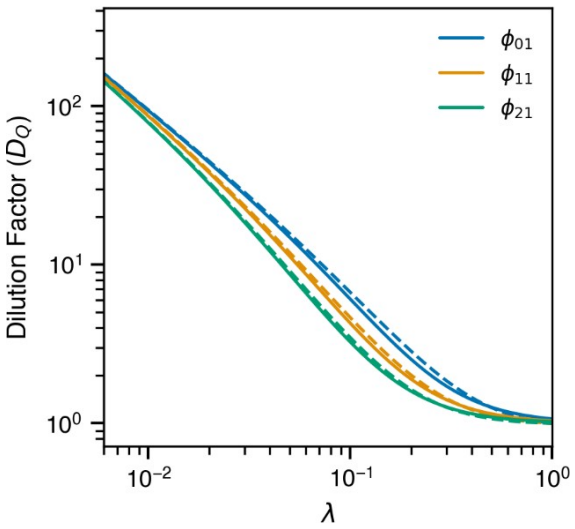

Figure 2.5: Exact (solid lines) and approximate (dashed lines) D_0 for the first 3 modes of a circular plate.

In DDT, the Q can be maximized by increasing λ, which can be accomplished either by increasing increasing Ta^+, which is proportional to the elongational energy, or reducing κ, which is proportional to the bending energy. This means the highest quality factors are achieved in thin, high-strain, large-area NEMS. We will further discuss the implications of dissipation dilution when applied to graphene NEMS in Chapter VI.

CHAPTER III

EXPERIMENTAL METHODS

3.1 Graphene Transfer and Semiconductor Device Processing

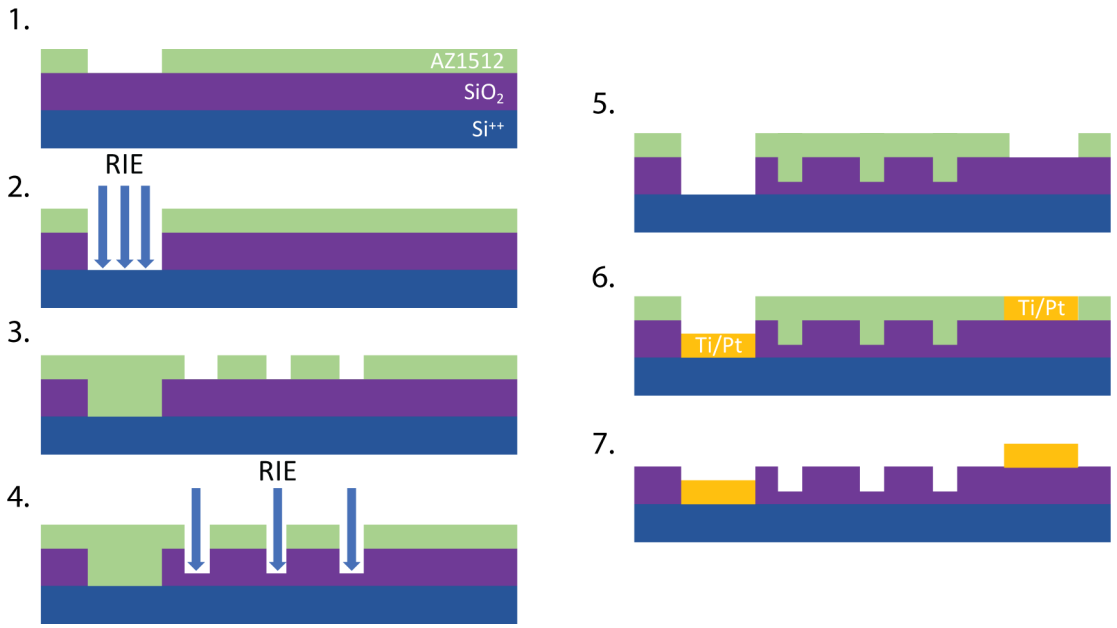

Figure 3.1: Process flow for fabrication of substrates. We start with a commercially acquired degenerately doped silicon wafer with 1 μm of wet thermal oxide. 1. Spin on AZ1512 and expose a large region for a via with photolithography. 2. Use a CHF_3 based reactive ion etch to etch the SiO_2 all the way to the Si. 3. Perform a second step of photolithography to expose arrays of circular holes. 4: Use a CHF_3 based reactive ion etch to partially etch the SiO_2, leaving a ~300 nm thick layer at the bottom of the holes to prevent shorting. 5. Perform a final step of photolithography to expose the via and a grid for electrical contacts. 6: Evaporate a 5 nm of Ti for adhesion followed by ~50 nm of Pt. 7: Lift-off final photoresist layer overnight in acetone.

We fabricate graphene NEMS using conventional planar device processing techniques shown in Figure 3.1, followed by semi-dry transfer process(74), shown in Figure 3.2. The general process is as follows. First, degenerately-doped silicon wafers with a thermally grown oxide (typically 1 μm) are dehydrated at 400 °C for 30 minutes. The

wafer is then placed under a large recrystallization dish with an opened bottle of hexamethyldisilazane (HMDS) for 2 hours. The HMDS forms a self-assembled monolayer that promotes adhesion of photoresist. We then spin on a film of AZ1512 photoresist at 4000 RPM, yielding a resist thickness of ~1.5 μm. We then perform direct-write photolithography to expose large (~5 mm^2) openings in the photoresist using a 405 nm laser and a dose typically between $250 - 400$ $\mu J/cm^2$. The exposed patterns are developed by immersion in AZ300 MIF developer for 2 minutes followed by immersion in deionized water followed by ~30 s of direct spraying with DI water. We then use a CHF_3/Ar reactive ion etch, which etches SiO_2 at a rate of ~35 nm/min, to etch the exposed SiO_2 all the way to the silicon substrate, forming a via. The AZ1512 is then removed by sonication in acetone. We then repeat this entire process to pattern an array of circular holes in the SiO_2 with diameter between 4 μm and 25 μm. A thin (~few 100 nm) layer of SiO_2 is left at the bottom of the holes to prevent shorting from collapsed graphene. A ~1 μm wide trench connects neighboring holes to allow gas to escape when the graphene drums are brought under vacuum(75).

Next, we perform a third step of photolithography to expose a grid surrounding the circular holes as well as the large vias. Then, we deposit a 5 nm/50 nm layer of Ti/Pt using electron-beam evaporation. We use platinum since we find gold balls up during later high-temperature processing. The resist is removed by soaking in acetone overnight followed by sonication.

Graphene is commercially acquired from various suppliers, typically Graphenea, on 60 mm × 40 mm pieces of thin copper foil. The copper foil is divided in ~10 mm × 10 mm pieces using a scalpel and stored for later. A rocking, rather than slicing, motion on a thick piece of plastic is used to cut the foil in order to prevent crumpling.

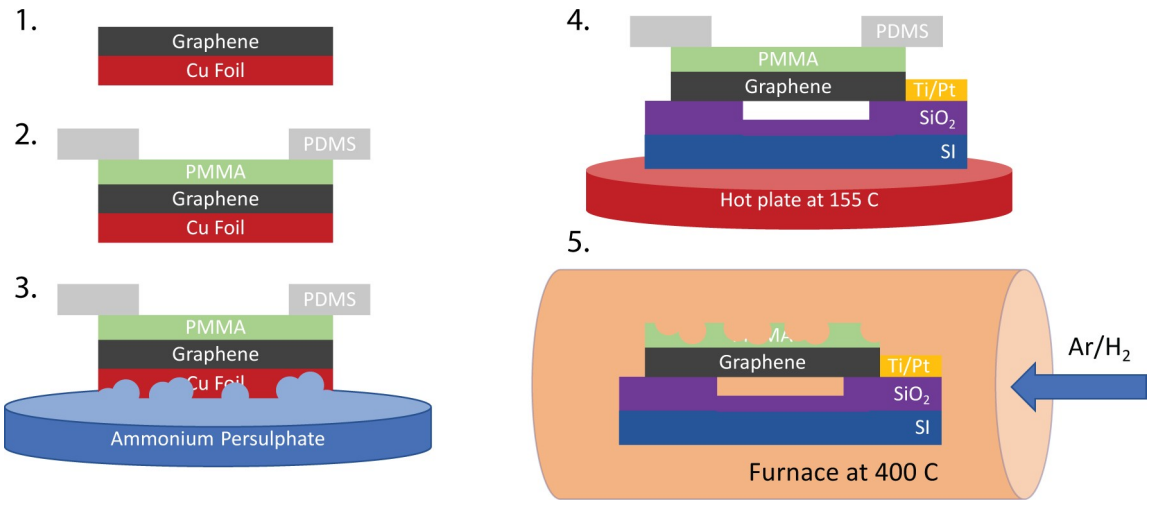

Figure 3.2: Process flow for transfer of graphene onto target substrate. 1. Graphene on copper foil is acquired from commercial vendors. 2. A relatively thick layer of PMMA (~3 µm) is spun onto the graphene foil. A PDMS stamp is then placed on the PMMA/Graphene/Cu stack. 3. Cu is etched by floating PDMS/PMMA/Graphene/Cu foil on ammonium persulphate for several hours. 4. PDMS/PMMA/Graphene stack placed on target substrate and baked at 155 °C for >12 hours. 5. PDMS is peeled of cut off the PMMA and the PMMA/Graphene/Chip is placed in a furnace at 400 °C in flowing Ar/H_2 for ~3 hours.

To transfer graphene, a piece of foil is placed on a smaller piece of PDMS/Plastic backing. The Graphene/Cu/PDMS/Plastic stack is placed on a spin coater, with the plastic side on the vacuum chuck. We then spin on PMMA A11 at 3000 RPM, yield a ~3 µm thick layer, which we let air dry for 15 minutes. The plastic holds vacuum on the spin-coater while the PDMS provides enough static friction to prevent the foil from flying off. This is in contrast to placing the foil directly on the vacuum chuck, which leaves a dimple in the copper foil. We then remove the PDMS and use 2 minutes of O_2 plasma cleaning to remove the exposed graphene on the backside of the PMMA/Graphene stack. We then place a hole-punched piece of Plastic/PDMS on top of the PMMA/Graphene/Cu to act as a scaffold. We sometimes use thermal release tape or polyamide tape instead of the Plastic/PDMS, with similar results. The Plastic/PDMS/PMMA/Graphene/Cu floated on ammonium persulphate (40 mg/ml) to etch the Cu, which takes several hours. The Plastic/PDMS/PMMA/Graphene is then sequentially floated in 3 DI water baths before being dried in air.

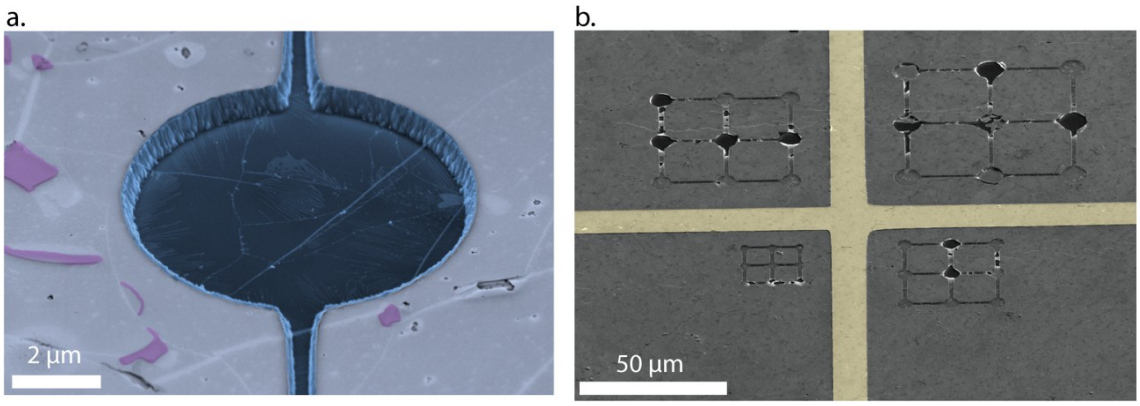

Figure 3.3: SEM images of finished graphene devices. (a) False-colored SEM of a graphene drumhead. The dark blue region highlights the suspended graphene devices. Grain boundaries and contamination are visible on the surface. (b) False-colored SEM of arrays of graphene drumheads. Electrodes are colored in yellow. Several failed devices are visible in the image.

Meanwhile, the target chip is cleaned in O_2 plasma cleaned and then baked on a hot-plate at 400 °C for several hours. These steps promote graphene adhesion to the SiO_2 surface. Then, the chip is brought to 155 °C and the fully suspended PMMA/Graphene is placed on top of it. The PMMA/Graphene/Chip is left to adhere overnight (>12 hours). We use tweezers or a scalpel to isolate the chip from the Plastic/PMMA support and remove it. We find some evidence that lower humidity values lead to higher yield of suspended graphene, however, we do not have definite confirmation of this. We also found that the particular batch of PMMA A11 has a significant impact on the yield of devices but we were unable to understand the exact mechanism behind this. The PMMA is removed at 400 °C under flowing H_2/Ar (100/400 SCCM). The final step is manual removal (using tweezers or a micromanipulator) to remove the graphene between the via and the top electrode. This process yields arrays of electrically connected graphene membranes, each of which forms a single NEMS. A finished device is shown in Figure 3.3a while an array of devices with a Ti/Pt electrode is shown in Figure 3.3b.

3.2 Focused Ion Beam Lithography of Graphene NEMS

In Chapter IV and Chapter V, we use FIB milling to fabricate suspended graphene NEMS with non-circular geometries. A more detailed description of the FIB-cutting approach will be presented in those chapters. In general, we use a FEI Helios 600i dual-beam FIB-SEM, which consists of a standard vertical electron column and a Ga^+ ion column mounted at 52° from vertical. In this way, imaging electrons and milling ions can be co-localized on a sample. Prior to milling, we focus the image obtained via scanning FIB microscopy and confirm the focus using a series of linear test cuts. The ultimate resolution of Ga^+ milling depends on the beam current. To achieve the highest resolution milling, we use beam currents of 1.1 pA, which is the lowest available on the FEI Helios 600i. With this dose, we find that a line cut with a well-focused beam takes about 1 ms to mill through a layer of graphene. All patterning is done using the built-in FEI patterning software using circular and square geometries as well as exclusion zones. More complex geometries could made by directly controlling the beam location, although we did not explore this.

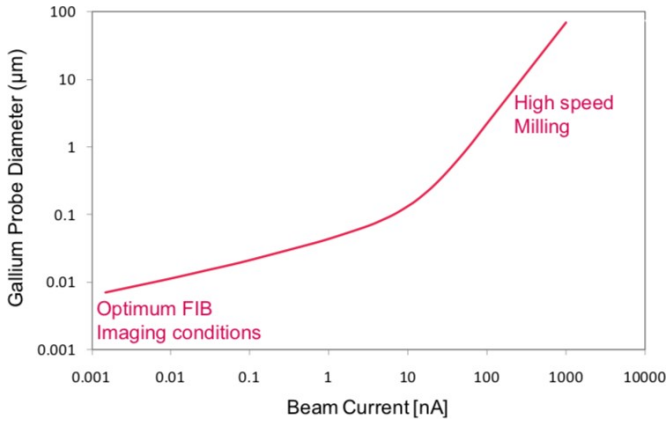

Figure 3.4 Ga^+ FIB resolution vs. dose. Taken from(76).

3.3 Actuation of GrapheneNEMS

Graphene NEMS have previously been actuated using a variety of techniques, including optically(77, 78), electrostatically(20, 54, 57, 79–82), electrothermally(63, 83), or with piezoelectric shakers(67). In this work, we use a combination of electrostatic and optical actuation, described in the two following sections

3.3.1 Optical Actuation of Graphene NEMS

Optical actuation is a valuable technique for driving graphene NEMS and is desirable when there is no back-gate, for example graphene membranes fabricated on transmission electron microcopy (TEM) grids(66, 84), or when precise control of the actuation efficiency of various mechanical modes(85) is required. In the optical drive scheme, a laser amplitude modulated sinusoidally at the drive frequency, $f_>$, is focused onto the graphene membrane, with power,

$$P = \frac{P_\$}{2}(1 + \cos(2\pi f_> t)) \quad (3.1)$$

The laser periodically heats the membrane creating a photothermal drive force. The exact details of this interaction are still not entirely understood but it is an active area of study(47). We explore the optical drive process further in Chapter VII.

3.3.2 Electrostatic Actuation of Graphene NEMS

Graphene NEMS can be electrostatically actuated by applying an AC ($V_{/\&} = \delta V \cos(2\pi f_> t)$) and DC ($V_{344} = V_S - V_{!\&TU}$) voltage between the graphene drumheads and a back-gate. V_S is the supplied gate voltage and $V_{!\&TU}$ is the mechanical charge neutrality point(81, 86), which is often non-zero due to trapped charge in the graphene or the SiO_2. Exploitation of this trapped charge to tune the resonance frequency is the basis for Chapter VIII.

To see the effect of an electrostatic gate on a suspended graphene sheet, we start with the electrostatic potential energy of a parallel-plate capacitor, where the distance between the plates can vary,

$$U = \frac{1}{2} C(z) \left(V_{/\&} + V_{344} \right)^2 \quad (3.2)$$

Here,

$$C(z) = \frac{\epsilon_\$ A}{d_{344} - z} \quad (3.3)$$

where d_{344} is the effective non-displaced capacitor thickness and is given by $d_{344} = d_V + \frac{\geq_1}{W_2}$, where ϵ_D is the permittivity of SiO_2, d_V is the distance between the graphene

and the SiO_2, and d_X is the oxide thickness. The electrostatic force felt by the membrane is thus,

$$F = -\frac{dU}{dx} \approx -C\,z\,V_{344}V_{/\&} - \frac{1}{2}C\,z\,yV_{344}z \quad (3.4)$$

where we've thrown away the $-C^{Y}(z)(V_{/\&})^{+}$ term in since it will result in a force at twice the drive frequency, which will not be detected by a lock-in amplifier. The $-C^{Y}(z)V_{344}V_{/\&}$ term in Equation 3.4 results in an electrostatic drive force at $f_{>}$ with an amplification factor from V_{344}. The second $-\frac{8}{+}C^{Y}(z)yV_{344}z^{+}$ term results in a static force that can be used to tune the frequency (see section 3.6).

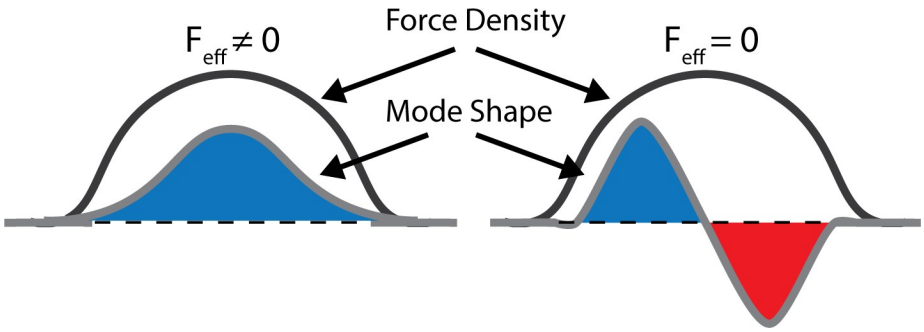

Figure 3.5: Diagram of the electrostatic drive force for a symmetric mode (left) and an antisymmetric mode (right).

One important consideration is that the electrostatic drive technique applies a symmetric force density across the membrane. From Eq. 2.7, we can see than a symmetric force integrated with an anti-symmetric (for example, the mode shape shown in right of Figure 3.5) will lead to no drive force. In theory, this means that the electrostatic drive technique cannot be used to excite higher order modes. In practice, small imperfections in the geometry or the mode shape of the membranes will break the perfect asymmetry, allowing a weak drive force even with anti-symmetric modes.

3.4 Two-Beam Optical Interferometry

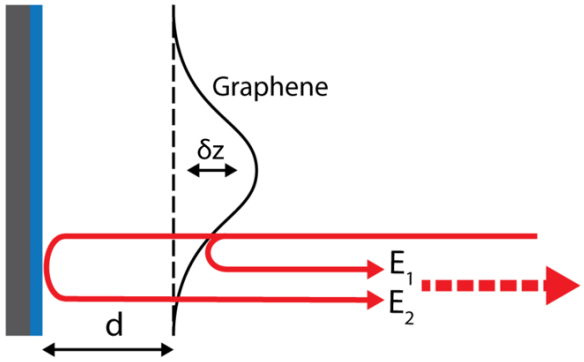

Figure 3.6: Diagram of two beam optical interferometry. The reference mirror can either be on a separate arm of the interferometer or the back-plane in a Fabry-Perot cavity.

We use two-beam interferometry in either a Michelson (shown in Supplementary Figure A.5) or Fabry-Perot (described in Section 3.7) configuration to transduce mechanical motion (87). Both transduction methods are mathematically equivalent to two-beam interference. However, the Michelson setup requires active stabilization of the reference mirror to reduce mechanical noise. We focus an incident optical field, E_1, with wavelength λ, onto the graphene drumheads, which reflect a small amount of light, $E_8 = E_{\$,8}$. The remaining light reflects off the silicon back-plane, with some attenuation, giving a reflected field $E_+ = E_{\$,+} e^{4\frac{1^{-3}}{—}\times+(>\mathbf{J}P5)}$, which has propagated an additional distance $2(d + \delta z)$. d is the equilibrium graphene-silicon distance and δz is the displacement of the graphene sheet from equilibrium. We ignore further reflections from the graphene sheet for the Fabry-Perot, which will be small. The displacement δz is given by,

$$\delta z = \delta z_{\$} \cos(2\pi f_{>} t + \Theta)\,. \tag{3.5}$$

where Θ is the phase of the response referenced to the actuation force. At the photodetector, the intensity is given by,

$$I \propto |E_8 + E_+|^+ = \not{E}_{\$,8}\,\mathrm{z}^+ + \not{E}_{\$,+}\,\mathrm{z}^+ + 2E_{\$,8}E_{\$,+}\cos(2d + 2(\delta z_{\$}\cos(2\pi f_{>} t + \Theta)) \tag{3.6}$$

Ignoring the DC terms, which will not be detected by a lock-in amplifier, the interference term measured is,

$$I \propto 2E_{\$,8}E_{\$,+}(\cos(2d)\cos(2(\delta z_{\$}\cos(2\pi f_{>} t + \Theta)) - \sin(2d)\sin(2(\delta z_{\$}\cos(2\pi f_{>} t + \Theta))) \tag{3.7}$$

Taking $\delta z_{\$}$ to be small (which we expect to be ~several nm) and combining constant terms, the interference term is,

$$I \propto -I_{\$}\delta z_{\$} \cos(2\pi f_{>} t + \Theta) \quad (3.8)$$

Thus, $\delta z_{\$}$ and Θ can be obtained above the DC background using lock-in amplification. For the purposes of this work, the vibrational amplitude is not-needed and we instead use the uncalibrated voltage obtained from the photodiode. Various methods have been developed to calibrate the motion of graphene nanodrums(61, 88) when an exact measurement of the vibrational amplitude is required.

3.5 Scanning Optical Interferometry

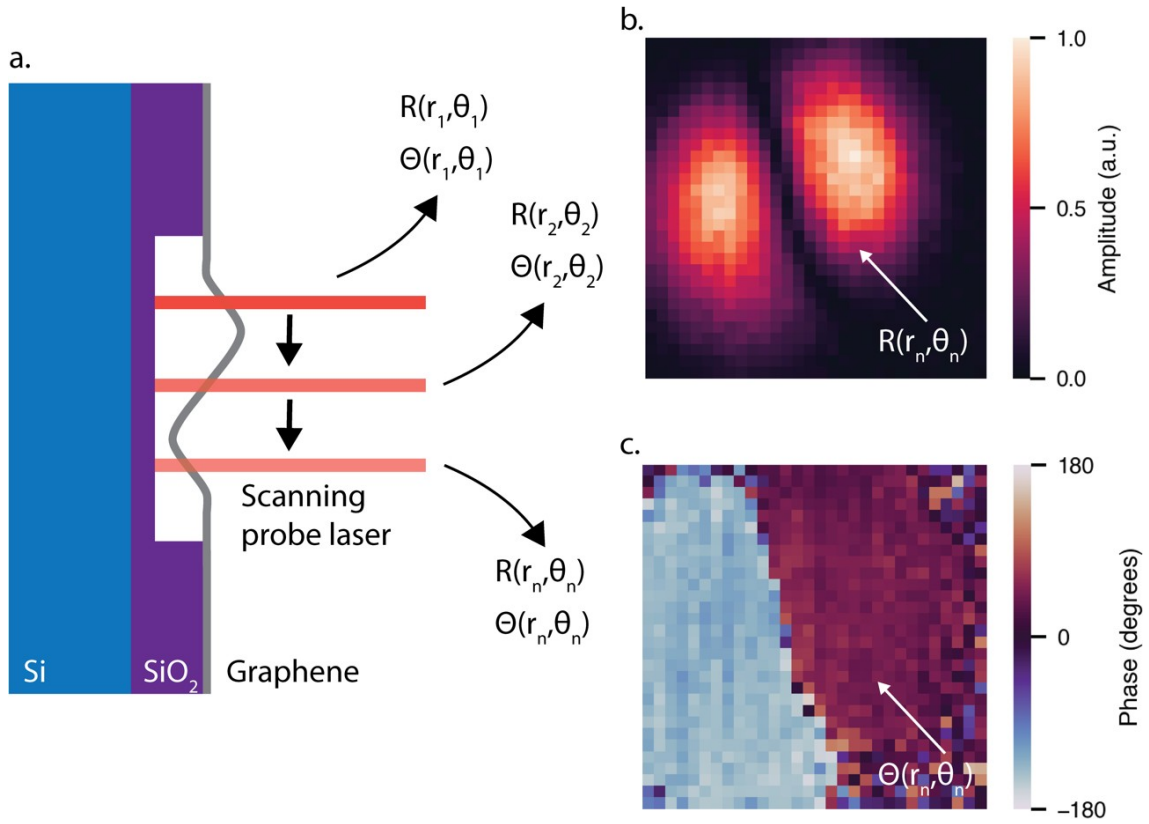

Figure 3.7: Scanning laser interferometry. (a) Diagram of scanning optical interferometry. (b) Amplitude measured at each point (r_{+}, θ_{+}) on a drumhead via scanning laser interferometry. (c) Phase measured at each point (r_{+}, θ_{+}) on a drumhead via scanning laser interferometry.

In many applications, such as mass spectrometry(32), an accurate determination of the mechanical mode shape is crucial. This can be accomplished either through direct AFM imaging(89) or with non-local scanning optical interferometry. In scanning

optical interferometry(79), the position of measurement laser, $\boldsymbol{r_p} = (r_p, \theta_p)$, is rastered across the drumhead and the amplitude and phase of the oscillation is recorded by the lock-in amplifier at each position (Figure 3.7a). Heatmaps (Figure 3.7b-c) can then be made of $R(r_p, \theta_p)$ and $\Theta(r_p, \theta_p)$ to visualize the mode shape and its phase. To increase the measurement speed, we perform scans at a fixed drive frequency rather than obtain a full frequency-response spectrum(79). The measured amplitude is different than the true mode shape due to the Gaussian beam spot and is given by the overlap of the mechanical mode and the laser spot,

$$A(\boldsymbol{r_p}) \propto < dA \exp\left(-\frac{|\boldsymbol{r} - \boldsymbol{r_p}|^2}{2\sigma_f^2}\right) \phi_{*+}(\boldsymbol{r}) \tag{3.9}$$

where σ_6 is related to the full-width at half-maximum as $\sigma_6 = FWHM/2.355$. For the 40x, .6 numerical aperture (NA) objective used in this work, the dilation due to the spread of the laser spot is negligible (see Chapter VII). In our work, we scan the laser with a galvometer and an optical relay system.

3.6 Electronic Frequency Tuning of Graphene NEMS

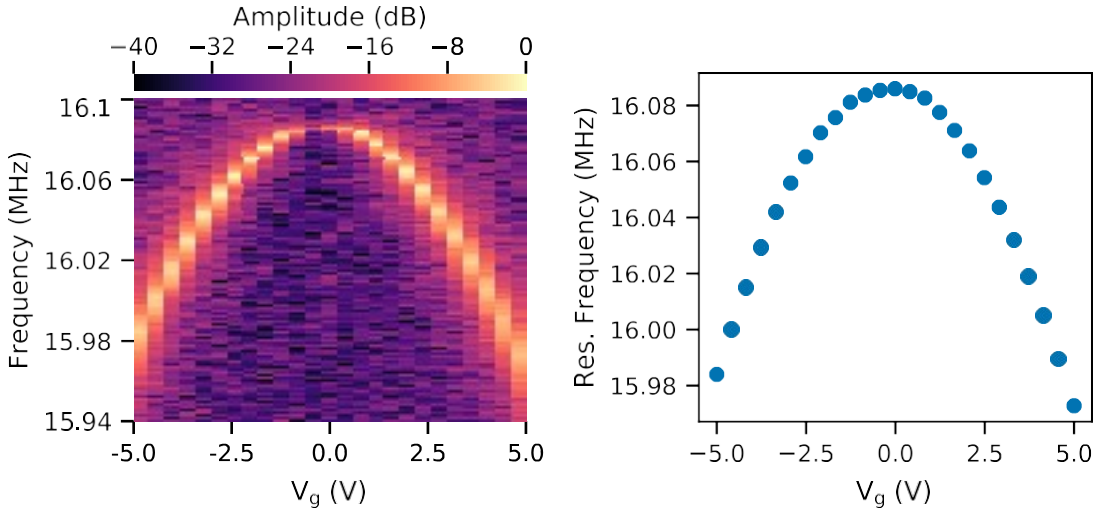

Figure 3.8: Spectrogram showing the amplitude-frequency response as a function of the gate voltage (left) along with the resonance frequency extracted from peak-fitting (right).

The ability to tune the resonance frequency of graphene NEMS using an electrostatic gate plays a crucial role in many chapters of this work and is highly desirable for many

applications. The second term in Equation 3.4, $-\frac{8}{+}C^{Y}(z)yV_{344}z^{+}$, allows for the tension in a graphene NEMS to be changed, thus tuning the resonance frequency. A common way to visualize this is with a spectrogram plot, where the gate-voltage is plotted on the x-axis, the drive frequency on the y-axis, and the vibrational amplitude encoded in the colormap. This is shown in Figure 3.8 for a graphene NEMS. By extracting the peak amplitude (either through curve-fitting or simply finding the max-amplitude), a plot of resonance frequency vs. V_S can be generated.

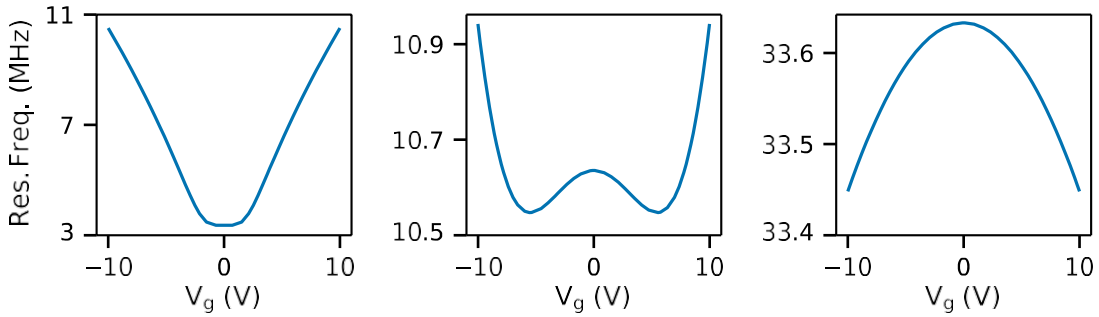

Figure 3.9: $f_{,}(V_{89})$ for initial tension values of 0.01 N/m, 0.1 N/m, and 1 N/m. The other parameters are typical for a graphene NEMS and are as follows: $R = 5$ μm, $d = 700$ nm, $Y = 100$ N/m, $\rho = 10 \times \rho_{:}$.

The behavior of $f_{\$}(V_{344})$ gives valuable information about the mechanical properties of a device. References(29, 62) developed a model for $f_{\$}(V_{344})$ and find,

$$(2\pi f_{\$})^{+} = \frac{2.4048^{+}T_{\$}}{a^{+}\rho} - \frac{\epsilon_{\$}(V_{\%\&})^{+}}{d\blacksquare} + 0.1316\frac{Y\epsilon^{+}(V_{\%\&})^{=}}{(1-\nu^{+})\rho T^{+}} \quad (3.10)$$

$$T = T_{\$} + \frac{Ya^{+}\epsilon_{\$}^{+}(V_{\%\&})^{=}}{(1-\nu^{+})128d^{=}T} \quad (3.11)$$

for the fundamental mode of a circular drumhead. A detailed derivation of this expression is presented in the supporting information of reference(62). The first term is the resonance frequency calculated from Eq. 2.1 in the absence of an additional voltage. The second term leading to a reduced frequency is due the reduction in the total energy of the system due to capacitive softening with the added gate voltage(90), and the third term is added tension due to the electrostatic pulling the membrane towards the back gate.

Eq. 3.10 results in a characteristic "inverted W" shape. For the gate-voltage values used in this work (< |15| V), Eq. 3.10 can yield several different shapes depending on the elastic and geometric parameters. Figure 3.9 show these for several values of $\sigma_{\$}$. Fitting this function with the known geometric parameters allows a measurement of the three unknown elastic properties ρ, Y, and T, which are typically very hard to measure (see Chapter VI).

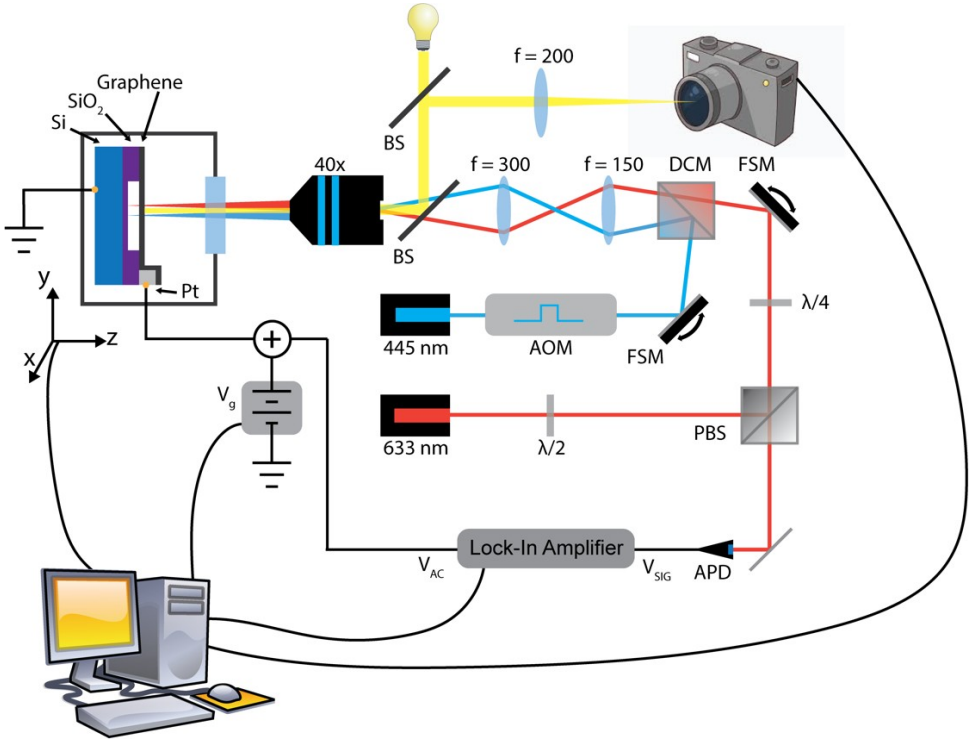

Figure 3.10: Diagram of the optical experiment used to actuate and transduce the motion of graphene NEMS. The devices are held in a vacuum chamber below 10^{-5} Torr, which can be moved 50 mm in XYZ under using motorized translation stages. BS: 50:50 beam splitter. PE: Pellicle beamsplitter. DCM: Dichoric mirror (550 nm longpass). FSM: Fast-steering mirror. $\lambda/2$: Half waveplate. $\lambda/4$: quarter waveplate. AOM: Acousto-optic modulator. PBS: polarizing beam splitter on motorized flipper. APD: Avalanche photodiode. All aspects of the experimental apparatus are controlled using custom-written LabView control software, allowing experiments to be performed remotely.

We note that the robustness of this fitting method is highly dependent on both the shape of the curve (mainly the depth of the local minima) as well as the how large a range of gate-voltages are measured (with a range often set arbitrarily(48, 62)). Previous work that used a similar fit found that the theory matched the data only a reasonably low gate voltages(48). One cause of this fitting discrepancy at high voltages is correlations in the fit parameters ($\langle Y, \rho \rangle$ and $\langle Y, T \rangle$) of the non-linear least-squares function become highly correlated when the concave section of $f(V_{\backslash])}$ becomes small compared to the concave up part of the curve. This high fit correlation value leads to diverging values of the fitted parameters and the three-parameter fit method is no longer appropriate.

3.7 Experimental Setup for Fabry-Perot Detection

For all the work described in this thesis, with the exception of Chapter IV, we use a Fabry-Perot detection scheme, shown in Figure 3.10

Our experimental setup is diagramed in Figure 3.10. We use a 633 nm frequency-stabilized HeNe laser (Thorlabs HRS015B). The beam is passed through a half-waveplate to rotate the polarization of the laser and then coupled into the detection beam-path with a polarizing beam splitter. The half-waveplate can be rotated to change the amount of laser light coupled into the detection path. Following the polarizing beam splitter, the laser is passed through a quarter-waveplate, which rotates the laser from linear to circularly polarized light. Next, the laser is reflected off a closed-loop 2-axis galvometer (Thorlabs GVS212) and is deflected by a small angle. The deflected beam is then passed through 550 nm longpass dichroic beam splitter followed by a scan lens ($f = 150$ mm) and tube lens ($f = 300$ mm). Both lenses are 2" diameter achromats to reduce aberrations as the beam is displaced from the center of the lenses. The beam then passes through a pellicle beam splitter, to reduce the beam shift when passing through a thin plate, on a motorized flip mount before being focused onto the sample by a 40×, 0.6 NA Plan-Fluor (for reduced chromatic aberration) objective lens with a glass-correction collar. On reflection from the sample, the beam passes back through the optical path and is rotated 90° from the

incident polarization by the quarter-waveplate. The reflected beam thus passes through the polarizing beam splitter before detection by a free-space avalanche photodiode.

A second optical path uses a 445 nm laser which is passed through an acousto-optic modulator (AOM) and deflected with a second galvometer before coupling into the main optical path with the 550 nm longpass. The blue laser is blocked by a 500 nm shortpass filter before reaching the photodiode. The modulation on the AOM is driven between $0 - 1$ V supplied from the lock-in amplifier.

A simple white-light microscope, coupled into the system by the pellicle beamsplitter, is used to image the sample and position the lasers at the correct location.

The samples are held under vacuum at $10^{-\hat{}}$ torr and placed in a vacuum chamber. The vacuum chamber can be moved in XYZ with motorized translation stages for the XY and motorized Labjack for Z. A custom window-mount allows us to use a 1 mm thick optical window with a visible-light anti-reflective (AR) coating, which is within the range of glass correction on the objective lens. The sample itself is mounted on a printed circuit board (PCB) which and is connected the signal and ground wires of a BNC feedthrough.

A spatial map of the mechanical mode shape can be obtained by scanning the position of the laser spot on the graphene drumhead (see Section 3.5). In contrast to previous work where the sample is scanned with a fixed laser, we use a closed-loop galvometer and optical relay system to scan the laser over the drumhead surface of the drumhead, allowing for much faster acquisition of spatial maps.

All parts of the experimental apparatus are computer controlled via USB through LabVIEW, allowing for fully remote measurements to take place.

CHAPTER IV

SHAPE TAILORING TO ENHANCE AND TUNE THE PROPERTIES OF GRAPHENE NANOMECHANICAL RESONATORS

From D. Miller, B. Alemán, Shape tailoring to enhance and tune the properties of graphene nanomechanical resonators. *2D Mater.* **4**, 025101 (2017). I performed the fabrication, experimental measurements, data analysis, and am the primary author on the publication. Benjamín Alemán is my supervisor.

4.1 Introduction

Nanomechanical resonators, such as freely vibrating nanometer-scale beams and membranes, have enabled ultrasensitive physical measurements at the level of single atom mass(17) and single electron charge(91) as well as the exploration of quantum mechanics in macroscopic mechanical systems(92). Among the most promising applications of nanomechanical systems is the ability to detect extremely small forces, such as those that arise from chemical or biological processes(93) or from electronic or nuclear spins(18), which is ultimately limited by thermal fluctuations due to mechanical damping. The minimum detectable force(94) for a mechanical resonator at a given temperature is directly related to the coefficient of mechanical damping as $\delta F_{min} \propto \sqrt{b}$, where the damping coefficient, b, is related to the resonator mass, mechanical resonance frequency and quality factor through $b \propto m_{eff} f_0 / Q$. Thus, the ideal force sensor would have low mass, relatively low tension, and a high-quality factor.

Low-dimensional materials such as nanotubes and two-dimensional crystals, including graphene, have begun to see wide use as nanomechanical systems because of their inherently small mass and strong interactions with their environment(19, 20, 48, 95). Graphene is exceptionally well-suited for nanomechanical systems because it

also offers high intrinsic stiffness, strength(96), and amenability to strain tuning(81). Additionally, fabrication of large-scale arrays of graphene drumhead resonators is well developed(84) and drumheads are frequently used in nanomechanical experiments. However, although various techniques have been used to increase the quality factor in graphene drumheads, such as using of few-layer reduced graphene oxide membranes(97), or larger area graphene drumheads(66), they also add significant mass, leaving the force sensitivity unchanged. Thus, new approaches are required to realize graphene mechanical resonators that both have high quality factors and the ultra-low mass.

Tailoring the geometric shape and clamping of nanomechanical resonators is a promising alternative to achieve reductions to the mass while also lowering tension and damping(35, 41). Although such geometric tuning of graphene is still in its infancy, the few studies that have explored geometric effects indicate that shape and size has a large role in the mechanical properties of graphene resonators. For example, low tension H-shaped graphene suspended structures(67) were found to display order-of-magnitude increases to the mechanical Q along with a significantly reduced damping coefficient. In contrast, doubly-clamped beams(54) show quality factors and mass similar to graphene drums, indicating the need for more detailed studies to elucidate the role of geometry and tension on the mechanical properties of graphene resonators. However, the arbitrary shaping of suspended graphene remains elusive, which is in part due to current fabrication approaches, so many potentially compelling device geometries, even as simple as a singly clamped cantilever, have yet to be fully explored.

Fabrication of arbitrarily patterned graphene mechanical structures via resist-based lithography(54, 58) and planar processing has not been achieved. This is partly due to the cumbersome, multistep nature of clamping and suspending such devices, which involves multiple lithography steps, thin film depositions, dry and wet etching, and critical point drying. In many cases, the etching chemistry needed to define the mechanical clamp is incompatible with graphene, which precludes the approach

altogether. An alternative patterning approach, one that circumvents challenges seen in traditional lithography, has emerged that employs Focused Ion Beam (FIB) milling(98) of free-standing graphene. This approach has been used to pattern graphene into diffraction gratings(99), nanopores(100), and nanowires(101). The FIB technique has seen little use as a method to pattern single-layer graphene nanomechanical systems and has presently only been used to fabricate low-aspect ratio cantilevers(102) with no associated improvements to the Q. Thus, the viability of FIB milling as a general approach to achieve arbitrarily shaped graphene mechanical resonators remains an open question. Furthermore, because the geometric parameter space of graphene nanomechanical resonators is largely unexplored, it is unknown which shapes or clamping configurations possess less mechanical damping.

In this section, we demonstrate that FIB milling is an effective tool to shape free-standing graphene membranes into a wide variety of two-dimensional geometries, with device features ranging in size from several tens of nanometers to a few micrometers. Many of these structures, such as crosses, triangular cantilevers, and tethered cantilevers, have not been previously observed in a suspended two-dimensional material. Furthermore, we employ optical techniques to actuate and detect the mechanical motion of the graphene structures in order to characterize their mechanical properties, such as the Q, resonance frequencies, and force sensitivities. We compare unmodified drumheads to the FIB milled structures and identify that singly-clamped graphene devices can display order-of-magnitude enhancements to the quality factor while also reducing mass, making them an ideal candidate for graphene force sensors. We also demonstrate that shape can be used to introduce mechanical nonlinear behavior and also stabilize the frequency of devices under optical probing, showing the broad generality of nanomechanical properties that may be tuned through geometric shape.

4.2 Fabrication

The starting template for the shaped graphene devices is a graphene sheet suspended over a pre-patterned circular hole, forming a freely suspended graphene mechanical resonator with uniform edge clamping (*i.e.* a circular drumhead). We used commercially available single-layer graphene on holey silicon nitride grids (Ted Pella Part# 21712) for device templates(98, 99). Each grid contains a periodic array of several thousand individual circular drumheads, each with a diameter of 2.5 μm. To characterize the quality of the graphene prior to milling, we used transmission electron microscopy (TEM) and Raman microscopy. We observe some degree of surface contamination under TEM and SEM, which is an unavoidable byproduct when transferring CVD graphene using standard polymer-based techniques (Figure 4.1 and Supplementary Figure A.1). The Raman spectrum typical of low-defect, annealed monolayer graphene (Supplementary Figure A.2) that is relatively free of defects (103). We also use selected area electron diffraction (SAED) to confirm the crystalline, single-layer nature of the graphene (Supplementary Figure A.3).

Graphene resonators were shaped by irradiative milling of the suspended graphene membrane template with a focused ion beam or FIB. The "positive-tone" FIB milling process sputters material from specified regions of the membrane to obtain the desired device geometry. Milling was accomplished with a commercial gallium FIB (FEI Helios 600i Ga+ SEM-FIB) operated in vacuum at 30 kV and with 1.1 pA ion currents to minimize damage due to the spread of the ion beam. Typical ion doses required to mill through the graphene were $8.5 - 17$ pC/μm^2, corresponding to $0.06 - 0.12$ μm^2/s milling rates. Prior to fabricating devices, a brief snapshot image was taken with the FIB to orient the milling patterns. Snapshots were taken of drumheads as well. During the snapshot, we apply an ion dose of ~.0007 pC/μm^2, which is 10000 times less than the dose required to mill graphene. Examples of the FIB milled geometries are shown in Figure 4.1 and Supplementary Figure A.4. To demonstrate the flexibility and robustness of our technique, we fabricated similar devices from graphene suspended over cavities (Supplementary Figure A.4).

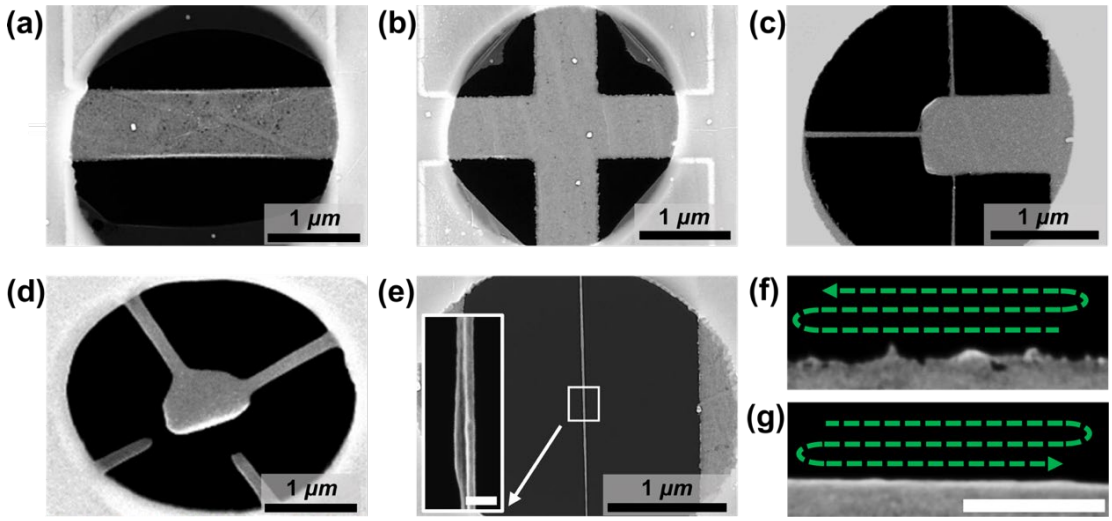

Figure 4.1: SEM images of FIB-fabricated graphene NEMS. (a) Graphene doubly-clamped beam with 600 nm width. (b) Cross with 600 nm bar widths. Peeled areas of graphene are visible around the edge of the circular hole. (c) Tethered cantilever with aspect ratio of 1.66 achieved through use of stabilizing tethers (d) Triangular cantilever with a 90-degree tether angle. (e) Graphene scroll with width ~25 nm spanning across the entire hole with a 100:1 aspect ratio. Rolling of the graphene is visible in the inset (Scale = 70 nm). (f) Edge of a graphene beam where the ion beam mills away from the device with local RMS roughness of 2.47 nm (g) Edge of a graphene beam where the ion beam mills towards the device with local RMS roughness of 0.23 nm.

We use four types of cuts to pattern the graphene. These cuts include a vector cut, where a single line is milled into the graphene with width determined by the Gaussian beam waist of the ion beam, a raster cut, where the beam passes over an area in many passes, and two types of single-pass directional raster cuts, shown in Figure 4.1f-g, where the serpentine raster is either directed away from or towards the device. The type and order of cuts dictated possible device geometries. In some cases, using the incorrect sequence of these cuts led to device failure.

We monitored the entire cutting process using the non-destructive scanning electron microscope (SEM) imaging system before, during, and after fabrication (Figure 4.2). This allowed us to fabricate devices in regions with fewer particulate contaminates, holes, and folding (multilayer) defects, while also allowing us to determine successful cutting strategies for each of the device geometries. For instance, we could observe if a particular cut caused device failure through tearing or rupturing and subsequently

adjust the cutting sequence or type accordingly. Post-fabrication SEM characterization generated maps of devices, which were used during optical characterization to locate and probe specific devices. We used the FIB patterning approach described above to generate a variety of device geometries. These include crosses, beams, two cantilever style geometries (Figure 4.1), coupled beams (Figure 4.2b), meshes, scrolls, and tethered trampolines (Supplementary Figure A.4). Many of these geometries have not been previously achieved in suspended graphene. This patterning technique achieved feature sizes as narrow as 10 nm, pitch resolution less than 100 nm, and length-to-width ratios as high as 250:1. We also generated edge-clamping configurations ranging from double-clamping (*e.g.* in simple beams) to 48 independent clamps (*e.g.* in trampolines), with clamp widths ranging from 10 nm to 1 μm.

Each device architecture required a particular, manually defined sequence of FIB cuts, which was largely determined by the need to manage tension or strain during device fabrication. Tensioned graphene, unlike many commonly FIB milled bulk materials(104), such as silicon or diamond, is susceptible to warping, tearing, and rupturing due to asymmetric strain that is introduced during FIB milling. An illustration of tension-driven failure in a simple beam device is shown in Figure 4.2a. In this example, an initial raster cut removed graphene from the left half of the graphene drumhead, resulting in tension originating only from edge-clamping on the right half of the membrane. As milling proceeded on the right side of the drumhead, tension became concentrated near the center causing the device to stretch and then tear. We observed that larger milled regions led to a greater tension imbalance around small device features, limiting FIB milling to areas of less than ~500 nm in lateral dimensions when tension asymmetries were not managed and controlled. However, once the proper cutting sequence for a given geometry was established, fabrication yield was near 100%.

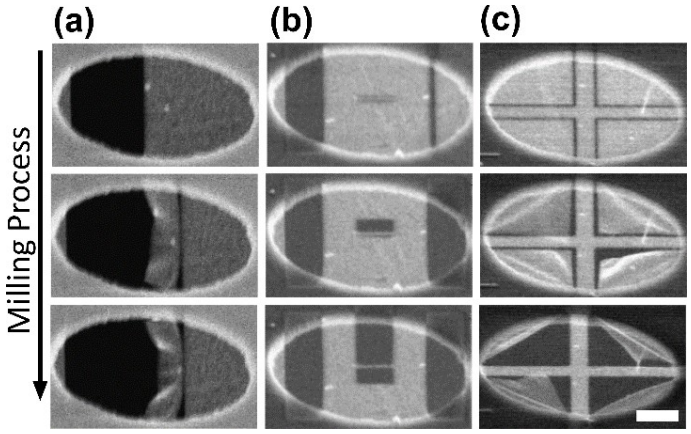

Figure 4.2: FIB milling process for different graphene NEMS geometries. (a) Sequence of images showing a failure during fabrication of a doubly-clamped beam. (b) Successful fabrication of a coupled beam. The narrow central ribbon is protected from excess tension by two isolating vector cuts in the center of the structure. (c) One of several fabrication methods for a cross. Vector cuts are used to outline the cross shape. Then, a parallel raster peels the graphene away from the device. (Scale Bar = 500 nm).

We identified several methods to controllably relieve tension in the devices to avoid tension-driven failure. These include specifying the mill direction, specifying the order of particular cuts, and using single-pass or multiple pass milling. Simple structures such as crosses and doubly-clamped beams could be shaped with high repeatability through several methods, including directional single-pass raster cuts or a vector cutting method shown in Figure 4.2c. In the vector cutting method, a series of vector cuts are used to etch the outline of the shape into the graphene. The ion beam then rasters around the region, causing the graphene to peel away from the device. For most geometries, this vector cutting technique proved to be the most robust approach.

The coupled beam geometry, consisting of two wide doubly clamped beams (500 nm wide, 2.5 μm long) coupled together through a narrow ribbon (50 nm wide, 500 nm long), required management of tension around the central ribbon, which was very sensitive to asymmetric tension. One successful milling sequence, shown in Figure 4.2b, starts by defining the narrow ribbon vector cuts on both sides to isolate it from tension imparted during later milling. Then, a single pass raster on both sides of the

drumheads leaves a single 1.5 μm by 2.5 μm beam. Finally, single pass raster cuts on either side of the thin ribbon to leave the freestanding, coupled beam geometry. This structure is the first example of coupled beams in graphene, which have been previously shown(105) to display complex non-linear dynamics and chaos in resonators fabricated from bulk materials.

We were able to fashion the graphene into nanoribbons with widths of 40 nm and lengths of 2.5 μm, which we achieved using a single pass directed raster towards the ribbon. The raster direction here was crucial, as outward raster cuts or multiple pass raster cuts frequently resulted in failure of the tether. In contrast, an inward raster severs the edge clamp first in order to relieve strain and thereby stabilize the ribbon as it forms. By reducing the ribbon width below ~40 nm, the ribbon spontaneously narrows and changes into a structure resembling a nanoscroll(99). We achieved nanoscrolls with widths of 10-15 nm that spanned the entire 2.5 μm width of the drumhead template, yielding an aspect ratios as high as 250:1. The nanoscroll and nanoribbon structures were fashioned as stand-alone devices (Figure 4.1e) and also served as tethers in more complex structures such as tethered cantilevers (Figure 4.1c) and trampolines (Supplementary Figure A.4).

The raster direction relative to the edge of a device feature also affected the RMS roughness of the edge. A raster away from an edge with a single pass (Figure 4.1f and Supplementary Figure A.1) resulted in a local edge roughness of 2.47 nm. A raster towards an edge resulted in a smoother edge with an edge roughness of 0.23 nm (Figure 4.1g). Based on SEM, these smooth edges are likely due to scrolling similar to that evident in the device in Figure 4.1d. Edge roughness can lower the thermal conductivity(106), reduce electron mobility(107), and increase damping(108) of graphene devices and reducing the edge roughness using FIB milling could be an effective route towards improving these characteristics.

FIB milling introduces some degree of defects and contamination when milling bulk materials or graphene(109). We investigated these effects with Raman microscopy

(WITEC alpha300 Raman microscope with a 532 nm excitation laser) and transmission electron microcopy (TEM). Even at the relatively low ion doses used in this work, both the lightly dosed drumheads and the milled devices had Raman spectra consistent with increased disorder in the graphene (Supplementary Figure A.2). This is in accord with previous studies of FIB milled or otherwise patterned monolayer graphene(110–112). We attribute this damage to deposition of amorphous carbon during SEM imaging or FIB milling, to the FIB snapshot images taken to orient the milling, and to the FIB fabrication itself. We also expect the cut edges in the FIB milled devices to contribute significantly to the disorder in the observed Raman data(113). To confirm that the fabricated devices are still crystalline, we perform SAED using TEM on the graphene before and after FIB irradiation, and we observe no difference in the diffraction patterns (Supplementary Figure A.3), so milled devices remain crystalline. Since all the devices studied in this work were exposed to a similar, relatively low amount of ion irradiation, we attribute the enhanced mechanical properties described below to the geometric shape rather than the FIB irradiation. Damage due to the FIB process could be reduced in future work through use of more localized etching processes, such as helium FIB milling(111) or water-assisted etching(112), or by a post-fabrication annealing step.

4.3 Mechanical characteristics

Having used FIB milling to demonstrate robust and reproducible control over the geometric shape of suspended graphene mechanical structures, we now turn to discussing the mechanical properties of some of these structures. Our central data include amplitude and phase spectra obtained via Michelson interferometry(114) modeled with a driven damped harmonic oscillator to infer the Q, damping, mode frequencies (f_n), and corresponding amplitudes. We optically drove the mechanical resonators with an amplitude modulated 445 nm blue laser, with tunable power output, P_0. The power of the blue laser incident on the drumheads is given by, $P = \frac{P_0}{2}(1 + \cos(2\pi f_{drive} t))$ which has an AC term, leading to photothermal actuation(66, 84), as well as a DC term, leading to optical heating and increased strain in the devices(48). A detailed diagram of the optical experiments is shown in Supplementary Figure A.5.

We first probed the amplitude response of drumhead resonators (Figure 4.3) to establish a baseline for comparisons with etched geometries. Although these drumheads were not ion milled, they were irradiated through the initial 'snapshot' of the devices. We measured eleven 2.5 μm diameter drumheads and found a center frequency $f_{\$}$~21.5 and quality factor Q~48.9, with standard deviations across the devices of σ_{4}~4.79 MHz and $\sigma_{\#}$~13.0, yielding a damping coefficient of b~2.7 pg/s. From $f_{\$}$, we calculate a minimum possible strain of strain of $\epsilon \sim 1 \times 10^{-\hat{}}$ (Section A.1), which is comparable to previous measurements of drumheads using graphene grown via chemical vapor deposition and transferred using sacrificial polymer layers(66).

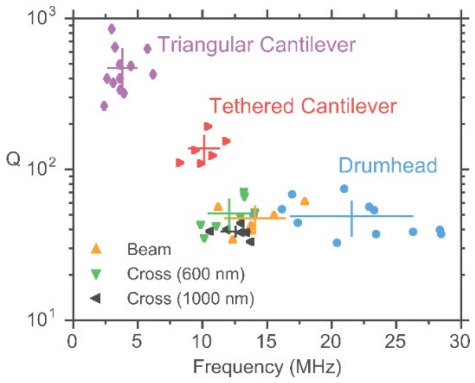

Figure 4.3: Resonance frequencies and quality factors for FIB shaped devices. Error bars indicate the standard deviation of f_0 and Q for a given device geometry. Triangular cantilevers of tether angles ranging from 15 to 90 degrees are grouped together.

We find the mechanical properties of etched geometries differ significantly from drumheads. In general, the etched geometries have lower resonance frequencies and less damping. Figure 4.3 shows the measured frequencies and quality factors for several device geometries. The beams (with width of 1000 nm) and crosses (with cross bar widths of both 600 nm and 1000 nm) display lower $f_{\$}$ and similar quality factors compared to drumheads. Therefore, the average damping relative to drumheads decreases by ~50% for the 600 nm cross and more modestly for the beams and 1000 nm crosses. Damping reduction is more pronounced for the cantilever geometries; for the tethered cantilever (Figure 4.1c), we observe $f_{\$}$~10.1

MHz with σ_4~1.22 and Q~137 with $\sigma_\#$~31.5 leading to an average damping of 7.5% that of the drumheads. For the triangular cantilever devices (Figure 4.1d), we find $f_\$$~3.79 MHz with σ_4~1.16 and Q~468 with $\sigma_\#$~167 and a mechanical damping coefficient that is 1.1% of that seen in the drumheads.

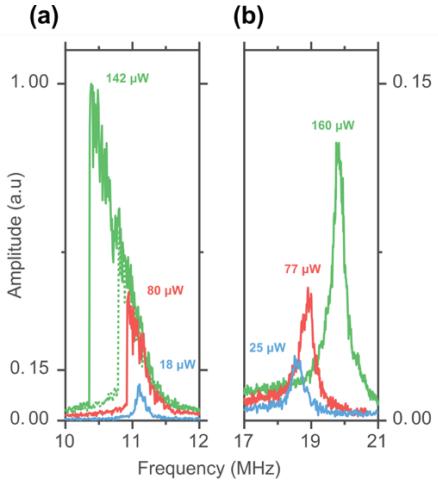

Figure 4.4: Comparison of the amplitude response of a tethered cantilever and of an unmodified drumhead. (a) Amplitude response of a tethered cantilever device at increasing optical drive powers. At high drive power, the resonance frequency lowers and the amplitude response curve become multi-valued and displays hysteresis; traces going from high to low frequency are shown solid green, while those going from low to high frequencies are shown in dashed green. (b) Amplitude response for a typical drumhead device; plotted on the same scaled y-axis as (a) and at increasing drive power. A 10-fold decrease in the amplitude response is observed for the drumhead compared to the tethered cantilever. A trend towards increasing frequency with higher optical drive powers is seen with the drumheads, likely due to thermal contraction of the graphene as it is heated by the DC component of the optical drive.

The cantilevered geometries presented here are unique due to their large aspect ratios, up to 1.66 in this work compared to less than 1 for previously fabricated graphene cantilevers(102). We observe a significantly increased amplitude response for both types of cantilevers, roughly by a factor of 10 compared to drumheads at similar optical drive powers (Figure 4.4). This result is expected due to the lower resonance frequencies and larger displacements of cantilevers. We are able to use this transduction sensitivity to resolve a thermally driven resonance for triangular

cantilever devices with no external drive (Supplementary Figure A.6), which we are unable to see for any other device geometry.

We also observe a markedly enhanced nonlinear response, typical of a softened duffing oscillator(58) for all measured tethered cantilevers at low optical drive powers of $\sim 20 - 40$ μW. For comparison, drumheads were driven up to ~350 μW with no discernable departure from a linear response. This can be understood by realizing that the onset of geometric non-linearity in cantilevers scales with the aspect ratio(115). Another factor could be a large strain-driven tension in the tethers. Finite element simulations (Supplementary Figure A.7) on the tethered cantilever geometry show that large strain-driven tension arises in the tethers during mechanical oscillations, which could contribute to the observed non-linear behavior in this structure.

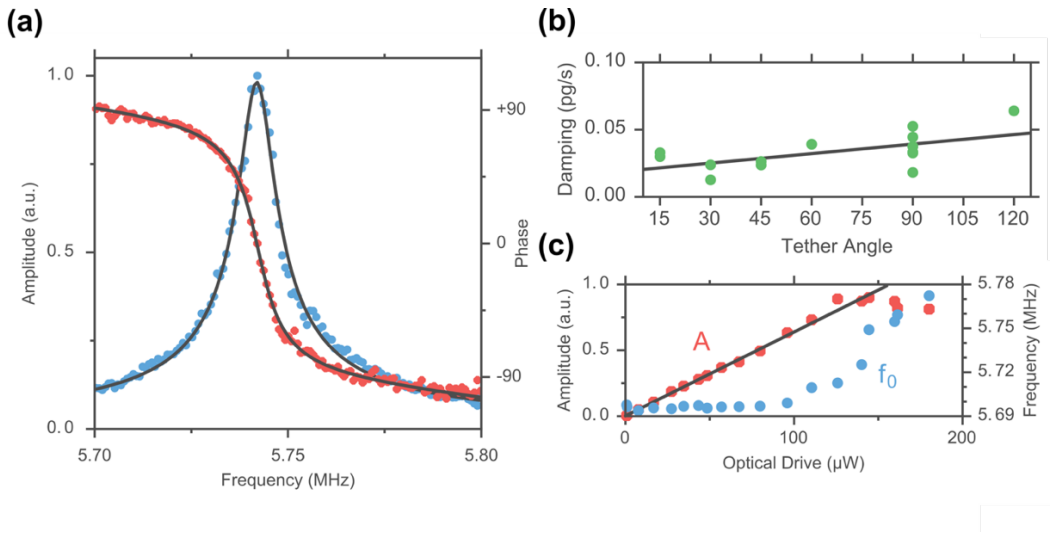

Figure 4.5: Mechanical response of triangular cantilever. (a) Amplitude (blue) and phase (red) response of a device with a 90-degree tether angle. The response curves are fit to a driven damped harmonic oscillator model (black lines) with a $Q = 628$. (b) Mechanical damping plotted against the tether angle for the triangular cantilever devices. A trend towards higher dissipation is seen as the frame angle increases. (c) Amplitude (red) and frequency (blue) as function of optical drive power. The black line is a linear fit to the amplitude response data. A linear response is observed for low drive powers. At high drive powers, a reduction in the measured amplitude and an irreversible increase to the frequency is seen, likely due to structural changes in the device.

Similar non-linearities have been exploited in other nanomechanical systems to reduce noise(116, 117), tune quality factors(118), couple mechanical modes(29), or as a means to improve mass sensitivity(119). Although this type of non-linearity has been observed previously in graphene(66, 67, 95), the comparative drive powers reported here to achieve a large non-linear response indicates that the tethered cantilever geometry could be an ideal device architecture for future studies of non-linear graphene nanomechanics.

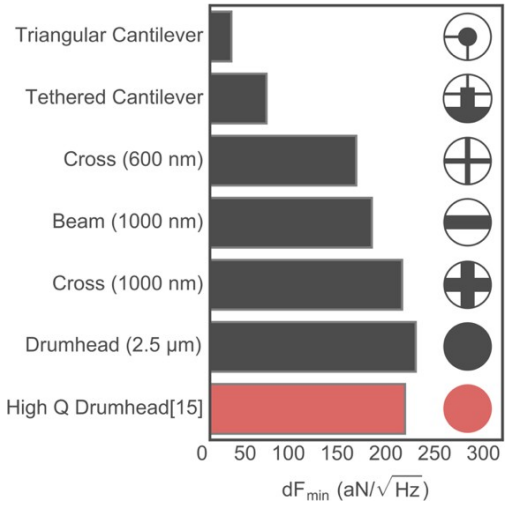

Figure 4.6: Role of geometry on the minimum detectable force of graphene nanomechanical resonators. Triangular cantilevers displayed the lowest minimum detectable force of all measured devices, with a value of ~22 aN/$\sqrt{\text{Hz}}$. For context, the characteristic force sensitivity (~200 aN/$\sqrt{\text{Hz}}$) for a high-quality factor graphene drumhead(66) is indicated in red.

In terms of reducing damping, the triangular cantilever geometry proved the most promising. This geometry consists of two ~750 nm long, ~200 nm wide tethers supporting a central platform (Figure 1.2d) with the angle between the tethers ranging from 15 degrees to 120-degrees. Due to the low bending rigidity of graphene, many of the devices flip upwards to some degree (Supplementary Figure A.4). There could be an additional degree of stabilization of the cantilevers due to contamination leftover from the fabrication process. A typical amplitude response curve for a device with a 90-degree tether angle is shown in Figure 4.5a; this device has a $Q = 628$. From

this data, we see that the triangular cantilevers generally have frequencies 80% lower than drumheads but have higher Q, and lower mass, yielding a damping coefficient that is two orders of magnitude smaller than the value for drumheads. We observe that the mechanical damping decreases with tether angle, reaching its minimum value at 30-degrees. Our data from these measurements is summarized in Figure 4.5b. A device with a 30-degree tether angle gave a measured Q of 849, which is the highest Q to date for a graphene cantilever at room temperature(102). In this case, the damping dropped to 0.47% the value for drumheads. One key difference between the triangular cantilever and the other device geometries is that its structure cannot sustain much in-plane tension, suggesting that low stress, low tension graphene mechanical resonators may yield lower damping. Because smaller angles support less tension, we would expect them to yield higher Q, in accord with our findings.

To further explore the role of tension in triangular cantilevers, we investigated the effect of optical drive power on the amplitude and resonance frequency, both shown in Figure 4.5c, for a device with a 90-degree tether angle. First, we find the amplitude increases linearly and reversibly over a ~100 μW range of optical drive, setting a minimum dynamic range of 33 dB. Furthermore, the response remains Lorentzian over the entire power range, unlike the tethered cantilevers, which go non-linear at relatively low power. Over the same power range, we find that $f_{\$}$ remains relatively constant. The invariability of $f_{\$}$ in the reversible regime and the broad linear response give a strong indication that any structural changes due to power absorption (*i.e.* thermal expansion or contraction, larger oscillation amplitude) do not lead to appreciable increases in tension in these devices, thereby lending validation to the claim that the triangular cantilever cannot sustain much in-plane strain. In contrast, drumheads experience large frequency shifts as the optical drive power is increased (Supplementary Figure A.8) due to the device and substrate heating. The insensitivity of the triangular cantilever frequency to optical drive power is attractive for force and mass sensing, since small changes to the resonator environment due to pump laser noise and other sources do not cause undesirable changes in the frequency. At higher drive powers (above 120 μW), we see irreversible changes, with

$f_{\$}$ increasing and the amplitude decreasing. Post-measurement SEM imaging reveals that devices driven past the reversible regime suffered from structural deformation such as out-of-plane buckling and kinking, leading to a shorter cantilever, smaller reflective surface area, and, consequently, the observed increase in resonance frequency and decrease in transduction sensitivity (Supplementary Figure A.4).

4.4 Discussion

The amount of pre-tension present in the shaped devices relative to the drumheads offers insight into the observed decrease in damping seen in all FIB cut geometries. Previous work(66) has identified local strain coupling to surface defects as the most likely source of damping in fully clamped graphene drumheads. Of the geometries considered here, the triangular cantilever geometry has the lowest tension and thus we would expect it to have the lowest strain-induced dissipation, consistent with our measurements. Similar investigations of low-tension(84) or minimally clamped(67) graphene mechanical resonators have also observed relatively high quality factors and low damping, which agrees with our result. Thus, strain reduction in devices could be a possible route towards high quality factor, ultra-sensitive graphene devices.

The triangular cantilevers we present here operate in a unique mechanical regime characterized by small mass (0.6 fg), low frequency (several MHz), large amplitude response, and high quality factors (up to 849). This regime offers the potential for exceptional mass and force sensitivity. For example, the theoretical minimum detectable mass(15) for our most sensitive device is 30 zg, given by $\delta M_{!1"} \approx \frac{2}{@4_!} 10^{\%\_/+\$}$, where DR is the minimum dynamic range and b is the damping coefficient . This value could be significantly improved through use of a higher dynamic range optical or electronic transduction technique(20, 67, 81). We estimate the minimum theoretical detectable force(94) of ~14 aN/$\sqrt{\text{Hz}}$, given by $\delta F_{!1"} = \overline{08\pi k_2 T m_{344} f_{\$}/Q}$, where m_{344} is the effective modal mass defined in Eq. 2.3, k_2 is Boltzmann's constant, and T is the resonator temperature for the most sensitive device measured. In contrast to drumheads, which have a force sensitivity of several hundred aN/$\sqrt{\text{Hz}}$ for

all sizes (66), we see a strong dependence on the device geometry. We compare the triangular cantilevers to the drumheads, beams, and crosses (Figure 4.6) and observe a factor of ~10 enhancement to the force sensitivity, corresponding to a reduction of ~100 in the mechanical damping. These triangular cantilevers, along with the recently reported lithographically patterned H resonator, constitute the best reported force sensitivities for room temperature graphene mechanical resonators(67). It is noteworthy that both of these devices utilize patterned, low-tension graphene. The FIB milling technique presented here offers an excellent method to further explore the geometric dependence of the force sensitivity, since it allows for rapid prototyping and characterization of desired device architectures.

4.5 Conclusion

In this work, we use FIB milling to efficiently fabricate suspended graphene structures into a wide variety of novel geometries. All shaped geometries exhibited a decrease in mechanical damping relative to the drumheads. Furthermore, we find that cantilever-style structures display additional sought-after attributes including easily accessible non-linear behavior, large transduction response, high-Q, and state-of-the-art force sensitivities, while also operating in the previously inaccessible low-tension regime. Importantly, this result was achieved strictly though simple geometric shape tuning of commercial graphene, in the absence of complex fabrication techniques or ultra-clean graphene. Our findings indicate a close relationship between geometry, tension, and mechanical characteristics: structures that support less tension, such as the triangular cantilever, have lower dissipation, while structures with concentrated tension, such as the tethered cantilever, exhibit strong non-linearity. Thus, our FIB shaping technique offers a prescription to tailor key nanomechanical properties of graphene through geometry. In particular, our work gives a well-defined, repeatable approach to achieve high-Q, low-mass graphene devices. Our approach can be easily extended to shape graphene for other nanomechanical device applications, such as creating coupled mechanical resonators or phononic crystal cavities. It can also readily be applied to shape other 2D materials, such as hexagonal boron nitride and molybdenum disulfide, to explore the interplay

between geometry and optical and electronic properties not present in graphene, such as photoluminescence and piezoelectricity.

4.6 Bridge

In this chapter, we developed a new method to engineer the geometry of graphene NEMS using FIB milling. This approach allowed us to tailor various mechanical properties such as frequencies, mechanical non-linearities, and quality factors. The ability to control these key parameters and the shape is an important first step to array-based applications of graphene NEMS. In the next chapter, we will use scanning optical interferometry to study how the mode-shape can be tuned using the FIB milling approach.

CHAPTER V

ENGINEERING THE MODAL SHAPE OF GRAPHENE NANOELECTROMECHANICAL SYSTEMS USING FOCUSED ION BEAM MILLING

From D. Miller, A. Blaikie, and B. Carter., B. Alemán, Engineering the Modal Shape of Graphene Nanoelectromechanical Systems Using Focused Ion Beam Milling, *2018 IEEE 13th Nanotechnology Materials and Devices Conference (NMDC).* 1-4. (2018). I performed the fabrication, experimental measurements, data analysis, and am the primary author on the publication. Benjamín Alemán is my supervisor.

5.1 Introduction

Controlling the modal shape of a nanoelectromechanical system (NEMS) is vital for applications ranging from improved point-mass sensing(32) to high quality-factor (Q) nanomechanics(34). Mechanical structures like trampolines and tapered beams in silicon-nitride have attracted increasing interest lately due to possessing an extremely high Q(35). Graphene NEMS(20) promise to merge the benefits of an engineered mode shape with graphene's extraordinary strength and low mass, but obtaining device shapes other than simple circular or square drumheads or beams has been a challenge. However, even a modest degree of shaping can improve device characteristics. H-beams, for example, can have a dramatically higher Q(67). Standard nanofabrication techniques, such as reactive ion etching and critical point drying, have low yields for high-aspect ratio graphene resonators, making it difficult to rapidly prototype appealing device geometries, such as trampolines. Our group recently demonstrated a simple method to achieve arbitrary geometries in graphene NEMS using focused ion beam (FIB) milling(120), which requires only commercially available pre-suspended graphene drumheads.

Continuum membrane mechanics predicts the dynamic mode shapes of these geometries, but the models cannot easily capture the effects of surface defects (*e.g.* wrinkles, folds, ripples), edge effects, and anisotropic strain(79). Therefore, a direct experimental test of the mode shapes is needed to assess the ability to engineer mode shape in graphene NEMS.

Here, we fabricate and characterize graphene NEMS with several novel geometries including straight beams, tapered beams, and trampolines. We drive the devices electrostatically and measure the mode shapes with scanning interferometry and find that these shapes agree well with the predictions of finite element modeling (FEA) of thin membranes. We measure the resonance frequencies and quality factors for simple drumheads as well as trampolines and find that trampolines display moderately increased frequencies. Our work here demonstrates that FIB milling can be used to obtain well-defined mode shapes in a graphene NEMS and improve quality factors.

5.2 Methods

The engineered geometries are cut out of a circular graphene drumhead template (Figure 5.2a). We fabricate the initial graphene drumhead resonators over holes etched in SiO_2 on Si^{++}. The graphene is placed over the holes using a standard dry-transfer technique(74) and is contacted to a Ti/Pt electrode for electrostatic actuation. We shape the template resonators using a single-pass focused ion beam milling (FIB) approach optimized for cutting pre-suspended graphene(120). SEM and FIB were performed in a FEI Helios dual-beam system, which used Ga^{+} ions. Typical milling parameters are a 1 ms dwell time, 1.1 pA of beam current, and an accelerating voltage of 30 kV. Milling time per device is ~1 minute.

The graphene resonators are actuated by applying an AC gate voltage (V_{AC}) between the resonator and the Si^{++} and the device. A DC gate voltage (V_{DC}) is used to increase the actuation amplitude and tune the resonance frequency(20). We keep V_{AC} between 10 mV and 60 mV to remain in the linear-response regime. We measure the

mechanical response of the devices using a home-built scanning interferometer and lock-in amplification. We focus a 633 nm laser onto the graphene resonators using a 40x, 0.6 NA objective, yielding a spot-size of ~1 micron. By scanning the laser across the device and measuring the on-resonance vibrational amplitude at each point, we can reconstruct the mode shape of the nanomechanical devices (Figure 5.1a). Measurements are performed at ~10^{-6} Torr to reduce the effect of gas damping and the laser power is kept <10μW to reduce photothermal heating.

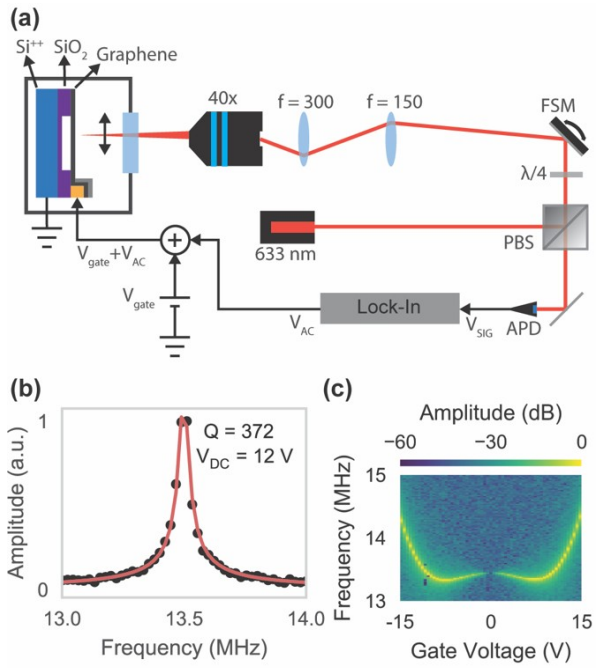

Figure 5.1: Experimental setup. (a) Diagram of experimental setup used for nanoelectromechancial measurements. FSM: Fast scanning mirror. PBS: Polarizing beam-splitter. APD: Avalanche photodiode. $\lambda/4$: Quarter waveplate. (b) Frequency response of a tapered beam with V_{DC} = 12 V. We measure a Q of ~372 and a resonance frequency of ~13.5 MHz. (c) Frequency tuning curving while varying V_{DC}. The resonance frequency sweeps upwards from ~13.5 MHz at V_{DC} = 0 V to ~14.5 MHz at V_{DC} = 15 V.

5.3 Results

We fabricate graphene NEMS with several novel geometries including trampolines (Figure 5.2b), tapered beams (Figure 5.3a), and straight beams (Figure 5.3b) using single-pass FIB milling. For the tapered beams and trampolines, annular line cuts are used to peel graphene away from the tethers. The regions of collapsed graphene that have peeled away from the finished device are visible in Figure 5.2b around the edge

of the hole. For the straight beam, a single-pass serpentine cut oriented away from the device removes the graphene. Compared to conventional bulk-milling approaches, our single-pass technique releases tension in a more even and controlled manner, offering significantly higher-yield for high-aspect ratio structures such as trampolines. We achieve near 100% yield for tapered beams and trampolines when starting from drumheads without visible tears. Yield for the straight beams is significantly lower, likely due to the visible appearance of wrinkles along the length of the beam. The tapered structure in both the tapered beams and trampolines reduces this wrinkling, which greatly improves the yield.

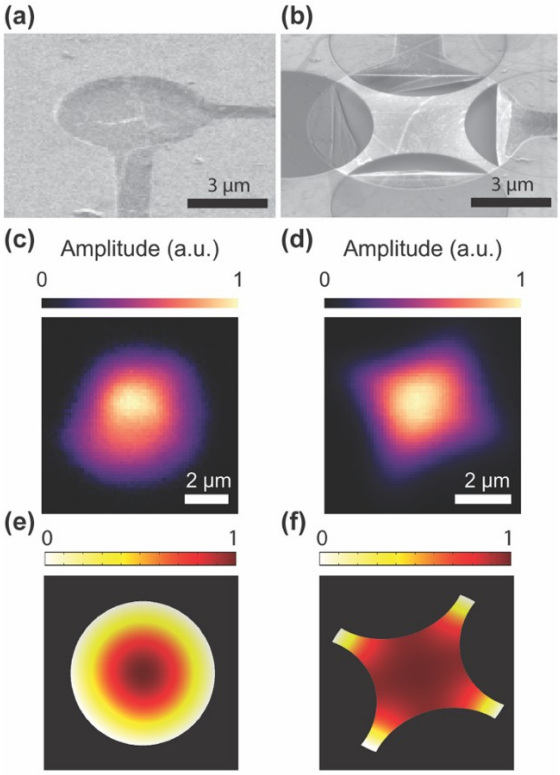

Figure 5.2: Mode shapes for graphene drums and trampolines. (a) SEM image of an 8 μm diameter template graphene drumhead. (b) SEM image of an 8 μm diameter graphene trampoline resonator. The regions of cut graphene which have been peeled away from the device are clearly visible at the edge of the hole. (c) Mode shape for a graphene drumhead. The mode shape is roughly circular but somewhat asymmetric. (d) Mode shape for a graphene trampoline. The mode shape is roughly square but is significantly more symmetric than the fully-clamped drumhead. (e) FEA simulation of drumhead. (f) FEA simulation of a trampoline resonator showing the rectangular mode shape and high amplitude throughout the central platform

We first characterize the electromechanical performance with optical interferometry and find resonance frequencies between 10 and 30 MHz depending on the specific device geometry. Figure 5.1b. shows a typical mechanical resonance peak for a tapered beam with length of 8 μm, measured at V_{DC} = 12 V, with a frequency of 13.5 MHz and a Q of ~372. As we sweep V_{DC} from 0 V to 15 V, we find that the resonance frequency increases from ~13.5 to ~14.5 MHz due to increased electrostatic tension while the Q decreases from ~1000 to ~350, which we attribute to increased Joule dissipation(121) (Figure 5.1c). This type of tuning curve is characteristic of a graphene NEMS and shows that the FIB milled geometries maintain the desirable electromechanical properties of graphene drumheads. Although we highlight a tapered beam here, all devices display similar electrostatic properties.

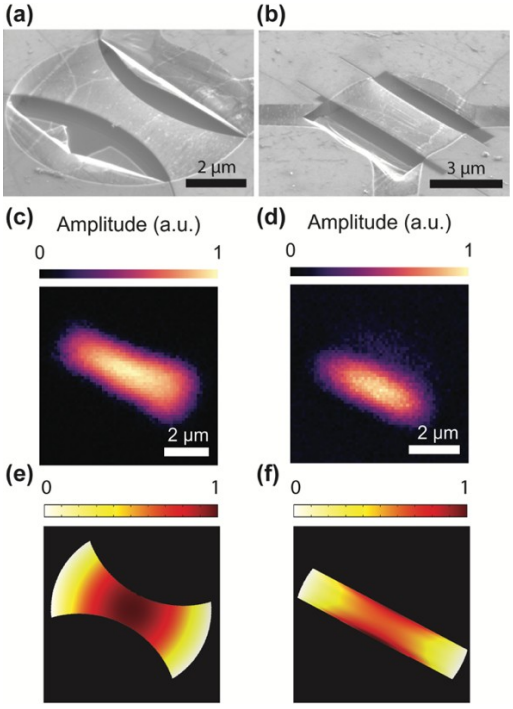

Figure 5.3: Mode shapes for graphene beams and tapered beams. (a) SEM image of an 8 μm long tapered beam. (b) SEM image of an 8 μm long straight beam. (c) Mode shape of a tapered beam. The modal amplitude is concentrated near the middle of the beam. (d) Mode shape of a straight beam. The modal amplitude is distributed throughout the beam. (e) FEA simulation of the tapered beam showing concentration of modal amplitude near the central taper. (f) FEA simulation of straight beam showing significant amplitude throughout the beam.

We next perform a high-resolution, two-dimensional scan of the measurement laser (60×60 points) over the resonators to elucidate their fundamental mode shapes, as described in Section 3.5. The drumhead (Figure 5.2a) mode appears slightly asymmetric (Figure 5.2c), which is often seen for drumhead modes since small imperfections in the clamping can cause deviations in the mode shape(79). However, when we remove most of the clamped edge to create a trampoline resonator (Figure 5.2b), we observe a square mode shape, which is significantly more uniform (Figure 5.2d). The measured trampoline mode agrees well with FEA simulations, which predicts a simple out-of-plane vibration much like a drumhead (Figure 5.2e-f)

We also investigate doubly clamped geometries, such as straight and tapered beams (Figure 5.3a). FEA simulations (Figure 5.3e-f) show that tapered beams localize the mode shape near the center of the beam significantly more than comparably-sized straight beams (Figure 5.3b.). Strain in a tapered beam is also maximal in the center, which has been shown to improve the quality factor(34). Indeed, when we compare the tapered beam (Figure 5.3c) to the straight beam (Figure 5.3d), we see that the mode has significantly higher amplitude at the center of the beam, relative to the clamped edges, confirming the result of the FEA modeling. This tapered beam

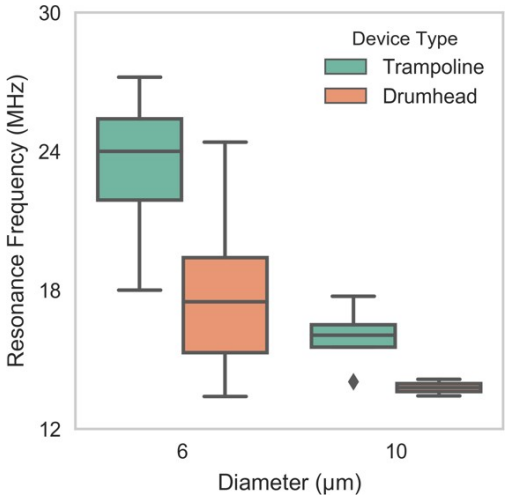

Figure 5.4: Resonance frequencies of 6 μm and 10 μm graphene drumheads (N = 16, N = 2) and trampolines (N = 6, N = 4). The average frequencies for the 6 μm and 10 μm drumheads are 18.1 MHz and 13.8 MHz while the trampolines frequencies are slightly higher, at 23.7 MHz and 16.0 MHz.

represents the first demonstration of strain-engineering in a graphene NEMS, offering the potential for greatly enhanced quality factors.

Finally, we compare the trampoline geometry to the drumhead geometry to test whether the more uniform mode shape translates into different mechanical properties. We measure the resonance frequencies (Figure 5.4) for a series of 6 μm diameter drumheads (N = 16). Then, we cut several of them into trampolines (N = 6) and measure the change to the mechanical properties. The drumheads have resonance frequencies around 18.2 MHz, which is typical for a 6 μm graphene drumhead(66). When shaped into trampolines, the average resonance frequency increases to 23.7 MHz. We see a similar trend towards increased frequencies for the 10 μm diameter devices, albeit with a smaller sample size. We also observe about a five-fold increase in the quality factor for both diameters of device. We attribute the increased frequencies and quality factors to the trampoline mode shape seen in Figure 5.2b. The trampoline geometry creates regions of high strain in the tethers, which has been shown to increase frequencies improve quality factors in high-aspect ratio silicon-nitride trampolines(35).

The ability to shape of graphene NEMS offers many potential applications not previously possible. For example, fabrication of coupled-resonators, which are desirable for mechanical resonator-mediated frequency mixing(7), can be readily achieved by leaving a central tether between two FIB-milled beams. Tailoring the geometry could also be greatly beneficial to point-mass sensing(32), where the frequencies of multiple mechanical modes are tracked simultaneously. The mode-shape could be engineered in such a way to maximize the frequency shift of the various modes due added mass on the resonator.

It should be possible to improve the device throughput by using higher beam currents or electron-beam induced etching. We use low ion currents (1.1 pA) in this work to maximize the resolution of the FIB milling, limiting our device throughput to ~1 Device/minute. However, beam currents 10^6 times larger are possible with modern ion sources, offering the potential for fabrication of 10^6 graphene NEMS/minute with

high-yield. The single-pass milling procedures we describe could also be used to fabricate devices with an electron beam via water-assisted etching(112), reducing the need for access to the relatively uncommon dual-beam microscopes.

5.4 Conclusion

In this work, we demonstrate the fabrication of graphene NEMS with engineered mode shapes, such as tapered beams and trampolines. We visualize the mode shapes of these devices and find they tend to be more symmetric and uniform than their non-engineered counterparts but still agree well with a membrane model. The FIB approach used here makes it possible to achieve highly complex geometries. We envision that future work could tailor the mode shape to a desired application, such as improving the Q of graphene mechanical resonators or enhanced point-mass sensing.

5.5 Bridge

In this chapter, we showed that the FIB-shaping approach can be used to precisely engineer the mode shape of graphene NEMS. In the next chapter, we will discuss the origin of the low Q in graphene NEMS and discuss ways to improve it.

CHAPTER VI

THE ROLE OF DISSIPATION DILUTION IN DETERMINING THE QUALITY FACTOR IN GRAPHENE NEMS

From an unpublished manuscript by Miller, D., Blaikie, A., Carter, B., Paulose, J., and Alemán, B. I performed the fabrication, experimental measurements, data analysis in collaboration with Blaikie, A. and am a co-primary author on the publication. Benjamín Alemán is my supervisor.

6.1 Introduction

In recent years, nanoelectromechanical systems (NEMS) have made significant contributions to many areas of science and technology, from the exquisitely precise detection of temperature(122), mass(123), local forces(123), and light(46) to the first tests of coherent quantum mechanics in macroscopic mechanical systems(8). Future uses for NEMS range from quantum bits(92), memories and busses to room-temperature neutral-particle mass spectroscopy systems(22). These uses demand NEMS with an even greater sensitivity and a higher degree of environmental isolation for improved classical(7) and quantum coherence(42), which in turn has driven a pursuit for NEMS in the extreme limit of low mass and high mechanical quality factor (Q)(15).

Despite much progress, the quest for both ultralow-mass and high-Q NEMS has fallen short. Silicon-nitride (SiN) beams and membranes possess the highest reported Q, but these bulk structures also have the highest masses, exceeding nanograms ($10^{-<}$ g). On the extreme end of the mass spectrum are low-dimensional NEMS resonators, such as suspended carbon nanotubes(17) or graphene sheets(20, 67, 81), which possess the lowest-possible mass density (linear or areal) of any material. Graphene NEMS have risen in prominence because of their scalability(54, 66), optical addressability(71), and large surface-to-volume ratio, making them particularly ideal

for sensing(59),(46) and optomechanical coupling(55, 56), (47, 48). Unfortunately, graphene NEMS have been hindered by an extremely low room-temperature Q(66), typically $Q \sim 10 - 100$.

Efforts to engineer a higher Q have been thwarted by a poor theoretical and experimental understanding of dissipation in graphene NEMS, but there are hints that the Q of graphene membranes can be described by dissipation dilution theory(34, 35, 40, 41) (DDT). According to DDT, the Q of a membrane is expected to increase with stress and scale linearly with its lateral size, both which have been observed with graphene drumheads(66, 68). In terms of thickness-to-radius aspect ratio(66) ($h/a \sim 10^{-=} - 10^{-\hat{}}$), mechanical stress(62) ($\sigma \sim 150$ MPa), and elastic modulus(96) ($E \sim 1$ TPa), graphene membranes are also physically similar to bulk, three-dimensional (3D) systems that are well-described by dissipation dilution (*e.g.* SiN strings and membranes(38, 44, 65)). On the other hand, the DDT for thin plates—the most relevant to graphene membranes—assumes a 3D structure, but experimental measurements of graphene's elastic properties (in-plane modulus, bending stiffness) often disagree with the 3D model(49). The predicted thickness-dependence(124) of the Q ($Q \propto h^{-8/+}$) also appears to fail for graphene membranes where Q should be in the range of 10,000 or higher because $h \sim 10^{-8\$}$ m. Verifying the DDT predictions have been further frustrated by large inconsistencies in the measurements of graphene's elastic properties—which vary with the measurement method(125, 126), the level of wrinkling(127), contamination, and strain(128), and device fabriction(129)—and because these properties have not been systematically measured and compared to the Q. Altogether, it is unknown if DDT can be appropriately applied to graphene NEMS.

In this work, we show that the Q in graphene NEMS devices can be understood with a wrinkle-corrected theory of dissipation dilution by measuring strain, modulus, bending stiffness, device dimensions, and Q on all measurable vibrational modes and on a large number of graphene NEMS. From this data, we identify that an anomalously

large bending stiffness caused by out-of-plane wrinkles is likely responsible for the low Q typically observed in graphene NEMS. Using the elastic engineering principles laid out by dissipation dilution, we increase the strain and suppress corrugations through Ga^+ ion irradiation and achieve record Q in room-temperature graphene NEMS.

6.2 Results

To test DDT for graphene NEMS, we first outline the predictions for a circular membrane. Dissipation dilution refers to the fundamental observation that thin, highly strained NEMS (*e.g.* strings and membranes) primarily store and lose energy through elongation and bending, respectively, so the Q of these mechanical structures can be increased by maximizing the ratio of the elongational energy to the bending losses. According to DDT (see Section 2.3), the Q of a circular membrane is,

$$Q_{!"} \approx \frac{Q_{\$}}{\lambda}(1 + \lambda \times \alpha_{!"})^{-8} \tag{6.1}$$

where α_{CB} is a constant that depends on the mode number ($\alpha_{\$8} = 2.404$, $\alpha_{88} = 3.832$, *etc.*) and $Q_{\$}$ is the intrinsic quality factor that arises from internal damping mechanisms(36). The increasing nature of the α_{CB} coefficients captures the higher bending losses that accompany the additional curvature of higher order modes. In Eq. 1, $\lambda = ?\frac{\overline{\hat{}}}{aI}$ is called the dilution factor, where a is the membrane radius and T is the tension. For a 3D plate of thickness h, the bending stiffness(44) is,

$$\kappa_{6bIR3} = \frac{Eh^{:}}{12(1-\nu^{+})} \tag{6.2}$$

where ν is the Poisson's ratio. For a bilayer graphene membrane, Eq. 6.2 predicts $\kappa \sim 160$ eV. Although $Q_{\$}$ is typically constant for a given material, it has been found to scale as $Q_{\$} \propto \frac{8}{c}$ for sufficiently thin NEMS(40, 124) (below ~100 nm), presumably due to surface losses.

To test the predictions of dissipation dilution, we fabricate a large array of CVD graphene drumhead resonators(74) (see Figure 6.1a) with diameters ranging from 4.4 μm to 16 μm. We primarily use commercially transferred bilayer graphene

(Graphenea) due to an improved yield of large-area drumheads. These devices are electrostatically actuated with an AC-gate voltage (V_{dc}) with a DC offset (V_{dc}) and the motion is measured with a 633 nm HeNe laser using scanning optical interferometry(79), which can resolve the mode shape of the various mechanical modes. All measurements were performed at room temperature under a vacuum of $P < 10^{-6}$ Torr. The laser power is kept low (typically less than 30 μW) to minimize the effects of photothermal heating and laser induced back-action(48), which can artificially modify the Q. Resonance frequencies and Q are obtained by fitting the characteristic amplitude frequency response curves around $V_{dc} = 0$ V, where Joule losses(130) are minimized.

In order to test the dependence of Q on the quantity Ta^{+}, we measure the device radii a from high resolution scanning electron images (Figure 6.1b) and the stress from the characteristic frequency-gate voltage dispersion curve, $f_0(V_{dc})$ (Figure 6.1c). We use a continuum mechanics model(29, 48, 62, 81) to fit $f_0(V_{dc})$ and obtain the tension T, mass per unit area ρ, and in-plane elastic modulus Y (see Supplementary Figure B.1). The parameter uncertainty for smaller diameter devices was large, so in this case we obtained T from the measured device resonance frequency f_0, ρ from larger devices, and the relation for the resonance frequency of a circular membrane(66) $f_0 = \frac{2.405}{2\pi a}\sqrt{\frac{T}{\rho}}$. We also check the self-consistency of T measured from fitting and f_0 (see Supplementary Figure B.1). Values of ρ range between $9 - 11\rho_g$ (where ρ_g is the intrinsic mass density of monolayer graphene), which is consistent with bilayer graphene with typical amounts of mass contamination. Values of T vary between 10 and 100 mN m^{-1}. We find that the devices have a modulus of Y_{2D}~80 N m^{-1}, which is consistent with previous work(62, 131) but much lower than the predicted by the bulk modulus of bilayer graphene, hE_{3D}~670 N m^{-1} (see Supplementary Figure B.1) assuming $h = 0.67$ nm for bilayer graphene.

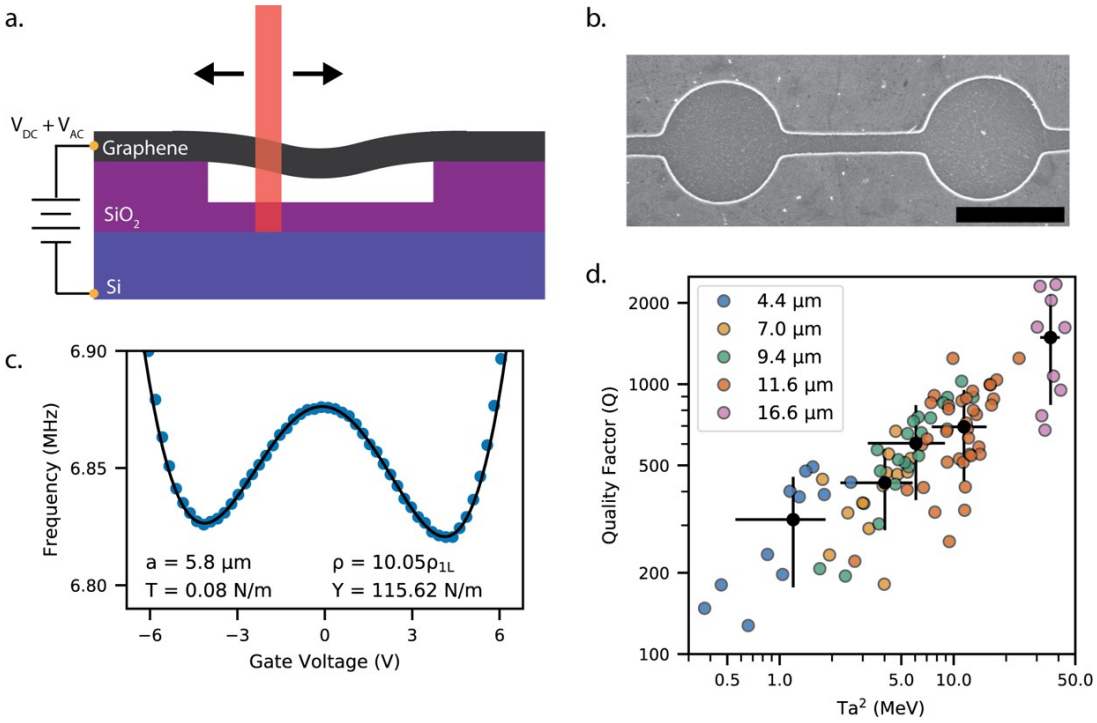

Figure 6.1: Characterization of graphene drumhead dataset. (a) Diagram of a graphene NEMS device. (b) Scanning electron microscope image of two 11.6 μm suspended graphene drumheads. (scale = 10 μm). (c) Resonance frequency of a 11.6 μm bilayer graphene drumhead as the gate voltage is swept from −6 V to 6 V. The black line is the fit to the data which gives mechanical parameters of $T = .08$ N/m,$\rho = 10.05\ \rho_{-=}$, and $Y = 115.62$ N m^{-1}. (d) Quality factors for the five different diameters. (d) Q vs. elongational energy parameter for drumheads of various diameters. The average measured mass density of 9.65 $\rho_{:}$ for 11.6 μm drumheads was used along with $f_{,}$ to estimate T to within ~10% for all devices.

Broadly, the quality factors of our graphene NEMS devices display a size-and-stress trend indicative of dissipation dilution. First, we observe a size-dependent quality factor, ranging from Q~400 for 4.4 μm diameter drumheads to Q~1600 for the largest 16.6 μm diameter devices, in accord with previous work on graphene membranes(65, 66) (see see Supplementary Figure B.1). Next, we analyze the unified contributions of size and strain together. Figure 6.1d shows the fundamental drumhead mode quality factor plotted against the elastic energy parameter, Ta^{+}. Despite the significant stress variability within a given diameter, we observe a clear

agreement with the theoretical scaling of $Q \approx Q_{\$}$ $?\frac{\overline{aI}}{\backslash}$ when $\lambda \ll 1$. Our data agrees with this DDT scaling over two orders of magnitude in the quantity Ta^{+}, in contrast to previous tests size dependence alone(66), which only spanned a factor of five in membrane radius. The size and stress dependence of the Q provides evidence that these previous results regarding the strain and size-dependent Q in 2D NEMS arise from dissipation dilution, rather than a frequency or area dependent damping mechanisms(36, 132), since higher frequencies due to strain lead to a higher Q while those due to a smaller size lead to a smaller Q.

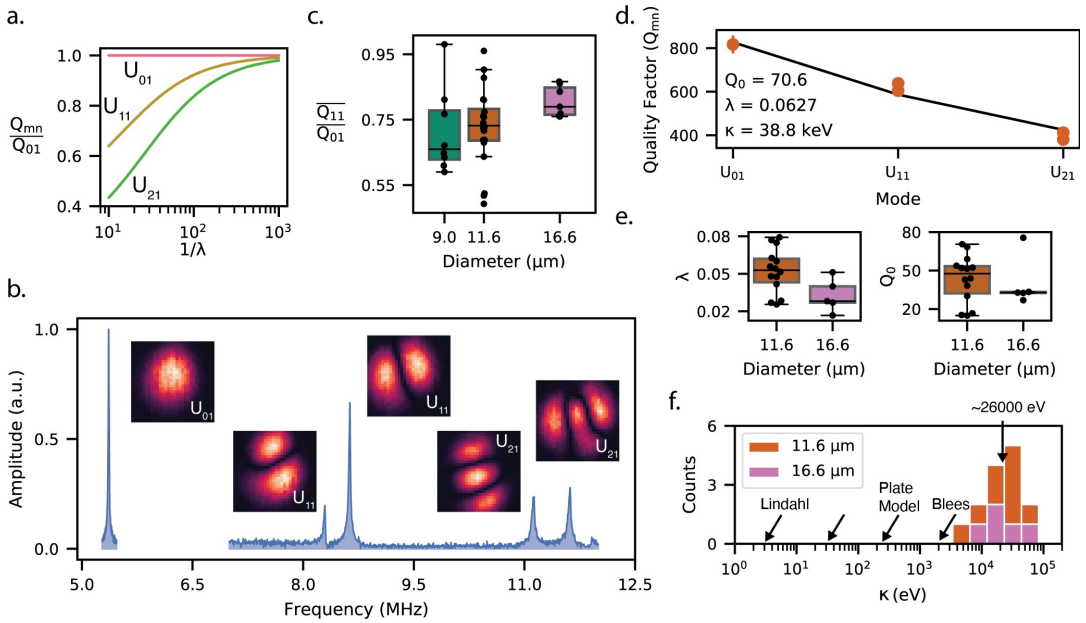

Figure 6.2: Modal dependence of the quality factor. (a) Predicted $Q_{>?}$ relative to the intrinsic quality factor $Q_{,-}$ versus the dilution factor λ. (b). Amplitude-frequency response spectra and corresponding mode shapes for the first 5 modes of an 11.6 μm device. (c) $\frac{\overline{Q_{11}}}{Q_{01}}$ for several different diameter drumheads. We average the Q of the degenerate U_{--} mode to obtain $\overline{Q_{--}}$. (d) Q as a function of mode number for an 11.6 μm diameter device. Fitting yields $Q_{,} = 70.6, \lambda = 0.0627, \kappa = 38.8$ keV. (e) $Q_{,}$ and λ derived from the fit shown in d for a number of 11.6 μm diameter drumheads. (f) Logarithmic histogram of measured κ values for 11.6 μm and 16.6 μm diameter drumheads.

A hallmark of dissipation dilution is the mode-dependence(39, 44, 65) of Q, which, according to Eq. 6.1, can be cast into a $Q_{\$}$-independent ratio of the Q of any mode to the fundamental:

$$\frac{Q_{\mathrm{CB}}}{Q_{\$8}} = \frac{(1 + \lambda \times (\alpha_{\$8})^{+})}{(1 + \lambda \times (\alpha_{\mathrm{CB}})^{+})} \qquad (6.3)$$

Q is expected to decrease due to the increased curvature (*e.g.* $\nabla^{+}U_{\mathrm{CB}}$) of the antinodes in the higher order modes(65). However, as λ decreases, the curvature at the clamped edge (to satisfy the boundary condition $\nabla U_{\mathrm{CB}}(r = a) = 0$) becomes the dominant curvature term, making the quality factor across modes increasingly uniform (Figure 6.2a). To test this trend in graphene NEMS, we first measure the amplitude spectrum (Figure 6.2b) and then identify the first several modes using scanning optical interferometry(79), as seen in Figure 6.2b inset. With the modes identified, we calculate $\overline{Q_{88}}/Q_{8\$}$, where $\overline{Q_{88}}$ is the average Q of the degenerate pair of U_{88} modes, for 9 μm, 11.6 μm, and 16.6 μm diameter drumheads (Figure 6.2c). We do not look at $Q_{+8}/Q_{8\$}$ because it is difficult to unambiguously identify the higher frequency U_{+8} mode in the 9 μm devices. From this, we see that $\overline{Q_{88}}/Q_{8\$}$ increases with diameter, from a median value of 0.66 for 9 μm diameter drumheads to 0.79 for 16.6 μm drumheads, which corresponds to values of λ of 0.087 and 0.036, respectively. Similar results have been seen in SiN strings and membranes(65), however, these values of λ are significantly larger than in a typical SiN membrane(44), where $\lambda \sim 10^{-=} - 10^{-:}$ and the Q does not begin to decrease until much higher mode numbers.

A more accurate measurement of λ and $Q_{\$}$ can be obtained by fitting the Q vs. mode number to Eq. 6.1 for the first 5 drumhead modes, which we do for a smaller sub-set of the 11.6 μm diameter drumheads. An example of this fit for the same device as shown in Figure 6.2b. The range of measured values for λ and $Q_{\$}$ is shown in the box-and-whisker plots in Figure 6.2e. We find a median value of $\lambda \sim .053$, consistent to the λ obtained by taking the ratio $\overline{Q_{88}}/Q_{8\$}$. We also measure $Q_{\$}$ between 10 and 80 with a median value of $Q_{\$} = 47.6$. This is in line with an extrapolation of the thickness-dependent quality factor seen in SiN strings(39, 124), where $Q_{\$} \sim 6900\ \frac{\mathrm{c}}{8\$\$\ \mathrm{BC}}$. This

intrinsic loss is thought to arise from surface losses that are ubiquitous in thin NEMS(124) and is likely similar across various materials. Taking the bilayer graphene thickness to be . 67 nm, we expect $Q_{\$}$~47, in excellent agreement with our measurements.

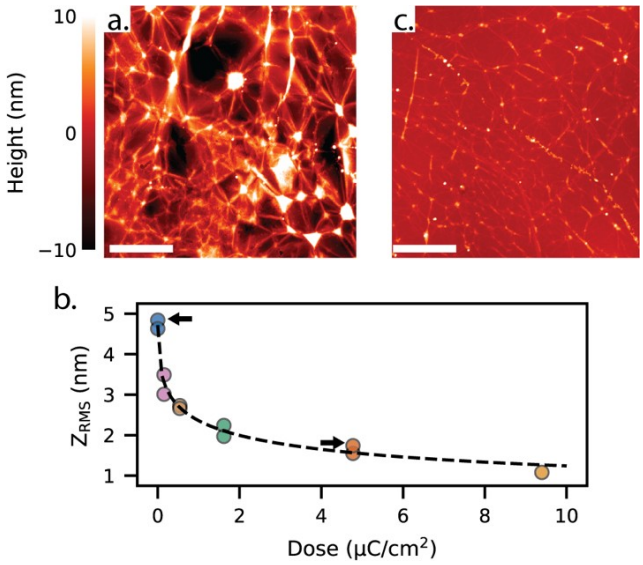

Figure 6.3: AFM images and RMS roughness of 11.6 μm diameter FIB irradiated drumheads. (a) AFM image of a non-irradiated bilayer graphene drumhead. (scale = 1 μm). (b) RMS roughness values at various irradiation doses. Each data point represents the RMS roughness value from 16 μm² section of a separate drumhead. The black arrows indicate values corresponding to the scans shown in a and c. (c) AFM image of a bilayer graphene drumhead irradiated at 4.8 μC/cm². (scale = 1 μm).

We separately fit the first 5 drumhead modes to obtain κ using the measured value of T and a. We find κ falls between ~5 − 75 keV with a median value of κ_8~26,000 eV (see Figure 6.2e). This value is significantly larger than theoretical predictions with the 3D plate model (Eq. 6.2) predicting $\kappa_{\text{jnimG}} \approx 160$ eV and the phonon spectrum of graphite(129) predicting $\kappa \approx 3$ eV. A similarly large value of κ~$10^{\text{:}} - 10^{\text{=}}$ has been observed in CVD graphene cantilevers(126) using non-contact methods. Given the measured values of T and $Q_{\$}$, an abnormally large value of κ appears to be responsible for the low Q observed in graphene NEMS. Given that $Q_{\$}$ is roughly in-

line with that expected for an atomically thin-NEMS with surface losses, reducing κ is imperative for increasing the Q in graphene NEMS.

Large-scale wrinkles and corrugations(126, 133) present in suspended 2D sheets can explain the anomalously high values of κ that contribute to lower quality factors. Out-of-plane wrinkles and corrugations will modify the elastic properties (κ and Y) of bare two-dimensional (2D) sheets(127), like graphene. In particular,

$$\kappa_{GHH} = \beta_{\backprime} \times \mathrm{O}\overline{\kappa_{1B_{\mathbb{m}}} Y_{1B_{\mathbb{m}}} \langle z_{GHH}{}^{+} \rangle} \tag{6.4}$$

$$Y_{GHH} = \beta_{o} \times \acute{\mathbf{O}} \overline{\frac{Y_{1B_{\mathbb{m}}} \kappa_{1B_{\mathbb{m}}}}{\langle z_{GHH}{}^{+} \rangle}} \tag{6.5}$$

where $\kappa_{1B_{\mathbb{m}}}$ and $Y_{1B_{\mathbb{m}}} = E_{1B_{\mathbb{m}}} h$ are the intrinsic bending stiffness and in-plane modulus, respectively, and $z_{\_pq} = \mathbf{?}\overline{\langle z_{GH}^{+} \rangle}$ is the RMS height profile of the wrinkled membrane.

$\beta_{\backprime}$ *and* β_{o} in Eq. 6.4 and Eq. 6.5 are small corrections(127) to the expected to be of order 1. We directly measure the $z_{\_pq}$ using atomic force microscopy (AFM) and find an $z_{\_pq}$~4.72 nm for the bilayer graphene membranes (Figure 6.3a). Unlike in other work, we use extremely low indentation forces of 1 nN to not flatten the surface during AFM imaging(134, 135). Using the known values of $E_{1B_{\mathbb{m}}} = 1$ TPa, $h = .667$ nm, and the bulk value of $\kappa_{8,1B_{\mathbb{m}}} \approx 160$ eV, Eq. 3 and Eq. 4 predict κ_{GHH} ~5 keV and Y_{GHH} ~25 N m^{-1}. These values differ significantly from theoretical bulk values and are much closer to the values we measure in this work ($\kappa_8 \approx 26{,}000$ eV and $E_{+\%} \approx 90$ N m^{-1}), suggesting that wrinkles play a major role in determining the mechanical properties of graphene NEMS and must be taken into account when describing the Q with dissipation dilution.

The presence of wrinkles will increase the bending stiffness, thereby decreasing Q as predicted by DDT. By removing these wrinkles, it should be possible to achieve higher quality factors in graphene NEMS, with a predicted scaling of $Q \propto \frac{8}{\mathrm{r}_{2'A}}$. To test this effect, we use 30 kV Ga^{+} FIB irradiation to flatten a set of 11.6 μm diameter drumheads(128). We find $z_{\_pq}$ decreases monotonically with FIB dose (Figure 6.3b),

reaching a value of z_{pq}~1 nm at 9.4 μC/μm². The reduction in wrinkles is visible in AFM images from a non-irradiated drum (Figure 6.3a) and one irradiated at 4.77 μC/cm² (Figure 6.3c). To infer z_{pq} with various FIB doses, we fit $z_{pq}(D)$ to a heuristic function,

$$z_{pq}(D) = \frac{z_{pq}(0)}{(1 - D^{s})} \tag{6.6}$$

where D is the dose in μC/cm² and find $z_{pq}(0) = 4.72$ nm and $\gamma = .45$ (black dashed line in Figure 6.3c). We do not determine the ultimate limit of how small z_{pq} can be made with FIB irradiation; however, perfectly flat 2D materials are expected to be thermodynamically unstable(136) so it is likely impossible to reach a perfectly flat state and recover the intrinsic bending stiffness. We attribute the reduced wrinkling to a reduction of the device area due to FIB-induced knock-out damage(131).

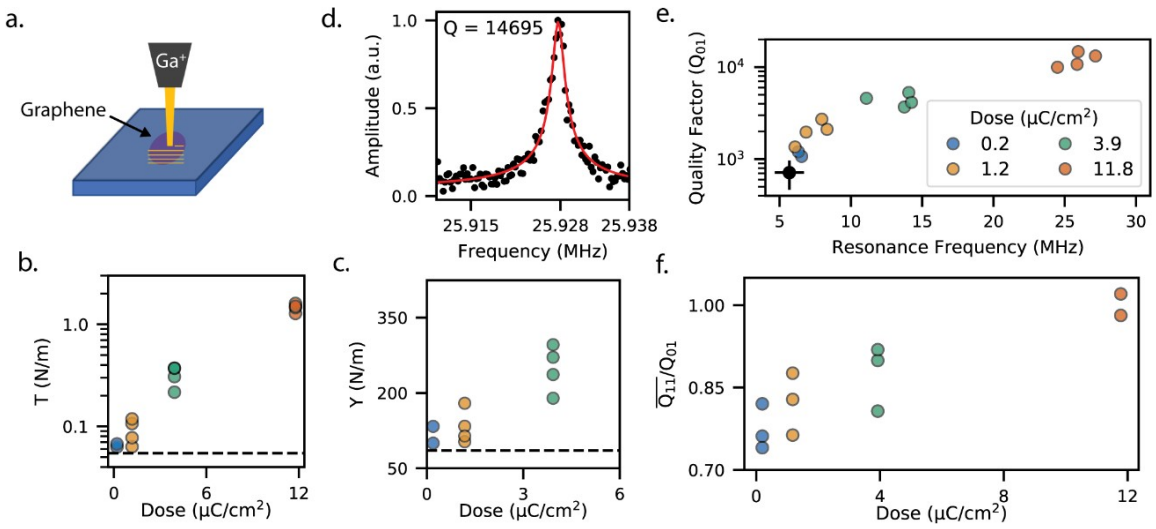

Figure 6.4: Effect of FIB irradiation on the mechanical properties of 11.6 μm diameter drumheads. (a) Diagram of the FIB irradiation process. (b) T vs. dose. For the 11.8 μC/cm², we estimate T from the resonace frequency rather than fitting $f_n(V_{89})$. (c) Y vs. dose. The black line in b-c indicates the average value for non-irradiated drumheads of the same diameter. (d) Amplitude-frequency response curve used to extract the highest quality factor, where $Q = 15{,}000$. (e) Q vs. f_n for the 4 different doses. The black error bars shows the mean and standard deviation of the non-irradiated 11.6 μm devices. (f) $\overline{Q_{11}}/Q_{01}$ vs. FIB dose with the black line again indicating the value for non-irradiated 11.6 μm diameter drumheads.

In addition to the reduced wrinkling, we also measure significantly modified elastic properties for the FIB irradiated devices. In separate set of FIB irradiation experiments on 11.6 μm drumheads with a dose ranging from $0.2 - 11.8$ μC/μm^2, we also find that the tension increases super-linearly, from ~.05 N/m to 1.5 N/m (Figure 6.4a), leading to resonance frequencies of $20 - 30$ MHz, $5 - 6$ higher than the non-irradiated drumheads. We also find that that Y increases by about a factor of ~3 (Figure 6.4b) from ~90 N/m to ~250 N m^{-1} at a dose of 3.9 μC/μm^2, consistent with a reduction in wrinkles. We cannot accurately measure Y for the highest dose devices but we expect it to be closer to the theoretical value for bilayer graphene of 670 N/m. A large increase in the elastic modulus through defect creation have been observed in previous work(135), however, this was not associated with a higher strain. This difference might arise from a different defect type due to the irradiation method (5 kV Ar^+ vs. 30 kV Ga^+) or different measurement methods (Raman vs. resonance frequency). In other studies however, defects have been associated with higher tension(137), necessitating further evaluation of the effect of irradiation on the mechanical properties of graphene membranes.

We see a dramatic increase in the quality factor for the irradiated drumheads. $Q_{\$8}$ increases by a factor of $\sim 15 - 20$, from Q~700 for non-irradiated drumheads to nearly Q~15,000 at 11.8 μC/μm^2 (Figure 6.4d-e),. We plot the frequency response for our highest-Q device in Figure 6.4d, which we fit to have $Q = 14695$, which is the highest reported quality factor in graphene NEMS at room-temperature to date. This large increase in the Q is consistent with DDT given reduced wrinkling and larger tension. Although we are unable to directly measure κ due to the higher frequencies (and thus fewer measurable modes) of the irradiated devices, combining Eq. 6.4and Eq. 6.6 gives the expected bending stiffness as a function of the FIB dose,

$$\kappa(D) = \frac{\kappa(0)}{(1 - D^t)} \tag{6.7}$$

where, $\kappa(0)$~26000 eV is the bending stiffness with no FIB irradiation. For 11.8 μC/μm^2, we expect $\kappa_8(D)$~7000 eV, giving a value of λ~ .005 with the measured

tension of 1.5 N/m. With this and $Q_{\$}$~47, Eq. 6.1 predicts Q~9700, which is close to our measured values, especially considering the variability in the measured values of $Q_{\$}$ and $\kappa(0)$. We also find that the ratio $Q_{\$8}/Q_{\$8}$ increases with the FIB dose (Figure 6.4f), reaching near unity of the highest dose, consistent with a larger value of λ.

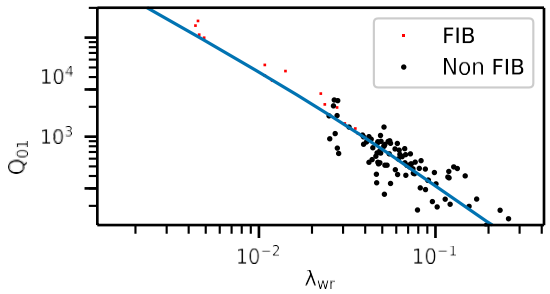

Figure 6.5: All measured FIB and non-FIB devices with a wrinkle-corrected dilution factor. The blue line is Eq. 6.1 with $Q_{,} = 47.3$.

Our combined measurements of non-irradiated graphene drumheads of various diameters and irradiated drumheads is consistent with dissipation dilution with a wrinkle corrected value of κ_8 that is orders of magnitude higher than expected for bare graphene drumheads.

The wrinkle-corrected dilution factor is,

$$\lambda_{uh} = \frac{?}{\beta_v(\kappa_{lBm}Y_{lBm})\text{-}?} \frac{\overline{B}}{\underline{w_{CDE}}} \quad (6.8)$$

Although the exact value of the proportionality constant likely depends on the nature of the exact nature of the wrinkles, it can be determined from Eq. 6.4. With κ_{GHH}~26000 eV, $\kappa_{lBm} = 160$ eV, and Y_{lBm}~670 N/m, we find a scaling constant of $\beta_v = 6.73$. We plot Q vs. the calculated λ_{uh} with a dose dependent $z_{hCy}(D)$ for all devices in Figure 6.5 and find excellent agreement with Eq. 6.8 across nearly three orders of magnitude using the measured value of $Q_{\$} = 47.3$.

6.3 Discussion

Overall, our results indicate that the origin of the low Q in graphene NEMS seems to originate from similar microscopic loss mechanisms as other 2D NEMS, however, the wrinkled nature of the sheets enhances the bending losses and lowers the Q. These

results could also help explain the temperature-dependence of the Q in cryogenically cooled graphene NEMS(54, 62, 81). As graphene is cooled, both tension and the measured in-plane modulus are observed to increase(62) simultaneous to a large increase in the Q, which can reach values of $10^{=}$ at 4 K(54, 81), an improvement of 10^{+}. This is in contrast to SiN where the Q only increases by a factor of ~10 even when cooled to 10 mK(40). Taken in the context of this work, the cooling increases tension and reduces wrinkles, which increases Y_{GHH} and reduces κ_{GHH}, thus leading to higher quality factors. Additionally, cooling will likely decrease $Q_{\$}$ by a similar value as in SiN(138), assuming the underlying damping mechanism is the same

It is likely that more aggressive shape and strain engineering approaches would lead to even more impressive quality factors than FIB irradiation alone. For example, patterning a phononic shield(34, 40) around the graphene NEMS would suppress the dominant edge bending, leading to a modified expression for the quality factor(34), $Q_{CB} \sim Q_{\$}/(\lambda^{+}\alpha_{CB})$. Using the estimated values for the bending stiffness and tension for the Ga^{+} irradiated graphene drums, this expression predicts a $Q > 10^{-}$ and $f \times Q = 10^{8:}$, potentially allowing for room-temperature quantum optomechanics with atomically-thin materials(35) or photothermal cooling(48) of a graphene sheet from room temperature to the quantum ground state. Furthermore, our devices operate well below the experimentally measured tensile strength of 50 N/m in monolayer graphene graphene(139) and are significantly smaller than the largest diameter membranes fabricated(66). By fabricating large area membranes near the tensile limit, quality factors of $Q > 10^{<}$ could be readily achieved, matching or exceeding the Q in SiN NEMS(34). Furthermore, these findings can be readily applied to other resonators made from exfoliated graphene(20) or other 2D materials(140) such as MoS_2, which share similar aspect ratios and mechanical parameters, but possess other desirable optical and electronic properties.

6.4 Conclusion

In conclusion, we have shown that a general theory of dissipation dilution broadly describes the observed quality factors in terms, of stress, size, and mode number. By

fitting the quality factors of higher order drumhead modes and comparing the stress, we determined a value for the bending stiffness in tension graphene drumheads. This bending stiffness was found to be three orders of magnitude larger than predicted from a 3D plate model, but can be explained by corrugations, and is likely responsible for the observed low Q in graphene NEMS. Guided by this knowledge, we report record Q for room temperature graphene NEMS. This high Q and ultra-low mass resonator could open the door to extremely-sensitive force and mass sensing or studies of quantum optomechanics(42, 48) in the two-dimensional regime.

6.5 Bridge

In this chapter, we presented strong evidence that the Q in graphene NEMS is governed by dissipation dilution. By adding stress and reducing static wrinkling, we can increase the Q by a factor of 20, reaching values as high as $Q\sim15000$. This work lays out the groundwork for achieving high-Q in graphene NEMS, one of the two key requisites for arrays of NEMS. In the next section, we will begin tackling the second challenge use of large-scale NEMS arrays, namely efficient actuation and control methods.

CHAPTER VII

SPATIALLY RESOLVED OPTICAL EXCITATION OF MECHANICAL MODES IN GRAPHENE NEMS

From Miller, D. & Alemán, B. Spatially resolved optical excitation of mechanical modes in graphene NEMS. *Appl. Phys. Lett.* **115**, 193102 (2019). I performed the fabrication, experimental measurements, data analysis, and am the primary author on the publication. Benjamín Alemán is my supervisor.

7.1 Introduction

Nanoelectromechanical systems (NEMS) made from two-dimensional materials, such as graphene(20), h-BN(141), and the transition metal dichalcogenides(142) have high promise for nanomechanical force and mass sensing(67, 81, 82) as well as studies of fundamental physics at the nanoscale(57). Initial experiments with 2D nanomechanical resonators have primarily focused on the dynamics of the fundamental mode(54, 66, 80, 81), but advanced NEMS applications are increasingly exploiting higher order-mechanical modes(27, 32) and the coupling between these modes(29). For example, by simultaneously tracking several mechanical modes, NEMS resonant detectors can both weigh and localize single molecules or individual viruses(143), while fine control over multiple modes has been used for all-mechanical phonon side-band cooling(29).

Future advances in NEMS multimodal applications demand that the shape of the mechanical modes be precisely known and, simultaneously, that any mode of interest can be efficiently and selectively actuated. Several high-resolution imaging methods, including scanning optical interferometery(79) and atomic force microscopy(89), have already been used to map the mechanical mode shape of 2D NEMS. The fundamental mode and some higher-order modes of 2D NEMS are routinely accessed, but the efficient, selective actuation of a given mode remains a challenge. For instance, a common means to actuate 2D NEMS is with an electrostatic gate(20, 54, 57, 79–82), but simple gating techniques are inherently inefficient at driving higher-order,

antisymmetric modes(29) because the gate applies a symmetric, constant-phase force density across the entire suspended membrane. Furthermore, electrostatic gating cannot be used to actuate insulating materials(141) or freestanding 2D drums(85, 120, 144) and gating reduces quality factors(121) due to Joule heating.

The combination of scanning optical interferometry and optical drive methods(77, 78) offers an approach to simultaneously image and actuate a 2D NEMS resonator, but only if the optical probe and drive force are sufficiently spatially localized. Optical drive methods have been used to selectively actuate higher-order modes in bulk micromechanical beams because the resulting radiation pressure and photothermal bending forces are localized to the immediate vicinity of the laser spot(145). Optical driving has also been employed to actuate 2D NEMS with both defocused and focused lasers(20, 47, 66, 120, 137, 141, 142, 146). The defocused drive laser, like gating, exerts a symmetric force and is therefore inefficient at driving higher-order modes. With focused lasers, the ultralow intrinsic heat capacity (mass) and exceptionally high thermal conductivity(47) of 2D materials coupled with the small lateral dimensions ($\sim 2-5$ μm) of the NEMS structures causes them to thermalize rapidly, which could make thermomechanical bending less local. Furthermore, the low optical absorption and reflectivity of 2D materials significantly decreases photon pressure, which is a local effect when using a focused laser. To date, experiments with focused lasers have either used static lasers—which can only measure mechanical spectra—or co-localized probe and drive lasers(20, 66), which convolve spatially resolved motion with actuation and therefore prevent an assessment of the spatial resolution. Therefore, it is uncertain if optical driving is sufficiently local in 2D NEMS to enable selective mode actuation.

7.2 Results

To determine the spatial localization of the optical force of a focused laser on a 2D NEMS, we measure the vibrational amplitude of a suspended graphene membrane, which is proportional to the driving force, while we scan the position of a focused, driving laser across the membrane. By comparing the resulting force images to the

mechanical mode shapes obtained via scanning optical interferometry, we find that the resolution of optical drive force is comparable to the spot size of the laser, and this resolution is sufficient to efficiently and selectively actuate higher-order modes of the graphene membrane.

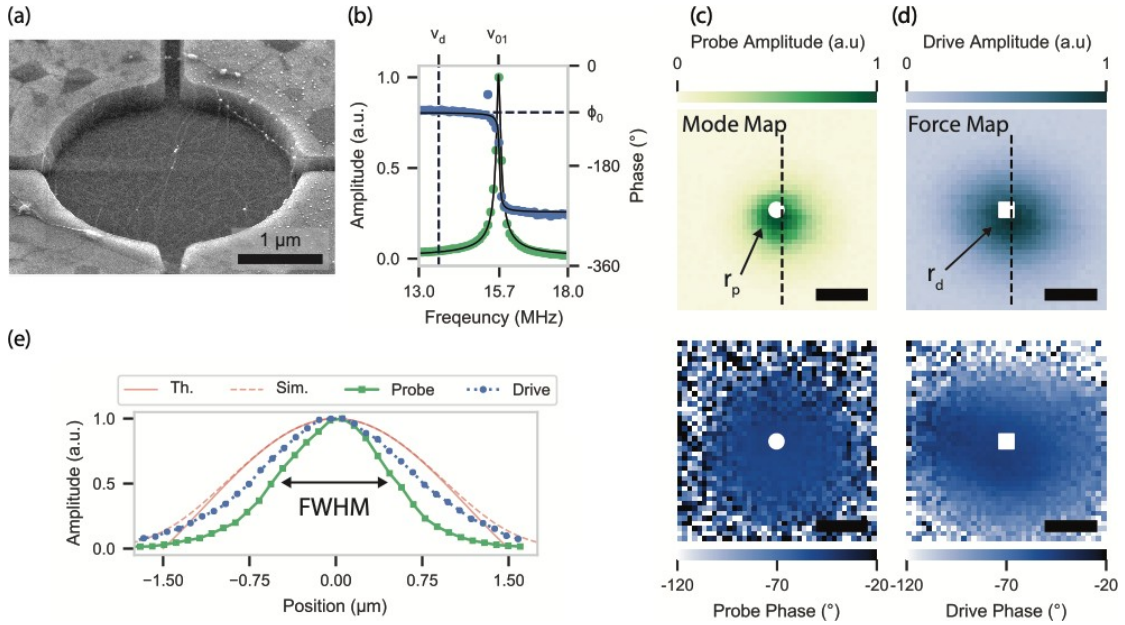

Figure 7.1: Optically driving the fundamental mode. (a) SEM image of a 3 μm graphene drumhead suspended over a 300 nm cavity. (b) Fitted (black lines) amplitude and phase response of the fundamental mode for a graphene drum. The device is driven at a frequency, ν_F, located below the resonance frequency, during acquisition of the spatial maps. The phase offset, $\phi_{,} = -84°$, of the mechanical oscillation is indicated by the horizontal dashed black line. (c) Amplitude and phase response maps obtained by scanning the probe laser while holding the drive laser at a fixed location, indicated by the white square in 1e. (d) Amplitude and phase response obtained by scanning the drive laser while holding the probe laser at a constant position, indicated by the white circle in 1d. (Scale = 1 micron). (e) Measured amplitude across vertical cross-sectional cuts in 1c-d. The theoretical mode shape and the expected measured mode shape after accounting for the Gaussian laser spot, for a 3 μm diameter drumhead, are indicated by the red solid and dashed lines, respectively.

The graphene NEMS devices studied in this work are few μm diameter nanomechanical drumheads (a 3 μm device is pictured in Figure 7.1a). We fabricate the drumheads by suspending single-layer graphene over cavities etched into SiO_2 on Si using a semi-dry transfer process(74). The devices are actuated using an amplitude modulated 445 nm laser(20, 47, 66, 137, 141, 142, 146), and the amplitude and phase are measured using an interferometer operating at 532 nm and standard lock-in

amplifier techniques, similar to previous work(29, 79). Both the 445 nm drive and 532 nm probe lasers are focused onto the sample using a 40 ×, 0.6 NA objective, yielding a spot-size of ~1 μm, and scanned using independent dual-axis galvo mirrors and coupled into the same optical path (see Supplementary Figure C.1). A schematic of our experimental setup is shown in Figure 3.10. In the following, we present results for a 3 μm diameter device, however, we observe similar, reproducible results for other devices and across a range of drumhead sizes.

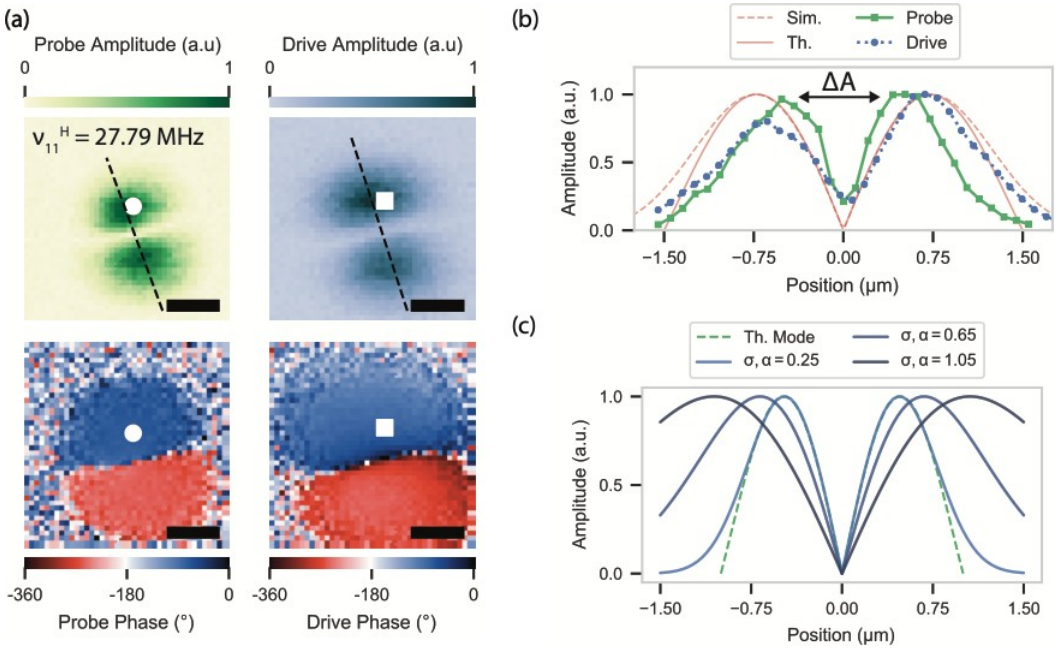

Figure 7.2: Optically driving the higher order modes. (a) Amplitude and phase recovered while scanning the probe (left) and drive (right) across the horizontally polarized U_{--}^{G} mode with ν_F set at 27.68 MHz (scale = 1 micron). (b) Cross-sectional profile of the amplitude for the mode and force maps (dashed line in 1a). The theoretical mode shape and predicted measured mode shape are indicated by the solid and dashed lines, respectively. (c) Simulated drive force versus r_F obtained by integrating the measured U_{--} mode (green dashed line) with the force density model for several values of σ and α.

We create two types of spatial maps of the membrane: mode maps and force maps (see Section 3.5). To obtain these maps, we first measure the frequency response spectrum of the graphene drumheads to find the mechanical resonance of the mode of interest (Figure 7.1b). Then, we set the driving frequency $\nu_>$ below the mode

resonance frequency $\nu_{!"}$, but above the flat amplitude response that occurs at low frequencies. Here, the relative change in amplitude and phase with respect to $\nu_{!"}$, which can drift due to heating(79), are small but individual modes can still be resolved above the background. To obtain the mode map, which measures the membrane's vibrational amplitude at different locations, we fix the position of the drive laser, $\boldsymbol{r_d} = (x_>, y_>)$ and scan the probe laser over an area slightly larger than the drumhead, while simultaneously measuring both the amplitude and phase of resonant motion at each point of a 40×40 array, resulting in a 1600 pixel map of the mechanical mode (Figure 7.1c). To obtain the force map, we fix the probe laser position, $\boldsymbol{r_p} = (x_6, y_6)$, on an antinode and measure the membrane amplitude and phase response for a given mode $U_{!"}$, as we scan the position $\boldsymbol{r_d}$ over the membrane. The measured amplitude $|a_{!"}(\boldsymbol{r_d})|$ is directly proportional to the drive force $|F_{!"}(\boldsymbol{r_d})|$. This off-resonant, fixed frequency approach allows scan times of $\sim$1 minute, $10 - 100$ times faster than obtaining the frequency response spectra at each point, and can resolve a spatially varying phase, unlike using a phase-locked loop.

The mode and force maps for the fundamental mode of the device ($U_{\$8}$) are shown in Figure 7.1c and Figure 7.1d, respectively. The graphene drumhead used to obtain this data has a resonance frequency of 15.7 MHz and a quality factor of $Q\sim120$. We plot cross-sections of the amplitude mode and force maps, indicated by the black dashed lines in Figure 7.1c-d, in Figure 7.1e, along with the theoretically predicted mode shape. The mode map exhibits a relatively constant phase (Figure 7.1c, bottom) and generally matches the expected shape for a circular membrane, including the full width. However, the full-width at half-maximum ($FWHM_{6DX23}$) of the measured mode shape is $\sim$58% that expected for a 3 μm diameter drumhead, potentially to imperfections in the atomically-thin membrane(79). The force amplitude map resembles the measured mode shape but is dilated at $FWHM$ by a factor $W_{\$8} \approx 1.4$, where $W_{\$8} = FWHM_{>D1V3}/FWHM_{6DX23}$ (Figure 7.1d). In contrast to the mode phase map, the phase lag is minimized at $\phi_{\$}\sim -45°$ near the center of the drum and increases to $\phi_{\$}\sim -100°$ towards the edge of the drum. We characterize the rate of this phase lag across the cross-section using a parabolic fit, $\phi_{\$}(x_>) = \phi_{\$}(0) + \delta_{\$8}{x_>}^{+}$,

and find $\delta_{\$8} = -17°/\mu m$ (Supplementary Figure C.3). We verify that the difference in phase is due to a spatially-varying phase, rather than a change in the resonance frequency, by obtaining full frequency-response spectra at various locations on the membrane and fitting for $\phi_{\$}$ (shown in Supplementary Figure C.2 for a different 3 μm device). Our measurements of the fundamental mode verify that both the drumhead amplitude and phase depend on the position of the focused drive laser.

To further characterize the optical drive force, we examine the horizontal polarization of the antisymmetric degenerate U_{88} mode, which we label $U_{88\{}$. The mode map (Figure 7.2a-b) shows a characteristic antisymmetric shape with two lobes separated by a nodal line(66, 79), where one lobe oscillates ~180° out of phase with the other. The amplitude nearly vanishes on the nodal line and the phase changes discontinuously. As with the $U_{\$8}$ mode, we observe that the size of the mode shape, ΔA, defined as the distance between the pair of antinodes, is ~72% of the expected value. Positioning the probe laser on an antinode, we again find the force map is qualitatively similar to the mechanical mode map; it has two lobes separated by a nodal line with a location and orientation nearly identical to the mode map. Although the phase changes by a ~180° across the nodal line in both the mode and force maps, the position-dependence of the phase is quite different for each case. While the mode phase changes abruptly by 180°, as expected for oscillations that are perfectly out of phase, the force map phase changes continuously at a rate of ~0.3°/nm across the nodal line (see Supplementary Figure C.3). Similarly to $U_{\$8}$ the force map for the U_{88} mode is dilated compared to the mode maps, with $W_{88} = \Delta A_{>\mathrm{D1V3}}/\Delta A_{6\mathrm{DX23}} \approx 1.28$.

We observe similar results for the vertically polarized $U_{88|}$ mode, which has a resonance frequency of 32.23 MHz and is rotated ~90° from $U_{88|}$ (Supplementary Figure C.4).

We now discuss a model that can describe the behavior seen in the force maps and can characterize the spatial resolution of the drive force. The amplitude and phase of the force exerted on a mode $U_{!"}$ when the drive laser is positioned at $\boldsymbol{r_d}$ is,

$$|F_{!"}(\boldsymbol{r_d})|\exp i\phi_{!"}(\boldsymbol{r_d}) = \int dA\, U_{!"}(\boldsymbol{r})|f(\boldsymbol{r};\boldsymbol{r_d})|\exp i\beta(\boldsymbol{r};\boldsymbol{r_d}) \qquad (7.1)$$

where $U_{!\cdot\cdot}(\boldsymbol{r})$ is the normalized mechanical mode shape(77, 78, 145), $|f(\boldsymbol{r};\boldsymbol{r_d})|$ is amplitude of the optical force density, and $\beta(\boldsymbol{r};\boldsymbol{r_d})$ is the phase of the optical force density. We model $|f(\boldsymbol{r};\boldsymbol{r_d})|$ as a Gaussian distribution of the form $|f(\boldsymbol{r};\boldsymbol{r_d})| \propto \exp\left(-\frac{(x-x_H)^2+(y-y_H)^2}{2\sigma^2}\right)$, where $\sigma = FWHM/2.355$. A Gaussian force distribution matches the shape of the focused laser and will approximate any azimuthally symmetric force centered at the drive laser position, such as photothermal stress or photon pressure. Likewise, the phase lag of the force density $\beta(\boldsymbol{r};\boldsymbol{r_d})$ will be a minimum at $\boldsymbol{r_d}$, allowing us to expand $\beta(\boldsymbol{r};\boldsymbol{r_d}) \approx \beta_0 - \frac{\alpha}{2}((x-x_0)^2+(y-y_0)^2)$ around the laser spot, where α is a constant that characterizes the rate of phase lag. The overall locality of the optomechanical drive force is determined by the spatial extent of both the phase and amplitude of the optical force density.

To infer the localization of the optomechanical drive force, we numerically integrate the overlap integral in Eq. 7.1 using the approximate forms of $|f(\boldsymbol{r};\boldsymbol{r_d})|$ and $\beta(\boldsymbol{r};\boldsymbol{r_d})$ and the theoretical mode shapes for a circular membrane in two-dimensions. We vary the values of both α and σ and look for consistency in W_{08}, W_{88}, and δ_{08} between the simulated and experimentally measured amplitude cross-sections of $|F_{!\cdot\cdot}(\boldsymbol{r_d})|$. In these calculations, we take the diameter of the mode shape to be 2 μm, which corresponds to the average of the mode sizes of the experimentally measured U_{08} and U_{88} modes. Figure 7.2c shows the simulated cross sections of the force map for several values of σ and α. We find that values of σ and α between . 55 μm and . 75 μm best match our experimental measurements (see Supplementary Figure C.5), corresponding to a FWHM of 1.3 μm to 1.75 μm for $|f(\boldsymbol{r};\boldsymbol{r_d})|$. This simple model can also capture the spatially varying phase seen in Figure 7.1d and Figure 7.2a assuming a slight asymmetry in the mode-shape, such as the small difference in the amplitudes of the two antinodes seen in Figure 7.2b. We note that the force maps in some devices display complexity that is not readily captured by this model (see Supplementary Figure C.6 for an example), but may potentially be due to various defects in the drumhead such as adlayers or grain boundaries(146) which alter the phase response.

In the future, a more descriptive model will be important for experiments that precisely measure the oscillation phase(47).

Though the above procedure only yields an approximate value for the localization of the force density, the stark contrast between the measured force map and that predicted from a larger area force density (*i.e.* $\sigma > 1$ μm) strongly suggests that the drive force is localized to a small region centered around the laser spot. This is in accord with 1D simulations of the temperature profile arising from a modulated laser incident on a graphene drumhead(146). Reducing the laser spot size by using shorter wavelengths or higher NA objectives could further enhance the control of the optomechanical drive efficiency, especially for smaller drumheads or beams which tend to vibrate at high frequencies(147).

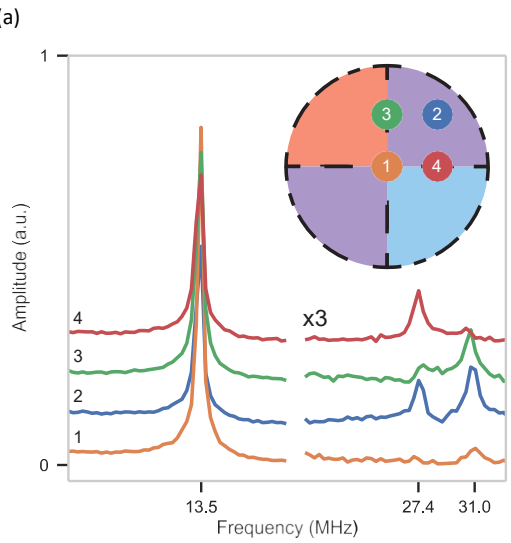

Figure 7.3: Frequency response traces with the drive laser at four different locations on the drumhead.

As further evidence of the local nature of the optical force in 2D NEMS, we demonstrate that a focused drive laser can selectively suppress or excite either polarization of the U_{88} mode. To show this, we position the probe laser at a location sensitive to the motion of $U_{\$8}$ and both polarizations of U_{88}, and then we measure the frequency response while the drive laser is positioned at four different locations on the membrane, all either on an antinode or node of the orthogonal U_{88}\{ and U_{88}|

modes (see Figure 7.3). The spectra show that the mode can be excited when the drive is placed on an antinode, or suppressed by ~75% when placed on a node. The suppression is sensitive to the beam shape and beam positioning—which we did not fully optimize—so it may be possible to achieve a much higher degree of mode suppression. Suppressing individual modes of a degenerate pair is typically quite hard, since they overlap in frequency, making this technique useful for probing the motion of a single mechanical polarization(148). Placing the drive laser at the point of a mode's maximum response also reduces the need for high laser powers, which can lead to irreversible changes in the device(137). Although we only study the first three modes here, this technique could also be used at higher frequencies, where the dense spectrum of modes can overlap significantly(149).

7.3 Conclusion

In summary, we have combined spatially resolved imaging with a force density model to infer the spatial resolution of the optical drive in a graphene nanomechanical resonator. Despite the fast thermalization, low reflectivity, and micrometer-scale size of the graphene resonator, we found that the optical force is localized to an area slightly larger than the focused laser spot and can selectively and efficiently actuate high-order mechanical modes. The combination of high-spatial-resolution optical drive and read-out enables full multimodal control of suspended 2D nanomechanical resonators for future NEMS applications. Our high-resolution, all-optical approach could be combined with optical beam shaping and spatial light modulation to selectively address an arbitrary subset of resonators within large arrays, a feat not easily achievable with electrostatic gating, or could serve as a point source of propagating mechanical waves for use in 2D nanomechanical circuits(150) and waveguides(151).

7.4 Bridge

In this chapter, we studied the spatial localization of the optical drive process in graphene NEMS and found that it was similar to the laser spot size. By changing the position of the drive laser, we can efficiently and selectively excite various mechanical modes. Such a technique allows for excellent control of the motion in NEMS arrays. In

the next section, we will tackle the problem of controlling the resonance frequency in graphene NEMS.

CHAPTER VIII

NONVOLATILE REWRITABLE FREQUENCY TUNING OF A NANOELECTROMECHANICAL RESONATOR USING PHOTOINDUCED DOPING

From Miller, D. Blaikie, A., and Alemán, B., Non-volatile rewritable frequency tuning of a nanoelectromechanical resonator using photoinduced doping, *Nano Lett.* **20**, 2378-2386 (2020). I performed the fabrication, experimental measurements, data analysis, and am the primary author on the publication. Benjamín Alemán is my supervisor.

8.1 Introduction

Nanoelectromechanical (NEMS) resonators have enabled a broad range of technological and scientific applications, including mass(17), charge(91), and force(18) sensing, and studies of cavity optomechanics(152), nonlinearity(7), and quantum mechanics(92). There is a burgeoning interest to broaden these uses and to discover new functionality—similar to the development of electronic circuits—by building large-scale NEMS resonator arrays, networks, and circuits. Simple NEMS arrays have already impacted areas like infrared imaging(153) and neutral mass spectrometry(22) and hold promise as ultralow-power alternatives to traditional analog electronics(15) in addition to nanomechanical information technologies like memory(154), logic(155), and computing(156, 157). However, these passive arrays suffer from random and unpredictable properties due to variations in their individual resonator components, variations that arise from fabrication imperfections, environmental interactions, and drift. These variations are further exacerbated at the small physical dimensions relevant to NEMS, and severely hinder the potential of NEMS arrays.

In order to achieve arrays with well-defined and controllable properties, it is necessary that the frequency of each individual NEMS resonator be programmable.

At the most basic level—like tuning the strings of a guitar or violin—programmability requires tuning of the resonance frequency that is at once persistent (*i.e.* non-volatile), reversible, repeatable (*i.e.* can be tuned and cycled many times), and scalable to large arrays. At a more practical level, programmability requires that the frequency be tuned quickly and over a large frequency range. In addition to overcoming the practical challenge of variability, programmable NEMS arrays also open many new and exotic opportunities, such as tunable acoustic crystals(150), acoustic invisibility and lensing(158), topological metamaterials(159, 160), and platforms for neuromorphic computing(161, 162) and for simulating complex networks(25).

Numerous NEMS frequency tuning methods(163) have been demonstrated, but in terms of programmability, each has significant drawbacks and challenges. Active tuning methods, such as electrostatic gating(20) and local heating(164), are reversible and can achieve a large tuning range, but they require a continuous, separate external force for each NEMS resonator to maintain its tuned frequency (*e.g.* in the case of gating, a separate analog DC source is needed for each resonator). The inherent transience of these active methods makes them impractical for programmable arrays. Passive methods, which tune the frequency by permanently modifying the NEMS structure (*e.g.* by adding or removing mass(81, 165, 166)), can achieve persistent tuning but at the expense of reversibility, speed, and scalability, making them unsuitable for programming. Some approaches have successfully combined persistence and reversibility, including mass electromigration along suspended carbon nanotubes(167) and etching/depositing of mass with a focused ion beam(168), but these techniques require electron microscopy, serial *in-situ* nanomanipulation, and dedicated power supplies for each device, which severely impedes practicality and scalability. Moreover, these tuning schemes suffer from poor

frequency resolution, a limited tuning range (~10%), slow speed, and limited cyclability.

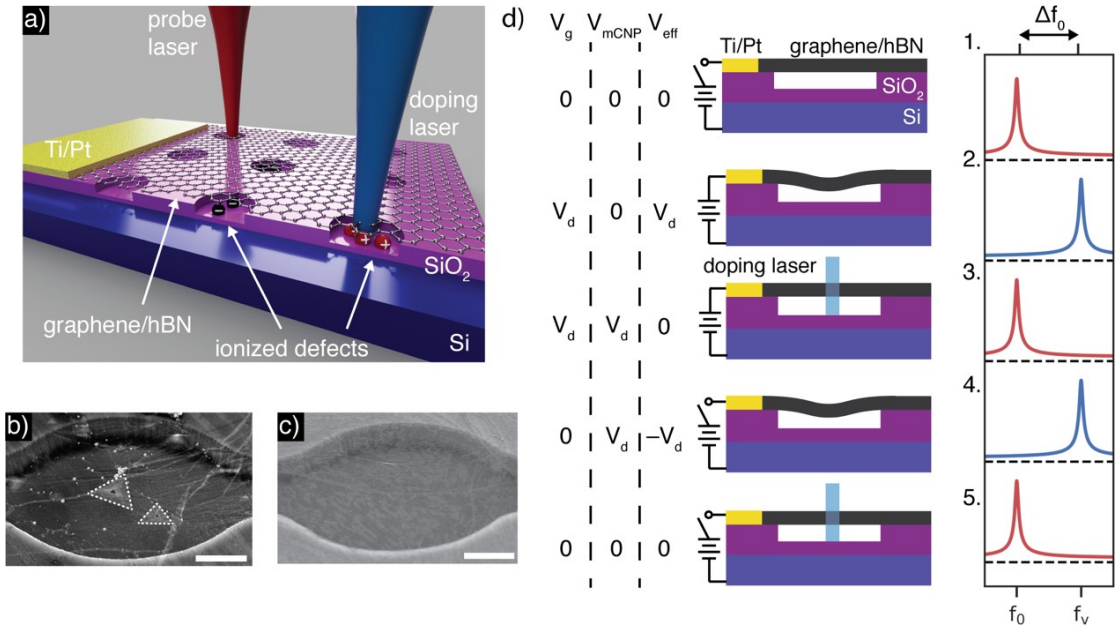

Figure 8.1: Photodoping graphene-based NEMS. (a) Schematic of the phototuning effect in 2D NEMS. b) SEM image of a gr/hBN drumhead with venting trenches on the sides. Small multilayer islands of hBN are visible on the surface. Scale = 1 μm. (c) SEM image of a graphene drumhead. Scale = 1 μm. (d) The frequency tuning sequence is as follows: 1. The device is initially in its intrinsic state with $V_g = 0$ V, $V_{mCNP} = 0$, and resonance frequency f_0; 2. The device is then biased with $V_g = V_F$, tuning the resonance frequency to $f_0 + \Delta f_0(V_F)$; 3. Photodoping the device while $V_g = V_F$ sets V_{mCNP} to V_F and returns the resonance frequency to f_0. 4: With the gate bias off, the device is in its phototuned state with a resonance frequency $f_K = f_0 + \Delta f_0(-V_{mCNP})$, where for the ideal device $V_{mCNP} = V_F$; 5. Photodoping with $V_g = 0$ now returns the device to its initial configuration, with a resonance frequency f_0.

Here, we demonstrate a non-volatile and rewritable frequency tuning method for graphene-based two-dimensional (2D) NEMS(20, 61, 79, 81, 95, 121). In our approach, we use a focused laser and two global electrical contacts to create locally photo-ionized defects(169–173) on an individual resonator. After the optical and electrostatic fields are removed, the trapped charge created by photo-ionization persists and applies spatially localized electrostatic strain to the resonator, thereby

tensioning the resonator and tuning its frequency. Our approach is robustly rewritable over a large tuning range and persistent over many days with no need for external power. Moreover, our approach is exceptionally fast, can locally address individual resonators, and is scalable to NEMS arrays of arbitrary size. By providing a facile means to address the frequency of NEMS resonators, this work lays the groundwork for fully programmable large-scale NEMS lattices, networks, and circuits(160, 174).

8.2 Results

Our frequency tuning method relies on principles similar to electrostatic gate-tuning of graphene NEMS(20, 81). In a typical gate-tunable device, a graphene membrane is suspended above a gate electrode to form a mechanically compliant parallel-plate capacitor, with a capacitance C_S that depends on the membrane deflection z. When an external voltage $V_S$is applied to the gate, the membrane will experience an electrostatic force $F = \frac{8^{>\&_L}}{+>5} y V_{344} z^{+}$ where the effective bias is $V_{344} = V_S - V_{!\&TU}$ and $V_{!\&TU}$ is the mechanical charge neutrality point, a quantity analogous to graphene's electronic charge neutrality point(86). This force will bend and tension the graphene membrane, changing its resonance frequency $f_\$$ by an amount $\Delta f_\$$. In general, $\Delta f_\$$ is a symmetric function about $V_{344} = 0$ where the exact shape and tuning range is determined from the geometric and elastic properties of the device(48, 81). For the devices used in this work, $\Delta f_\$$ increases monotonically with $^{o}V_{344}{}^{o}$ at a rate determined by the value of $^{o}V_{344}{}^{o}$. In graphene-based NEMS, V_{344} is typically offset from V_S by relatively small but non-zero values of $V_{!\&TU}$. The origin of this non-zero $V_{!\&TU}$ has been ascribed to the presence of electrically charged dopants and defects(81, 121). If the density of these charged species were controllable, then it would be possible to modify $V_{!\&TU}$ and thus tune $f_\$$, even in the absence of an external gate bias ($V_S = 0$). This previously unexplored tuning mechanism is the basis of our technique.

We tune the $V_{!\&TU}$ of an individual graphene-based NEMS device with spatially resolved photodoping(169–173). In previous studies of graphene photodoping, graphene is separated from a global gate-electrode by a stack of dielectrics (e.g. hBN and SiO_2)(171). When a voltage is applied to the gate while a laser is focused onto the graphene, the local electronic charge neutrality point of the graphene (*i.e.* the gate bias corresponding to the highest resistivity) changes until it equals the applied gate voltage in magnitude, neutralizing the effect of the gate. This photodoping effect is attributed to the accumulation of photo-ionized defects trapped near the laser focus. Crucially, the trapped charge persists long after the laser and gate are removed, but can also be controllably neutralized and re-ionized by subsequent photodoping, allowing for intricate, long-lived spatial patterning of charged dopants in the heterostructure. In our approach, we exploit photodoping to control $V_{!\&TU}$ and thus tune the resonance frequency of individual graphene membranes. By using a focused, scannable laser, a single global gate electrode, and a single shared electrical top contact, we can address spatially separated resonators in arbitrarily large arrays and program their resonant frequencies.

We study this tuning method in NEMS membranes made from both CVD-grown monolayer graphene and a graphene/hBN heterostructure (gr/hBN). In our device, we suspend the 2D sheet over a circular cavity ($\sim 4-5$ μm in diameter) etched into SiO_2 on top of a degenerately doped silicon gate electrode (see Figure 8.1a-c). Venting trenches, visible on the sides of Figure 8.1b-c, are fabricated between the cavities to protect the suspended sheets from rupture under vacuum(75). A layer of SiO_2 (~300 nm thick) is left at the bottom of the cavities to prevent shorting and create potential charge traps(170). The devices are driven with standard electrostatic actuation techniques(20) using the silicon back-gate and a Ti/Pt top contact, and measured using an interferometer operating at 633 nm(61, 79). Photodoping is performed with a power-stabilized 445 nm diode laser, except where noted otherwise. Both the measurement and doping laser are scanned with independent fast steering mirrors(71), allowing for the array of devices to be rapidly addressed. Devices are measured in vacuum ($< 10^{-^{\wedge}}$ mTorr) to reduce the effect of air damping, to increase

the mechanical quality factor (Q), and to prevent oxidative damage to the 2D membrane.

To set or change the frequency of an individual membrane through photodoping—a process we will call phototuning—we apply a bias to a global back-gate (in this case, degenerately doped silicon) while focusing a laser onto the individual, suspended membrane of interest (see Figure 8.1a,d). Prior to any photodoping (*i.e.* before the laser or bias are turned on) and assuming that $V_{!\&TU} = 0$ V in the undoped state, the resonator will be at its intrinsic resonance frequency $f_{\$}$ (*step 1*). Then, we set the gate voltage to $V_S = V_>$, so that $V_{344} = V_>$, which tensions the membrane and blue shifts the resonance frequency (*step 2*) to $f_{\$} + \Delta f_{\$}(V_>)$. Here, $V_>$ represents the photodoping voltage setpoint. Next, with the gate still at $V_>$, we turn on the laser to photo-ionize defects and create trapped charge, with the value of $V_>$ determining the polarity and density of trapped charge. In our devices, the charged defects are likely both in the hBN(169, 171) and the oxide(170). The generation of this charge brings $V_{!\&TU}$ towards $V_>$, lowering the effective voltage to $V_{344} = V_> - V_{!\&TU}$ and red shifting the resonance frequency. Given enough laser dose, $V_{!\&TU}$ saturates to $V_>$, so that $V_{344} = 0$ and $\Delta f_{\$}(0) = 0$. This returns the frequency to $f_{\$}$ (*step 3*). After turning the laser and bias off, the photo-ionized charges remain, so that $V_{344} = -V_{!\&TU}$ and the frequency blue shifts to $f_{\$} + \Delta f_{\$}(-V_{!\&TU})$ (*step 4*), which is the same as $f_{\$} + \Delta f_{\$}(V_>)$ due to the symmetry of $\Delta f_{\$}(V_{344})$. We denote $f_|$ as the phototuned frequency $f_{\$} + \Delta f_{\$}(-V_{!\&TU})$ obtained after *step 4*. Importantly, $f_|$ persists without an external gate bias (*i.e.* $V_S = 0$). Steps 2-4 complete the phototuning "write" function of our programming platform. The frequency can be reset back to $f_{\$}$—or "erased"—by zeroing the photodoping setpoint ($V_> = 0$ V) and illuminating the membrane with the laser (*step 5*). The frequency does not need to be erased to be rewritten to a different state. To rewrite, steps 2-4 are repeated with a different photodoping setpoint ($V_>$). We note that the description above represents the ideal case of phototuning. For most devices we study, the non-photodoped $V_{!\&TU}$ is slightly offset from zero and $V_{!\&TU}$

saturates to a slightly different value than $V_>$, but neither of these factors affect the key properties of the phototuning method.

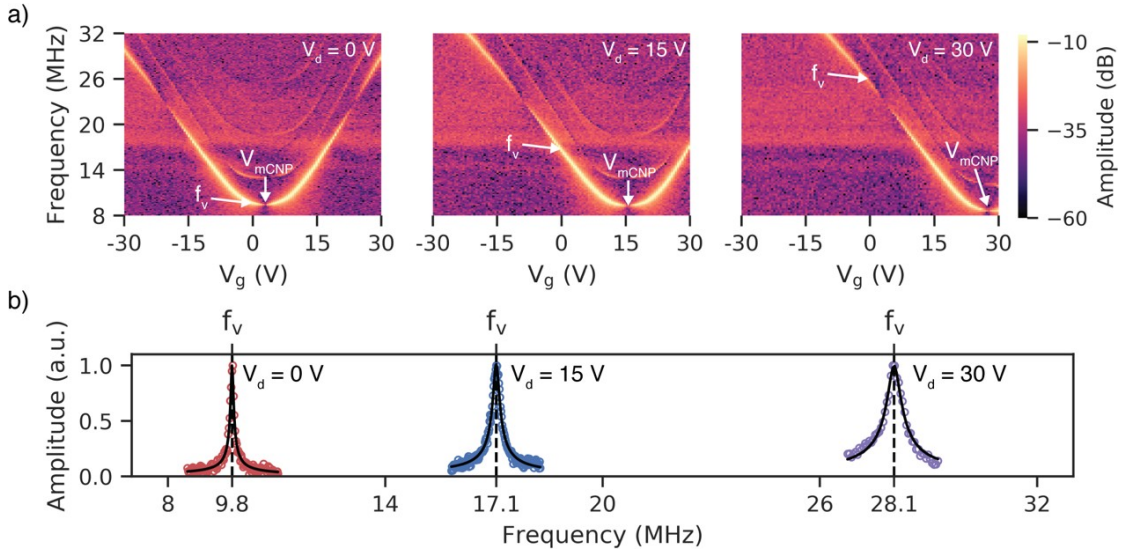

Figure 8.2: Phototuning the resonance frequency of a gr/hBN drumhead. (a) Electrostatic frequency tuning spectra for a gr/hBN drumhead resonator as it is phototuned from the erased state, *i.e.* with $V_F = 0$ V (left), to phototuned states with $V_F = 15$ V (middle) and $V_F = 30$ V (right). The V_{*91J} is initially located at ~1 V and shifts to $V_{*91J} \sim 28$ V after phototuning at $V_F = 30$ V. (b) Resonant response at $V_: = 0$ V for the three different states in (a). f_K is the center frequency in each of these curves. The resonance frequency increases by ~200% and the Q-factor decreases from 135 to 74 between the $V_F = 0$ V and the $V_F = 30$ curves. The maximum amplitude has been independently normalized to unity for all three resonance curves.

Phototuning creates local charge on the graphene membrane that tensions the membrane and shifts its resonance frequency. These photo-ionized charges also generate an electrical potential given by $V_{!\&TU}$ and modulate the gate-dependence of amplitude resonance spectra. The effect of $V_{!\&TU}$ on the membrane is indiscernible from an electrostatic gate bias, yet exists in the absence of an external bias. To observe these basic effects, we first set the gate to $V_>$ and raster the laser (at relatively high power, ~1 mW/μm^2) over the area of the membrane, and then collect spectra. The

resulting electrostatic frequency tuning spectra for a gr/hBN device in the erased state ($V_> = 0$ V) and two phototuned states ($V_> = 15, 30$ V) are shown in Figure 8.2a.

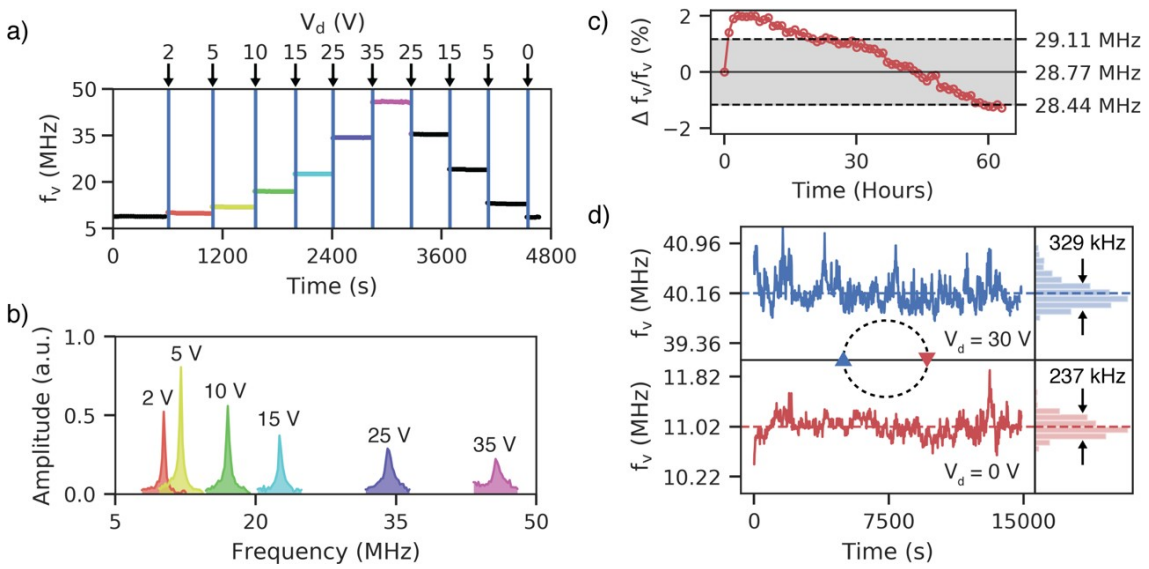

Figure 8.3: Stability and repeatability of the phototuning process. (a) Setting the frequency in time. A combined high-power optical pulse of ~1 mJ and gate voltage V_F are applied at the times indicated by arrows. (b) Resonance spectra taken with $V_: = 0$ V immediately after photodoping for the corresponding V_F in a. The amplitude varies due to different transduction and actuation efficiencies at the different values of V_{MNN}. (c) Stability of f_K with $V_: = 0\ V$ after phototuning to 28.77 MHz. After an initial jump of 2%, the f_K decays at a rate of ~0.05%/Hour. The gray band shows the mechanical linewidth corresponding to a Q of 74. (d) Reproducibility of f_K for 919 complete cycles of phototuning with $V_F = 30$ V followed by erasure with $V_F = 0$ V. The f_K value falls within a ~0.33 MHz band for both states.

The fundamental mode has the highest contrast, but several higher order modes are also resolved; we infer $V_{!\&TU}$ as the gate bias where the fundamental mode is at its minimum frequency. The individual resonance curves collected at $V_S = 0$ V for these same three states are shown in Figure 8.2b; we infer $f_|$ from these spectra. In the erased state, $V_{!\&TU}$ is offset from zero by ~1 V, which indicates the presence of static charged contaminants(81, 121). In the erased state, $f_| = 9.8$ MHz (Figure 8.2b, red curve) and the resonator quality factor is $Q = 135$. In the phototuned states with $V_> =$ 15 V and $V_> = 30$ V, $V_{!\&TU}$ saturates to ~15.7 V and ~28 V, respectively. Moreover, in the tuned states, $f_|$ has shifted to 17.1 MHz ($V_> = 15$ V) and 28.1 MHz ($V_> = 30$ V),

and the Q decreases (*e.g.* to $Q = 74$ for $f_1 = 28.1$ MHz). Although the tuned state with $f_1 = 28.1$ MHz differs from the erased state by $\sim 200\%$ and $V_{!\&TU}$ differs by $\sim$27 V between these states, the gate-dependence of each mode relative to $V_{!\&TU}$ doesn't change. Thus, apart from the $V_{!\&TU}$ shift, the phototuning process does not alter the mechanical characteristics of the device in any significant way, in contrast to most passive tuning methods(81, 164, 166). Based on the shape of the resonance frequency curves (extracted from the peak amplitudes), the force on the membrane due to $V_{!\&TU}$ is equivalent to an external gate bias(20, 81). Also, the peak amplitude and Q for all modes decreases with $^{o}V_{344}{}^{o}$, just as it would with an applied electrostatic backgate(95). Moreover, for each tuned state, the amplitude of the fundamental mode vanishes when $^{o}V_{344}{}^{o} \approx 23.6$ V at a frequency of $\sim$23 MHz. The amplitude is expected to vanish when the membrane displacement leads to destructive interference(48) in the optical signal, providing further evidence that $V_{!\&TU}$ is generated by local electric charge, charge that physically deflects the membrane.

To demonstrate the reversibility of f_1 using phototuning, we change f_1 at discrete time intervals by varying the doping potential. At the beginning of each interval, we phototune the device using a single short, high power laser pulse of $\sim$1 mJ ($P\sim$2 mW, $t = 0.5$ s) at a given $V_>$ (Figure 8.3a), and then continuously monitor the f_1 by fitting the resonance spectra (Figure 8.3b) for the remainder of the interval, $\sim$600 seconds. Increasing $V_>$ stepwise from 0 to 35 V (as seen in Figure 8.3a), f_1 takes on fixed, stable values that increase from 7 MHz up to 45 MHz. When we decrease $V_>$ stepwise back to 0 V, f_1 returns to 7 MHz. This data clearly demonstrates that the phototuning of f_1 is both reversible and bidirectional. The tuning range of f_1 is large, here nearly 550%, which is an order of magnitude larger than any previous hybrid tuning method(167, 168). In our measurements, we limited the doping potential to 35 V to avoid damage

to the mechanical resonators, but larger potentials up to the dielectric breakdown of the SiO_2 could be used to achieve an even higher degree of tuning.

The phototuned frequency states persists for several days with minimal change. This persistence is clear from the steps in Figure 8.3a, which show f_1 is stable for at least 600 s. To assess the longer-term stability of phototuning, we write f_1 a single time and then measure f_1 every hour over the course of 3 days. Figure 8.3c plots the fractional change $\Delta f_1/f_1$ after phototuning f_1 with a doping potential of 30 V. Immediately after photodoping, the f_1 of this device blueshifts by 2% over the course of 2 hours. This blueshift is only seen in some devices, and the effect could be due to the slow thermal relaxation of surface contamination (*e.g.* PMMA) that follows laser heating(62), or possibly to the rearrangement of trapped charge. After this initial detuning, the f_1 slowly redshifts at a rate of 0.05%/hour, resulting in a total frequency shift only one linewidth after 30 hours. For reference, the mechanical linewidth for our devices is ~2% of the resonance frequency (shaded region of Figure 8.3b). The slow redshift of f_1 may be ascribed to diffusion and/or recombination of the ionized defects, or to the probe laser. To isolate the effect of the probe laser, we set f_1 and measure it once after 8 days (see Supplementary Figure D.1). In addition to a small amount of detuning, we also observe warping of the electrostatic frequency tuning spectrum, suggesting that additional sources of detuning are present, which may include the rearrangement of the trapped charge in the oxide or hBN, or strain relaxation (*e.g.* in folds and edge clamping). Detuning driven by thermally-induced recombination of the ionized defects(169) could be reduced by operating at cryogenic temperatures. Given the time scale of the drift, phototuning feedback would be a straightforward means to stabilize the frequency. Nevertheless, the long-lived phototuned f_1 state does not require an external power supply or gate bias, in contrast to conventional externally biased NEMS resonators. Therefore, phototuning can replace DC voltage sources and patterned gate electrodes(150, 174) with the use

of a single voltage source and a single scannable laser, making our phototuning approach uniquely scalable to arbitrarily large resonator arrays.

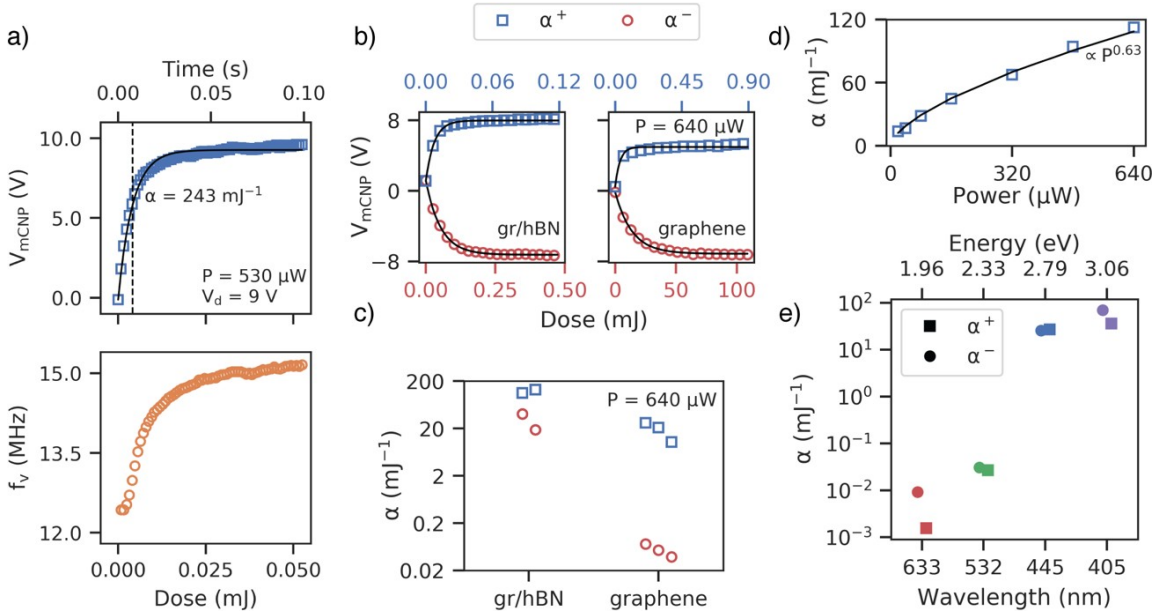

Figure 8.4: Measurement of the photodoping rate. The laser wavelength is 445 nm except in e. (a) Top: Example of a single photodoping curve with $V_F = 9$ V. The black line is an exponential fit to the data with $\alpha = 243$ mJ^{-1}. Bottom: Same data for f_K. The optical power for the is measurement is $P \sim 530$ μW. (b) Photodoping curves for $\Delta V > 0$ in blue (α^0 branch) and $\Delta V < 0$ in red (α^- branch) for a typical gr/hBN device and a graphene-only device. The laser power is 640 μW and $V_F = \pm 8$ V for all the measurements. c) Doping rates for both α^0 (blue squares) and α^- (red circles) for 640 μW, 445 nm irradiation for two gr/hBN and three graphene devices. For the α^0 branch of the graphene devices, which don't saturate close to V_F, we take the initial slope of $V_{*91J}(E)$ and divide by V_F to obtain α. (d) Laser-power dependent doping rate for the α^0 branch of one of the gr/hBN devices in c. The black line is a fit to the function $\alpha = \alpha_\gamma P^P$, with $\gamma = 0.63$. (e) Photodoping rates of a gr/hBN device for both the α^0 (squares) and α^- (circles) branches for different doping laser wavelengths. Data was collected using 405 nm, 445 nm, 532 nm, and 633 nm illumination all at 20 μW. For the 532 nm and 633 nm laser illumination where photodoping is extremely slow, we use the same linearized doping rate defined in c.

The phototuning method can achieve a high degree of frequency tuning repeatability and can execute an indefinite number of write/erase cycles with no observable change to the mechanical properties of the NEMS device. To test repeatability and

cycling performance, we erase the frequency state by phototuning with $V_{>} = 0$ V, then we write $f_{|}$ with $V_{>} = 30$ V. For all writing and erasure steps, the same dose of 1 mJ was used. Figure 8.3c shows the results after 919 erase/write cycles. As measured from the histogram (right of Figure 8.3d), the average frequencies of erased and written states are $f_{3DIÅ3} = 11.02 \pm 0.12$ MHz and $f_{ÇD1R3} = 40.16 \pm 0.16$MHz, which yields a writing repeatability of 99.5%. The small uncertainty in the repeatability could be inherent to the phototuning process, but could also be caused by sources of frequency noise and fluctuations common to 2D NEMS, such as adsorbates, heating, and unwrinkling(61). The large frequency separation of the written and erased states in Figure 8.3a,c could easily allow a discrete binary logic state(154, 175). Alternatively, the frequency states can represent discrete levels for logic or memory applications(162, 176), where information is encoded in the frequency of each resonator. For example, with the frequency separation (29.14 MHz) and the average full-width-half-maximum as the write error (283 kHz) shown in Figure 8.3d, it is possible to define over 100 discrete and well-defined logic states.

The photodoping rate will ultimately determine the number of devices that can be controlled with the phototuning method, or how quickly the state of an individual device can be changed. This rate can be inferred from the dependence of either $f_{|}$ or $V_{!\&TU}$ on the accumulated dose during the phototuning process (see supplementary information), where the accumulated dose is the total optical energy ($E = P \times t$) delivered to the devices at a given power P and over a time t. Figure 8.4a shows a plot of $V_{!\&TU}(E)$ (blue, upper) and $f_{|}(E)$ (orange, lower) for $V_{>} = 9$, and P~530 μW with a 445 nm laser. Both $V_{!\&TU}$ and $f_{|}$ approach steady state saturation values within ~25 ms, equivalent to a total dose of ~15 μJ. As noted earlier, we find that $V_{!\&TU}$ does not saturate exactly to $V_{>}$, but each device has a small but consistent offset, which we

denote $\delta V_{!\&TU}$. To obtain the doping rate α (measured in units of inverse energy, mJ^{-1}), we model $V_{!\&TU}(E)$ with a saturation function of the form,

$$V_{!\&TU}(E) = \Delta V(1 - e^{-\ddot{A}\acute{E}}) + V_{\$} \quad (8.1)$$

where $\Delta V \approx V_{>} - V_{\$} + \delta V_{!\&TU}$ and $V_{\$}$ is the initial $V_{!\&TU}$ before additional photodoping. Prior to each rate measurement, the device is photodoped at high power with $V_{>} = 0$ V, which initializes $V_{\$}$ to $\delta V_{!T\&U}$. The black trace in the upper plot of Figure 8.4a is the fit for $V_{!\&TU}(E)$ using Eq. 8.1, with fit parameters $\Delta V = 8.94$ V and $\alpha = 243$ mJ^{-1}. The saturation offset $\delta V_{!\&TU}$ exhibits a large asymmetry in graphene devices. In gr/hBN devices, $\delta V_{!\&TU}$ is less than 15% of $V_{>}$ regardless of the polarity of ΔV. However, in graphene devices, when $\Delta V > 0$, $\delta V_{!\&TU}$ can be as large as ~50% of $V_{>}$ (Figure 8.4b), indicating that not enough ionized defects or dopants are being created to neutralize the effect of the applied gate. Although we observe α to be independent of ΔV for a given polarity, we do find that α depends on several factors, including the device material (graphene vs. gr/hBN), the polarity of ΔV, the optical power, the wavelength of light, and the doping laser position(172, 173).

The photodoping rate is larger for gr/hBN devices and when $\Delta V > 0$. We measure α with optical power ranging from $20 - 2540\ \mu W$ (see Supplementary Figure D.3 for full power range) with a blue doping laser (445 nm) and $V_{>} = \pm 8$ V. The results for two graphene/hBN and three graphene-only devices (Figure 8.4b-c) show several features. First, the photodoping rate depends on whether $\Delta V < 0$ (α^{-} branch) or $\Delta V > 0$ ($\alpha^{\mathbf{J}}$ branch) (Figure 4b). For all devices, $\alpha^{\mathbf{J}} > \alpha^{-}$, but the difference can vary greatly. For the gr/hBN devices, $\alpha^{\mathbf{J}} \sim 2\alpha^{-}$, which is in contrast to a previous study using exfoliated hBN(169), where $\alpha^{-} \sim 10^{+} \times \alpha^{\mathbf{J}}$. For the graphene-only devices, $\alpha^{\mathbf{J}} \sim 10^{:} \times \alpha^{-}$ (Figure 8.4c). In either case, the high rate of the $\alpha^{\mathbf{J}}$ branch could be due to an increased defect density or to a lower ionization energy for the acceptor-type defects in CVD hBN(177), surface contaminants, or the SiO_2(170). Next, α for gr/hBN devices is greater than for graphene-only devices, regardless of branch, although the difference is significantly larger for the α^{-} branch, which can differ by a factor of $10^{+} - 10^{:}$ (Figure 8.4c). These differences in the rates and the value of $\delta V_{!\&TU}$

between the gr/hBN and graphene-only devices suggests that the gr/hBN heterostructure has a relatively higher density of ionizable dopants and/or a lower dopant ionization energy, consistent with previous reports of electronic photodoping(169–173).

We find that the phototuning rate is not purely determined by the accumulated energy but also by the optical power. Figure 8.4d illustrates the behavior of $\alpha(P)$ for the $\alpha^{\mathbf{J}}$ branch of a gr/hBN device with laser power increasing from 20 – 640 μW. Both α branches increase with the optical power consistent with a power function $\alpha(P) = \alpha_{\$} P^{s}$. Fitting the data Figure 8.4d (solid black curve), we find $\gamma = 0.63$. In general, γ is between $0.4 - 0.6$ for gr/hBN devices and $0.2 - 0.7$ for the graphene devices (see Supplementary Figure D.3). The non-zero value of γ is potentially due to local laser-induced heating of the suspended 2D sheets(79), which would lower the energy barrier between the donors (acceptors) and the conduction (valence) bands, increasing α. Even faster phototuning should be possible with higher laser power since both graphene and hBN are stable at high temperatures(63).

The phototuning rate is greater for shorter wavelength light. To characterize the wavelength dependence of α, we measure α in a gr/hBN device using four different laser wavelengths (633, 532, 445, 405 nm) with an optical power of 20 μW and $|V_{>}| =$ 8 V. The results (Figure 8.4e) show that shorter wavelength, higher energy illumination leads to much faster phototuning. Compared to 633 nm light ($\alpha^{\mathbf{J}} = 9.2 \times 10^{-:}$ mJ^{-1} and $\alpha^{-} = 1.5 \times 10^{-+}$ mJ^{-1}), α for 405 nm light ($\alpha^{\mathbf{J}} =$ 70 mJ^{-1} and $\alpha^{-} =$ 36 mJ^{-1}) is larger by a factor of $\sim 10^{=}$. The rate increase also appears to be saturating near 3 eV. The enhanced phototuning at shorter wavelengths agrees with previous photodoping studies in hBN as well as SiO_2(169–171). The wavelength dependence of α is advantageous for nanomechanics experiments, as it allows selection of a long-wavelength laser for transduction, which has a negligible phototuning effect, and a short-wavelength laser for phototuning. We note that higher photon energies likely

also induce photodoping, which could explain the frequency shifts seen in γ-ray irradiated 2D sheets(178).

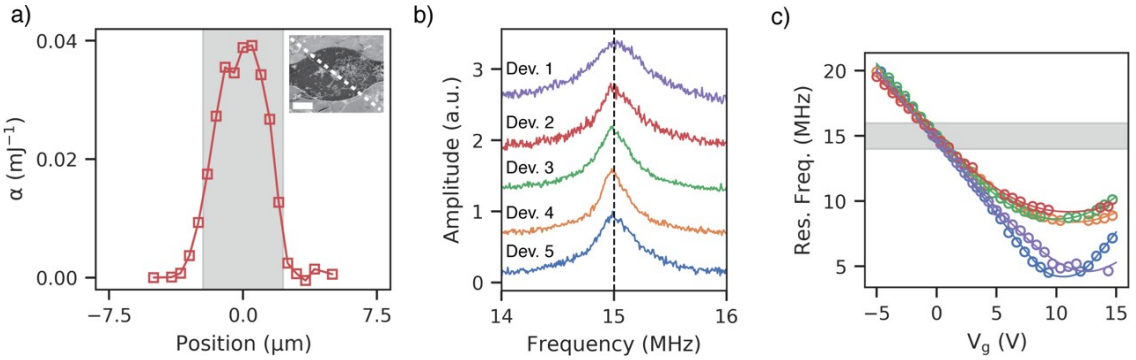

Figure 8.5: Aligning the resonance frequencies of neighboring gr/hBN NEMS. (a) Photodoping rate as the doping laser is scanned across a gr/hBN drumhead. The scan line is indicated in the SEM image inset. The doping rate reaches a maximum at the center of the drum and rapidly falls off as it is swept away. The gray band indicates the spatial extent of the device. Scale = 1 μm. (b) Resonant response for five different gr/hBN devices displaying alignment of f_K to 15 MHz of less than 99.8%. The alignment is achieved with no external electrical gate bias. (c) Electrostatic frequency tuning curves for the fundamental mode of the five devices from b (the data color corresponds to each device) after being simultaneously phototuned to $f_K = 15$ MHz. The gray horizontal band corresponds to the $14 - 16$ MHz plot range of b.

The temporal rate of phototuning, $\frac{\geq 4^{Q}}{>}$, depends on the value of $V_{!\&TU}$, and can exceed 1.75 GHz/s when $V_{!\&TU}$~35 V .(see s Using Eq. 1 and electrostatic frequency tuning curves $f(V_S)$ (*e.g.* curves extracted from the maximum amplitude of spectra in Figure 8.4a), we find an expression for the temporal rate, $\frac{\tilde{N}4^{Q}}{>R} = \alpha P \Delta V \, w\frac{>4}{>|_L} x$, where $\frac{>4}{>|_L}$ is the slope of the photodoped gate voltage tuning curve at $V_S = 0$ V (*i.e.* at $f_|$). See supplementary information for the derivation of $\frac{\geq 4^{Q}}{>R}$. The $\frac{>4}{>|_L}$ is determined by the device geometry(61, 81) and strain, and could be increased by using small area devices or shallower cavities. For our devices, the maximum values of $\frac{\geq 4}{>|_L}$ are typically between $0.8 - 1.4$ MHz/V, and these max values are achieved in the range $V_{!\&TU} = 5 - 15$ V (see Supplementary Figure D.2). For a typical gr/hBN device, we observe

$\alpha P \sim 50$ s^{-1} with 500 μW of incident optical power, (see Figure 8.4b-d and Supplementary Figure D.3). Thus, with $\frac{\geq 4}{> \mathrm{I_L}} \sim 1$ MHz/V and $\Delta V = 1$ V, we obtain a tuning rate of $\frac{\tilde{N}4Q}{>R} = 50$ MHz/s. We note that $\frac{\tilde{N}4Q}{>R}$ characterizes the change in the steady-state f_{I} for a particular dose, not the dynamic change in f_{I}, which is limited by the RC time constant of the device (~1 μs). Still, the frequency tuning rate of phototuning is exceptionally fast; for example, with a moderate bias voltage of ΔV~10 V and optical power less than 1 mW, it is possible to tune a resonator by its full linewidth ($\Delta f_{\ddot{\mathrm{U}}} \sim 100$ kHz) in a time $\frac{\grave{a}\frac{\tilde{N}4_Q}{>R}\hat{a}^{-8}}{\ddot{\mathrm{U}}} = \sim 100$ μs, or equivalently, to tune 10 resonators in one second.

Many applications in NEMS circuits and lattices require precise, programmable frequency and strain tuning of individual resonators within large arrays on a single chip(150, 174). To demonstrate this capability with phototuning, we first show that the effect is localized to the laser spot Figure 8.5a shows the doping rate at 20 μW measured at different locations on the membrane. The device begins to photodope only when the gaussian spot of the laser overlaps with the area of the membrane. We use the dilation of the spatial doping rate profile relative to the device diameter (grayed region in Figure 8.5a) to infer a spatial resolution of ~1 μm, which is approximately the size of the laser spot. Next, we align the frequencies of five different gr/hBN devices, which are all on a single chip. Even without tuning with feedback, we tune the resonators to within 30 kHz of $f_{\mathrm{I}} = 15$ MHz (Figure 8.5b), which aligns the frequencies within ~5% of a resonance linewidth and achieves a tuning precision of 99.8%. The electrostatic frequency tuning curves (extracted from amplitude maxima of the fundamental mode) for each device are shown in Figure 8.5c. While the curves intersect at $V_{\mathrm{S}} = 0$ V, which defines f_{I}, the values of $V_{\mathrm{!\&TU}}$, the minimum frequency (*i.e.* at $V_{\mathrm{!T\&U}}$), and the general curve shape vary considerably. Based off SEM images (see Supplementary Figure D.4), each device also differs markedly in terms of geometry (*e.g.* number of trenches), surface contamination, and macroscopic defects (*e.g.* tears, grain boundaries, wrinkles, holes). This demonstrates that phototuning is

largely insensitive to variations between individual resonators and is thus a robust frequency tuning method.

8.3 Discussion

The phototuning effect we demonstrate in graphene and gr/hBN NEMS could be applicable to other types of NEMS. Persistent photodoping has been observed in a variety of graphene heterostructures(170, 171, 179) as well as other materials including $SrTiO_3$(180). In these systems, the mechanical element does not need to be an atomically thin membrane, like graphene or a graphene heterostructure. For example, it might be possible to phototune graphene-coated silicon nitride nanobeams(37), which would offer the benefit of an ultra-high quality factor ($Q > 10^{-}$.) However, atomically thin resonators have the great advantage of an extreme tuning range.

Phototuning offers intriguing possibilities for both applied and fundamental physics in isolated NEMS and NEMS arrays, where tight control over individual resonators is essential. Our technique can pattern arbitrary complex geometries of static charge across a single, large-area resonator, which could improve the actuation efficiency of antisymmetric modes or allow tunable intermodal coupling(61), both commonly achieved via intricately patterned back-gates. Furthermore, this tuning also offers new opportunities for programmable NEMS crystals. In our vision for these crystals, individual resonators would be coupled to neighboring resonators by a suspended bridge material. By phototuning the resonators and the bridges, precisely tuned complex acoustic crystals would be possible. Unlike previous demonstrations of static phononic crystals(92, 160) and tunable phononic crystals(150), our approach is not vulnerable to fabrication imperfections and possesses a higher degree of tunability and the ability to modify individual unit cells of the crystal.

8.4 Conclusion

In conclusion, we have demonstrated a fast, reversible, persistent, and scalable frequency tuning method based on deterministic charge trapping, which allows for electro-optic "etch-a-sketch" patterning of strain in 2D NEMS arrays. Our phototuning

technique eliminates the need for complex, lithographically defined gate electrodes used to electrostatically strain and frequency tune NEMS resonators. When applied to large NEMS lattices, this approach could enable reprogrammable phononic crystals and waveguides(160, 174), or more exotic applications such as nanomechanical logic, neuromorphic computing(161, 162), or the simulation of complex networks(25).

CHAPTER IX

CONCLUSIONS AND FUTURE WORK

9.1 Future work

This work lays the groundwork for future studies with arrays of graphene NEMS. Due to their high quality factors and anomalously high thermal resistance(47, 153), the graphene trampolines shown in Chapter V have great promise for high-resolution sensing. These experiments are underway and our lab recently demonstrated graphene trampolines for fast and sensitive room-temperature nanomechanical bolometry(46). Scaling such devices up could allow for new, ultrafast thermal imaging cameras. However, much additional work remains to be completed. For example, integrating electronic readout(81) into the FIB-shaped geometries would increase their efficacy as sensors. It would also be interesting to explore the use of graphene trampolines as multi-modal sensors. For example, a graphene trampoline could simultaneously measure adsorbates the energy of a particle and its mass.

The phototuning method we demonstrate in Chapter VIII has the potential to revolutionize the field of array-based NEMS. Although many frequency tuning methods exist, none simultaneously allows for a large array of devices to be rapidly and repeatably programmed. This would not only solve long-standing problems combatting fabrication imperfections, first identified in the resonant-gate transistor, but would allow for a suite of potentially disruptive applications in nanomechanical computation. For example, NEMS arrays have been suggested for neuromorphic computing(164), however this requires fine control of the initial state of each resonator. By phototuning each resonator to the desired initial state and tuning the coupling between individual resonators, it should be possible to realize a nanomechanical neuromorphic computer.

Finally, further exploration of high-Q graphene NEMS is also a promising research direction and could lead to the use of graphene NEMS in quantum optomechanics. Our

work in Chapter VI shows that that the Q in graphene NEMS is governed by dissipation dilution but is limited by large out-of-plane wrinkles. By reducing or removing wrinkles through pre-stress(128, 181, 182) or FIB irradiation, it should be able to achieve much higher quality factors in graphene NEMS. Furthermore, by applying the same engineering strategies used in SiN(34) it might be possible to achieve truly massive quality factors in graphene. For a membrane where the edge-bending is reduced via a phononic crystal, $Q \sim Q_{\$} \times \frac{a}{t}$. Given the experimentally measured tensile breaking strength of ~20 N/m in CVD graphene(139), the theoretical bending stiffness without wrinkles (~10 eV), our experimentally measured $Q_{\$}$, and a moderate device radius of 10 μm, $Q > 10^{8\$}$ could be achievable, surpassing the highest values attained in SiN. Even relaxing some of these values, $f_{\$} \times Q > 10^{8+}$ should be readily achievable in graphene NEMS, allowing for quantum optomechanics at room temperature(35). Such devices would also have exceptional sensitivity to masses and forces due to the combination of high Q and low mass, making them attractive for mass sensing(5, 27, 143) and MRFM(18, 30). To this end, we have begun fabrication of large-area graphene NEMS on nanopillars(183), which we plan to cut out using FIB to generate a phononic crystal.

9.2 Concluding Thoughts

In conclusion, this body of work represents a significant advancement in our ability to build viable arrays of NEMS. In Chapter IV and Chapter V, we showed that FIB milling is an effective way to modify the geometry, tune the mode shape, and enhance the mechanical properties of graphene NEMS. In Chapter VI, we demonstrated that dissipation dilution is an effective theory to describe the Q in graphene NEMS and that the Q can be greatly enhanced using similar strain and shape engineering techniques to those used in SiN. In Chapter VII, we presented a study of optical actuation methods, allowing for fine control of the actuation efficiency of various mechanical modes. Finally, in Chapter VIII, we showed that photoinduced doping of graphene NEMS is a means to persistently and reversibly tune their resonance frequencies, potentially enabling large-scale NEMS arrays and circuits. Together,

these studies demonstrate that graphene has great potential for applications for both single NEMS as well as large NEMS arrays.

APPENDIX A

SUPPLEMENTARY INFORMATION FOR CHAPTER IV

From Miller, D. & Alemán, B. Shape tailoring to enhance and tune the properties of graphene nanomechanical resonators. *2D Mater.* **4**, (2017)

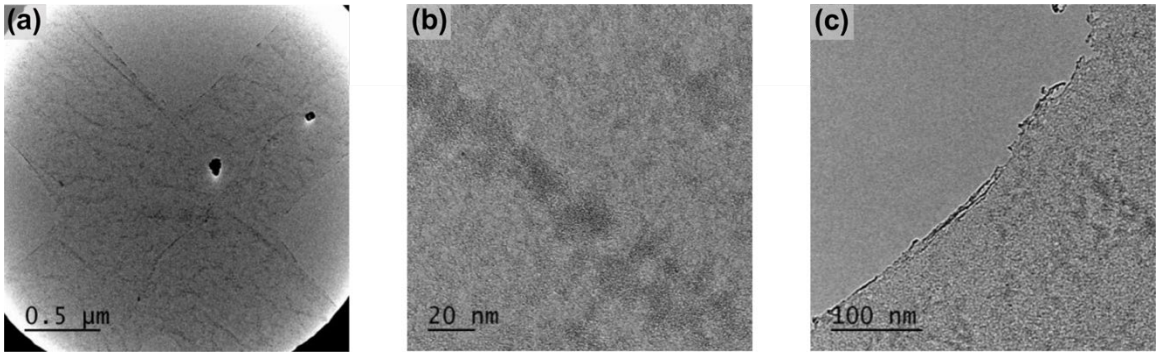

Supplementary Figure A.1**:** Transmission Electron Microscopy (TEM) images of Focused Ion Beam (FIB) cut devices taken with an FEI Titan operating at 80kV. (a) TEM image of a graphene cross. The black dots are contaminants remaining from the transfer process. (b) Higher magnification image of the same graphene cross. Polymer contamination leftover from the transfer process is visible as the darker contrast regions. (c) Rough edge after FIB milling similar to the one shown in the main text.

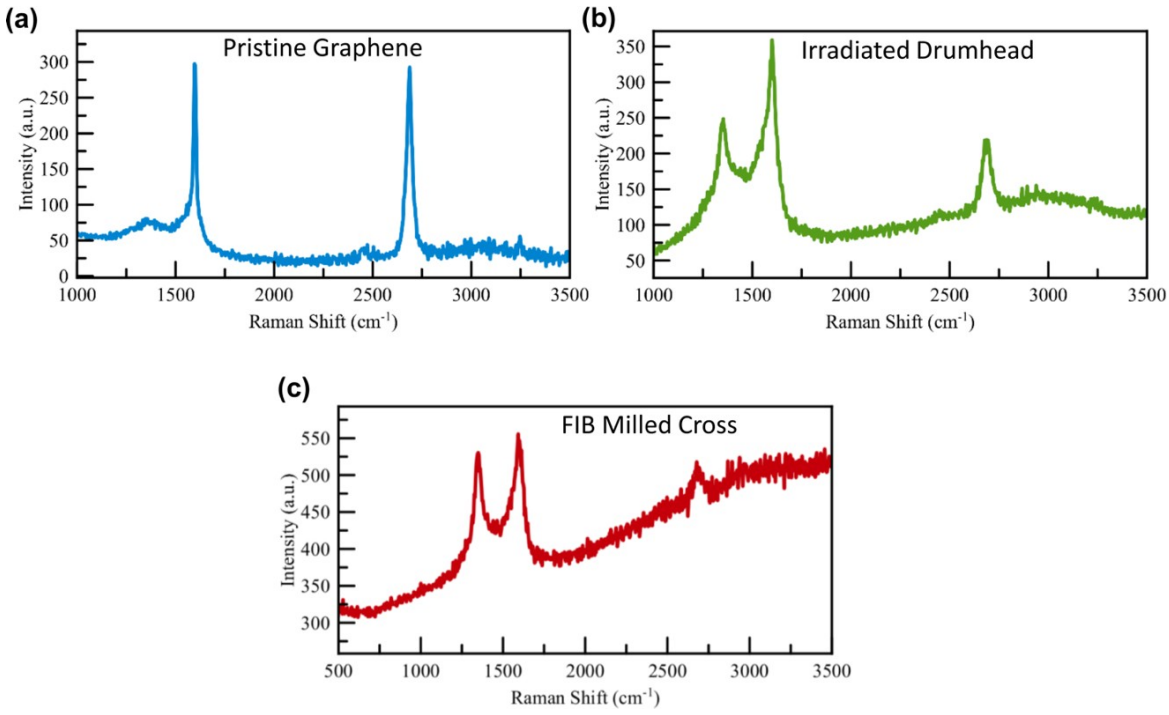

	I_G (a.u)	I_{2D} (a.u)	I_D (a.u)	G (cm^{-1})	2D (cm^{-1})	D (cm^{-1})	$FWHM_G$ (cm^{-1})	$FWHM_{2D}$ (cm^{-1})	$FWHM_D$ (cm^{-1})
Pristine Graphene	245±3.3	256.5±2.9	30.0±0.9	1598.0±0.2	2686.6±0.2	1366.9±3.6	7.7±0.3	32.2±0.5	94.13±5.7
Irradiated Drumhead	213.5±15.5	97.14±2.7	139.3±5.8	1600.8±1.2	2688.4±1.4	1355.5±6.0	23.3±5.8	46.6±1.8	65.58±10.0
FIB Milled Cross	129.2±3.7	38.70±17.7	178.0±2.4	1600.9±0.6	2682.0±15.7	1347.6±0.4	55.8±3.0	68.7±44.4	66.8±1.6

Supplementary Figure A.2: Raman spectroscopy of FIB milled graphene. (a) The Raman spectrum of the graphene prior to milling has an I2D/IG ratio of ~1 and a sharp 2D peak with a FWHM of ~32 cm^{-1}. The I2D/IG is low compared to as-grown CVD monolayer graphene but is typical of annealed, single-layer graphene (86), as described by the supplier of the graphene. We also fit a broad peak underneath the G peak, which is indicative of carbonization of hydrocarbon residue during annealing. (b) The nanomechanical drumheads that have been briefly exposed to the ion beam show signs of damage and modified lattice strain, evidenced by an increased D peak intensity and a lower 2D peak intensity (48, 81). The FWHM of both the G and D peaks increases as well. (c) The milled devices show a continuation of the trends seen in the FIB exposed drumheads, indicating a higher defect density. Additionally, the edges of the cut devices are expected to contribute to the enhanced D-peak (81, 121). All Raman spectra were obtained with a WITEC alpha300 Raman microscope with a 532 nm excitation laser. The laser power was kept low to avoid damaging or heating graphene.

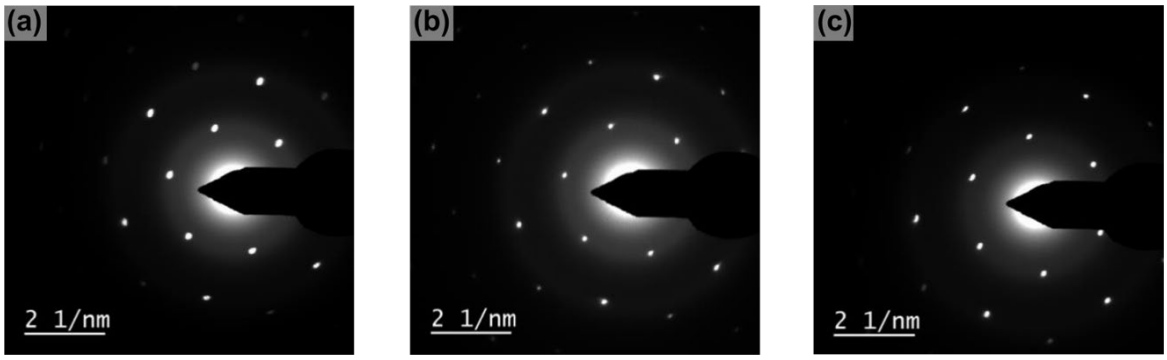

Supplementary Figure A.3: Selected Area Electron Diffraction (SAED) of the graphene devices before and after FIB irradiation. (a) SAED of a pristine graphene drumhead imaged far away from the milled region. The single set of diffraction spots confirms that the graphene is single grain. Some slight rotation of diffraction spots is observed and is likely due differential strain and fold defects in the graphene. (b) SAED image of a graphene drumhead which has been irradiated with a FIB 'snapshot', equivalent to a dose of ~ .0007 pC/μm^2. (c) SAED of a graphene cross. Despite the FIB irradiation, the graphene possesses a diffraction pattern corresponding to single-crystal graphene.

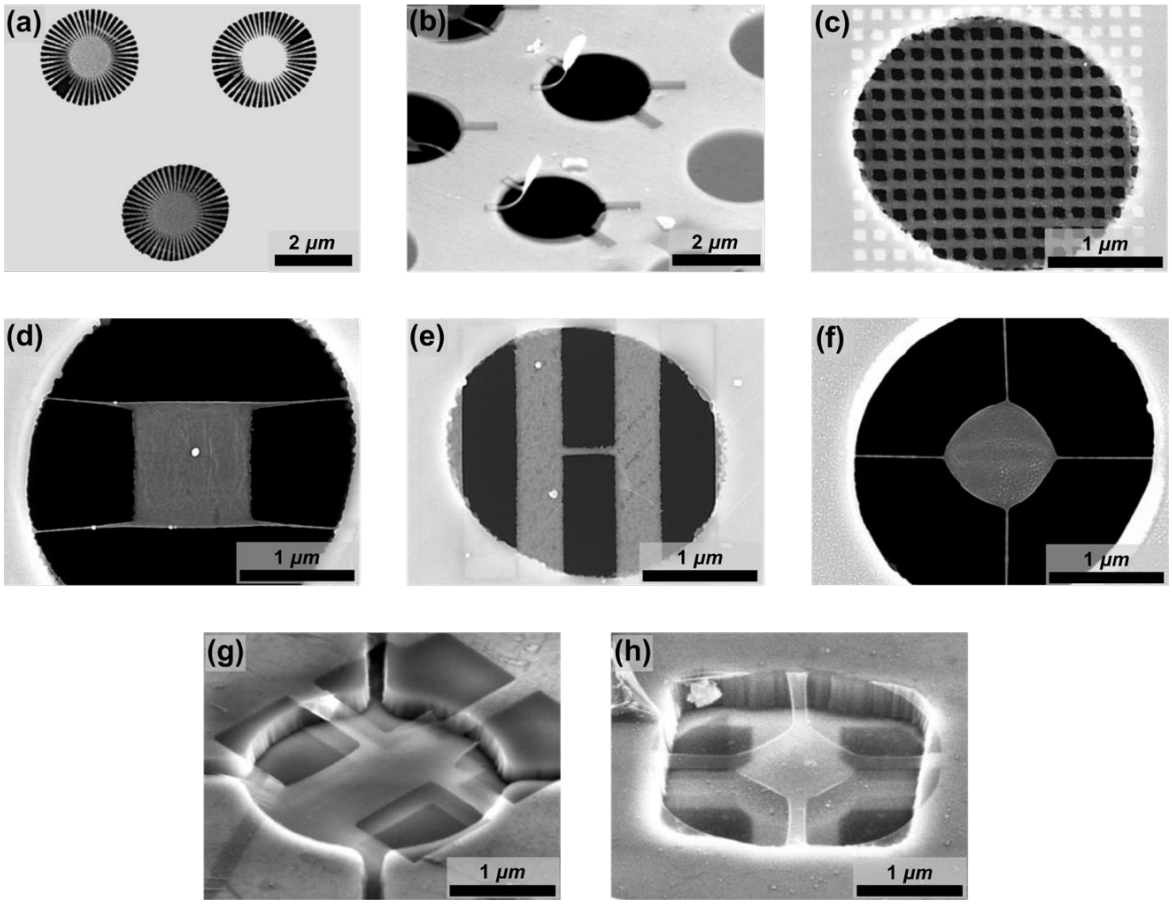

Supplementary Figure A.4: Additional SEM images of selected devices (a) "Trampoline" devices consisting of 48 individual tethers ~40 nm in width. (b) Due to the low bending rigidity of graphene, all cantilevers bend upwards to some degree but the effect is exaggerated after optical characterization at high power (c) Mesh cut into graphene with pitch ~100 nm. (d) Doubly-clamped suspended 'H' structure. The tethers are similar to the scrolled graphene shown in the main text. (e) Finished coupled beam geometry with ~500 nm beams mechanically coupled through a ~50 nm tether. (f) Trampoline style device with tethers of scrolled graphene. (g) Tethered cantilever style resonator fabricated over a cavity using CVD graphene transferred using the techniques described in (169–173). (h) Trampoline resonator fabricated over a cavity.

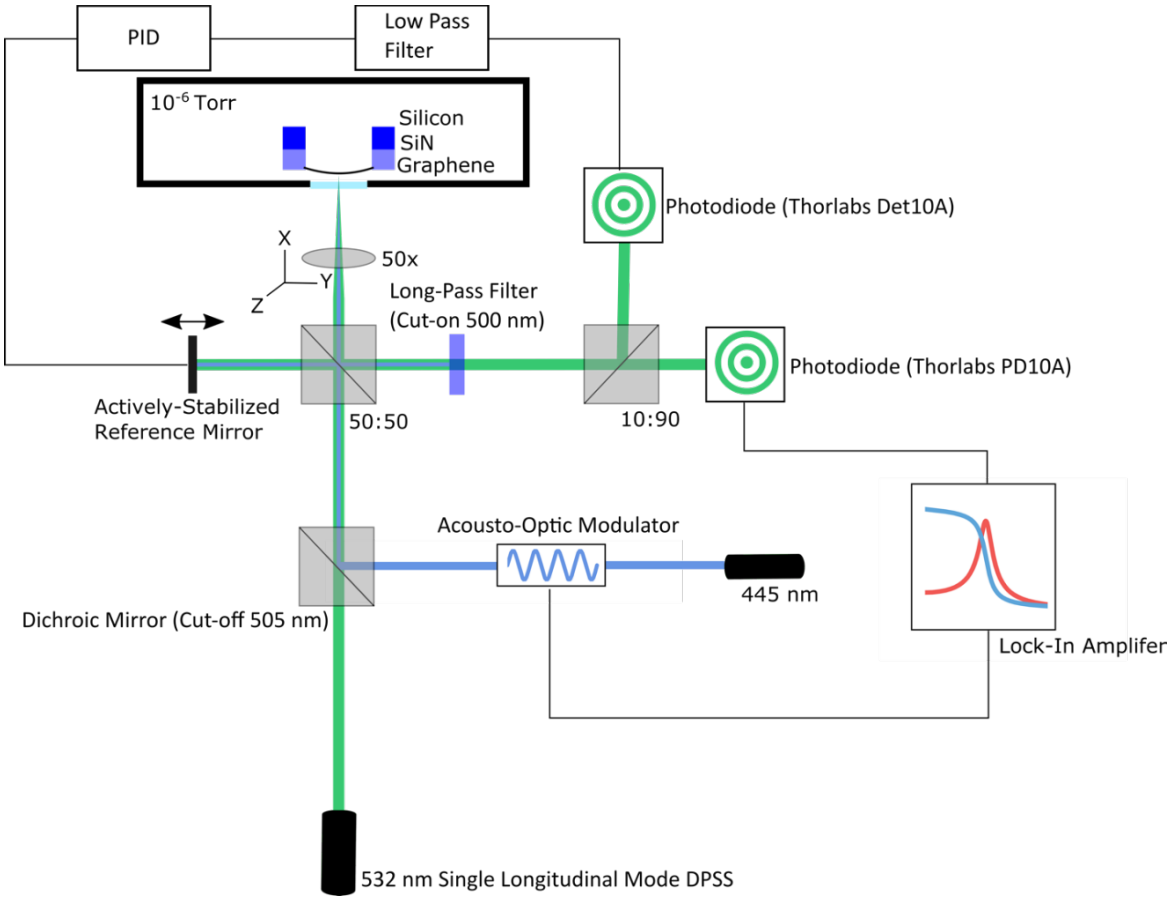

Supplementary Figure A.5: Detailed diagram of the interferometric measurement of graphene mechanical motion. An incident 532 nm single longitudinal mode laser is divided by a 50:50 beamsplitter into a signal and reference arm. Reflected light from the graphene devices and a reference mirror is interfered on two fast photodiodes using a 10:90 beamsplitter. The reflected signal is fed through a low-pass filter with a characteristic time constant much longer than the period of the mechanical resonance frequencies of the graphene devices. This filtered signal is used as the input for a PID loop. The output of the PID loop drives a piezoelectric crystal, which adjusts the length of the reference arm to compensate for low-frequency path length changes in the interferometer. The transmitted signal is measured using a lock-in amplifier to recover amplitude and phase information. A 445 nm diode laser is amplitude modulated via an acousto-optic modulator and coupled into the optical path through a dichroic mirror in order to photothermally actuate the mechanical motion. Prior to detection, the 445 nm light is filtered out by a long-pass filter.

A.1: Calculation of strain for a mechanical drumhead

We follow the calculation given in (171) to calculate the minimum strain in the graphene drumheads. The fundamental resonance frequency for a tensioned membrane is given by $f_0 = \frac{4.808}{2\pi D}\sqrt{\frac{Yt\epsilon}{\rho\alpha}}$ where D is the drumhead diameter (2.5 μm), t is the thickness (.335 nm), Yt is the in-plane Young's modulus (340 N/m), ρ is the two-dimensional mass density (7.4×10^{-16} g/μm^2), α is scaling factor to account for additional contaminant mass from the transfer process, and ϵ is the strain in the membrane. Since $\boldsymbol{\alpha}$ is unknown, typically of order 1, we set a minimum, rather than absolute, value on the strain. Using the measured resonance frequency of 21.54 MHz for the drumheads, we calculate a minimum strain of $\boldsymbol{\epsilon} \sim 10^{-5}$, which is in accord with previous measurements of graphene drumheads on holey silicon-nitride(75).

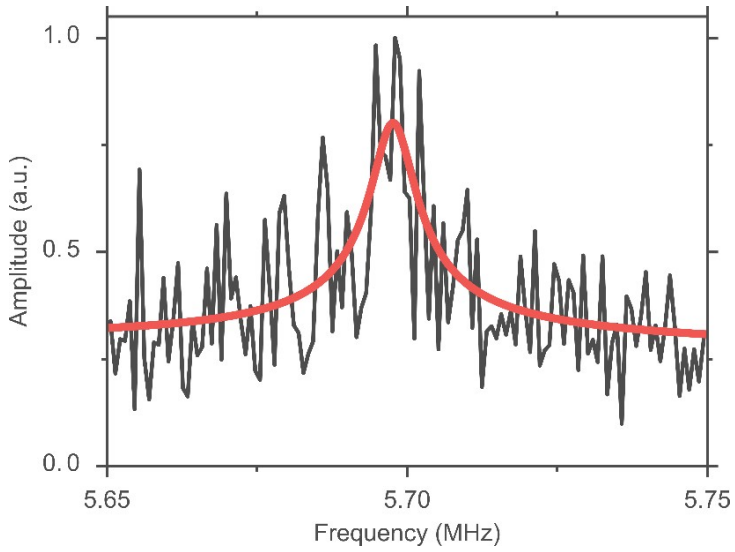

Supplementary Figure A.6: Thermomechanical noise (black) for a triangular cantilever fitted to damped harmonic oscillator fit (red). The time constant on the lock-in amplifier was set to 10 ms.

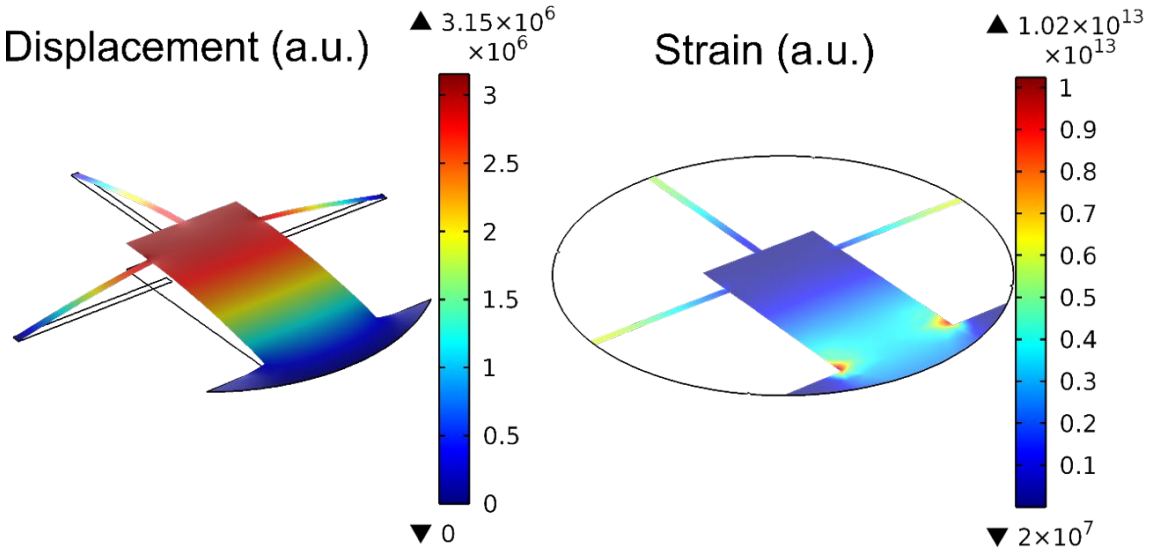

Supplementary Figure A.7: Finite element simulations of normalized displacement and strain for tethered cantilever. Regions of high strain are visible both in the base of the cantilever and at the ends of the three tethers.

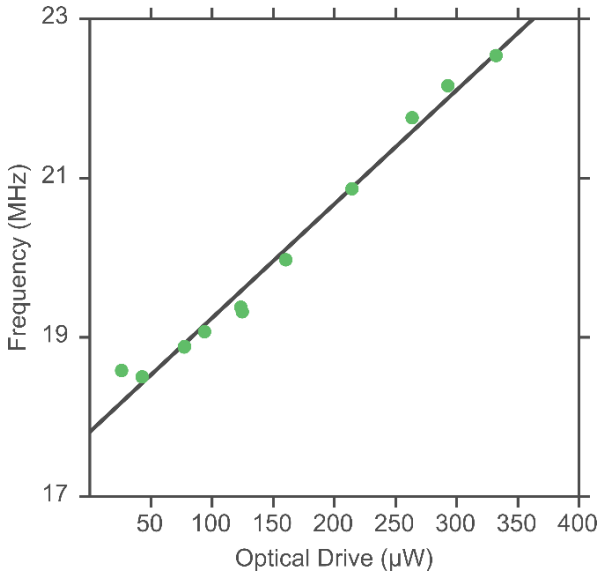

Supplementary Figure A.8: Frequency shift as a function of optical drive power. The frequency is seen to increase with increasing optical drive power. We attribute this to a combination of thermal expansion of the silicon-nitride and thermal contraction of the graphene at increased temperatures(170). The amplitude response remains linear over the entire range of optical drive power. A linear fit (black line) shows a frequency shift of 14 kHz/μW over a range of about 4 MHz.

APPENDIX B

SUPPLEMENTARY INFORMATION FOR CHAPTER VI

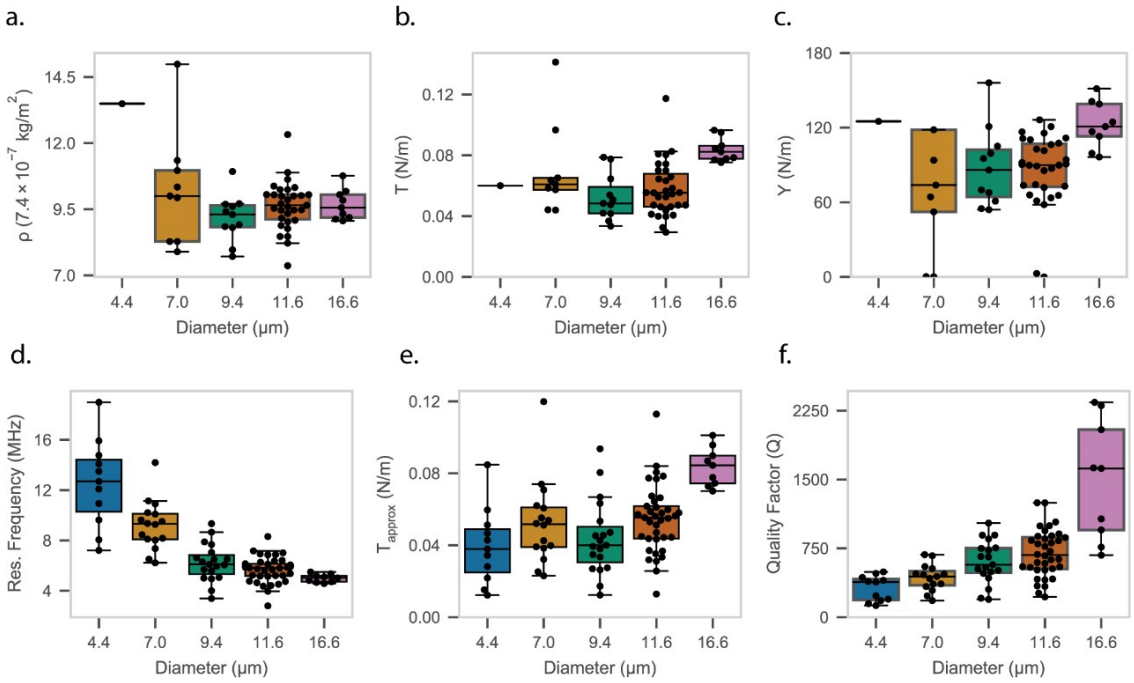

Supplementary Figure B.1: Elastic properties from 3-parameter fit and approximate value of the mass density. (a-c) Mass density, tension, and 2D modulus vs. diameter obtained directly by fitting the gate-frequency response curves. Outliers for the smaller diameter devices are likely the result of mis-fitting, rather than the true mechanical properties. The average mass density in (b) for the 11.6 μm diameter devices is $\rho_{RS:} = 9.64\rho_{:} \pm .91\rho_{:}$. (d) Resonance frequency vs. device diameter. (e) Approximate tension vs. device diameter using $f_{,}$ and $\rho_{RS:}$. This value of the tension is used throughout the main text rather than those shown in (b). (f) Q vs. device diameter.

B.1 Derivation of dilution factor for a circular membrane

The dilution factor given by $D = 1 + \frac{\cdot\cdot}{\cdot_{\#}}$ can be analytically solved for in the limit of $\lambda \gg 1$. Applying Eq. 2.21 ($\nabla^{+}\phi_{\mathbf{I}} = -\eta^{+}_{\mathbf{!}}\ \phi_{\mathbf{I}}$ and $\nabla\phi_{\ 3} = \xi^{+}_{\mathbf{!}}\phi_{\ 3}$) to the expressions for effective plate and membrane spring constants (Eq. 2.5 and Eq. 2.6), we find,

$$k_{6,344} = \frac{\kappa}{a^{+}} \int_{\$}^{+@} d\theta \int_{\$}^{8} s\,ds\ (\eta^{+}_{\mathbf{!}}\cdot\cdot\phi_{\mathbf{I}} + 2\eta^{+}_{\mathbf{!}}\cdot\cdot\xi^{=}\ \phi_{\mathbf{I}}\phi_{3} + \xi^{=}_{\mathbf{!}}\cdot\cdot\phi_{3}^{+})$$

$$k_{n,344} = T \int_0^{2\pi} d\theta \int_0^{R} sds(\eta^+_{n\cdots} \phi^+_1 + 2\ldots \xi_{n\cdots} \phi_1 \phi_3 - \xi^+_{n\cdots} \phi^+_3)$$

The solutions to the radial part of these integrals are,

$$\int_0^{R} sds\phi_1^+ = \frac{1}{2} w J_n^+[\eta_{n\cdots}] - \frac{2}{\eta_{n\cdots}} m J_{n-8}[\eta_{n\cdots}] J_n[\eta_{n\cdots}] + J_{n-8}^+[\eta_{n\cdots}] x$$

$$\int_0^{R} sds\phi_3^+ = \frac{J_n^+[\eta_{n\cdots}]}{2I_n^+[\xi_{n\cdots}]} w I_n^+[\xi_{n\cdots}] + \frac{2}{\eta_{n\cdots}} m I_{n-8}[\xi_{n\cdots}] I_n[\xi_{n\cdots}] - I_{n-8}^+[\xi_{n\cdots}] x$$

$$\int_0^{R} sds\phi_1\phi_3 = \frac{J_n[\eta_{n\cdots}]}{I_n[\xi_{n\cdots}]} \frac{1}{\xi_{n\cdots}^+ + \eta_{n\cdots}^+} (\xi_{n\cdots} J_n[\eta_{n\cdots}] I_{n+8}[\xi_{n\cdots}] + \eta_{n\cdots} J_{n+8}[\eta_{n\cdots}] I_n[\xi_{n\cdots}])$$

These expressions can be simplified using several approximations. First, using Eq. 2.30, $\int_0^{R} sds\phi_1\phi_3 = 0$. Next, we look in the membrane limit where $\lambda \ll 1$. This allows us to write $\xi_{n\cdots} = 1/\lambda$, $\eta_{n\cdots} = \alpha_{n\cdots}$, $\frac{\alpha J_{n+8}[\alpha]}{J_n[\alpha]} \approx 1$, $\alpha_{n\cdots}\lambda J_{n+8}[\alpha_{n\cdots}] = -J_n[\alpha_{n\cdots}]$, and $J_n[\alpha_{n\cdots}] \approx 0$.

This means,

$$\int_0^{R} sds\phi_1 \approx \frac{1}{2} J_{n-8}^+[\alpha_{n\cdots}]$$

Finally, using the asymptotic approximation of $I_n[\beta] \approx \frac{e^{\beta}}{\sqrt{2\pi\beta}}\left(1 - \lambda\frac{n^2-8}{2\beta}\right)$ and keeping only the leading order of λ, we find,

$$\int_0^{R} sds\phi_3 = \frac{1}{2}\alpha_{n\cdots}\lambda\, J_{n+8}^+[\alpha_{n\cdots}]$$

Thus,

$$\frac{k_n}{k_0} = \frac{1}{\lambda^+} \frac{\alpha_{n\cdots}^+ J_{n-8}^+[\alpha_{n\cdots}] - \alpha_{n\cdots}^+ \lambda J_{n+8}^+[\alpha_{n\cdots}]}{\alpha_{n\cdots}^= J_{n-8}^+[\alpha_{n\cdots}] + \frac{\alpha_{n\cdots}^2}{\lambda} J_{n+8}^+[\alpha_{n\cdots}]}$$

Using the identity,

$$nJ_{n\cdots}(\alpha_{n\cdots}) = \frac{1}{2}\alpha_{n\cdots}\left[J_{n-8}(\alpha_{n\cdots}) + J_{n+8}(\alpha_{n\cdots})\right] \approx 0$$

We find,

$$D_{\#} = 1 + \frac{k_n}{k_0} = \frac{1}{\lambda}\frac{1-\lambda}{(\alpha_n^+\lambda + 1)} = \frac{1 + \alpha_{n\cdots}^+\lambda^+}{\lambda^+\alpha_n^+ + \lambda}$$

For very small λ,

$$D_{\#} = \frac{1}{\lambda(1 + \alpha_{\mathbf{I}}^{\dagger}\lambda)}$$

APPENDIX C

SUPPLEMENTARY INFORMATION FOR CHAPTER VII

From Miller, D. & Alemán, B. Spatially resolved optical excitation of mechanical modes in graphene NEMS. *Appl. Phys. Lett.* **115**, 193102 (2019).

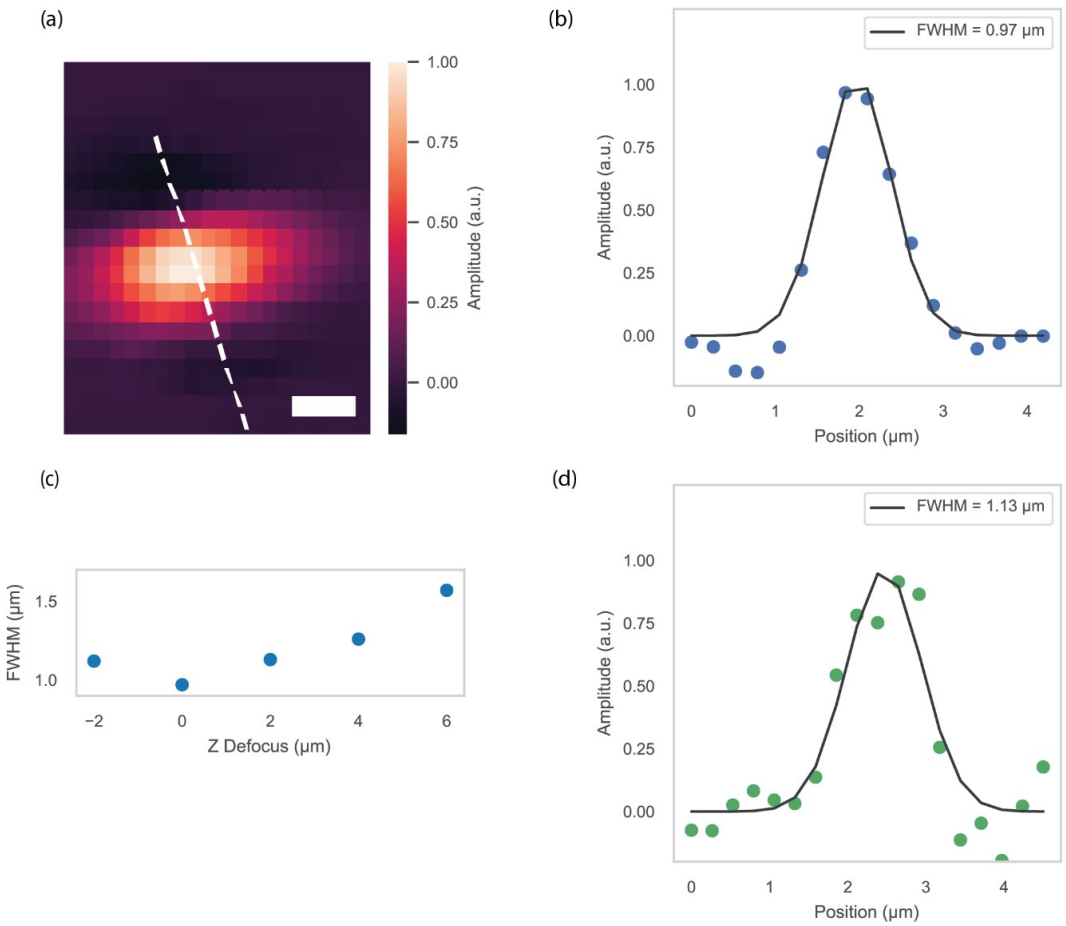

Supplementary Figure C.1**:** Measurement of laser FWHM at sample plane. The probe and drive laser were modulated at 1 kHz and 100 kHz respectively and reflected off of the substrate before being sent directly into the photodiode. The voltage signal was demodulated by a lock-in amplifier to give the reflected laser amplitude. By scanning both lasers across the 300 nm wide knife-edge venting trenches in the substrate, the Gaussian FWHM can be estimated. (a) Amplitude of the reflected drive laser as it is scanned across a trench. Increased scattering when the laser is on the trench leads to a reduced amplitude measured at the photodiode. Imperfect coupling of the 445 nm light into the photodiode leads to the elliptical shape in the image. (Scale = 1 μm). (b) Gaussian fit to the line cut indicated by the white-dashed line in a. The fit gives a FWHM of 0.97 μm. (c) FWHM as a function of laser defocus. As the laser is defocused, the FWHM measured through this knife-edge method increases. All measurements in the main text took place within a focus range of −2 μm to 2 μm. (d) Gaussian fit to the line-cut while scanning the probe laser over a trench. The FWHM in this case is 1.13 μm.

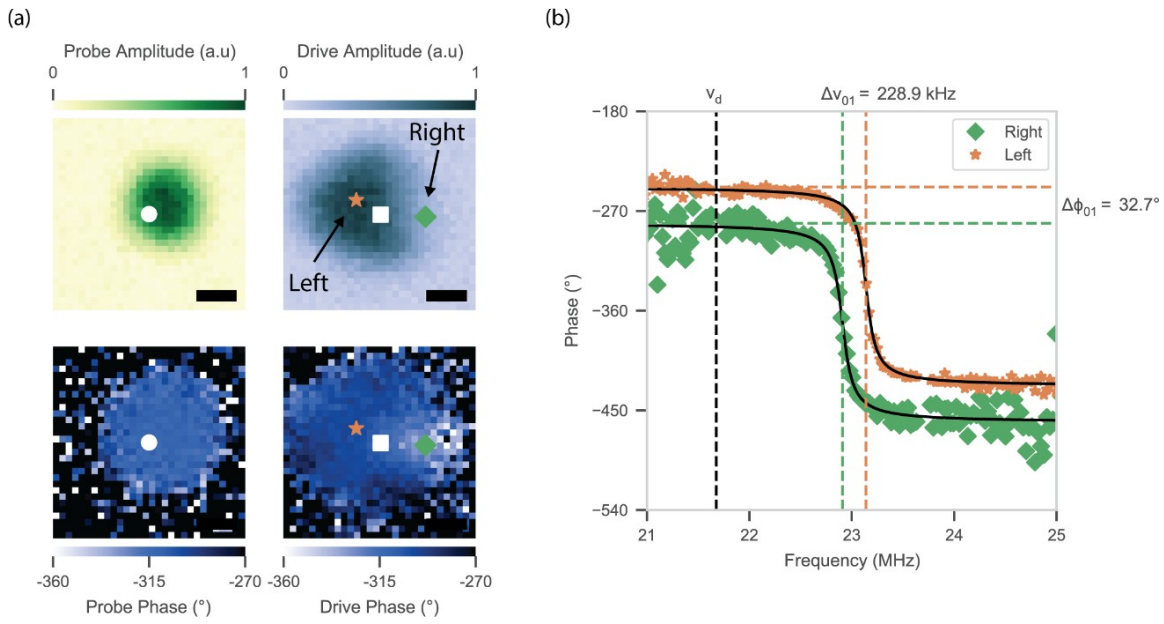

Supplementary Figure C.2 Spatial dependence of the phase. (a) Probe and force maps for the fundamental mode of a 3 μm diameter drumhead. A spatially varying phase similar to those shown in the main text is visible in the force maps. (b) Phase-response spectra from two points on the drumhead, indicated by the orange star and green diamond in the force map. The off-resonance drive frequency is shown by the black vertical dashed line. The deviation in phase between the two spots is measured at 31.4°, in accord with what is seen on the force map. We find that although $\nu_{,-}$ varies by 231.9 kHz between the two spots, presumably due to thermal tensioning, it cannot explain the observed phase variation seen in the force map. This furthers our claim that the reported phase variations in the main text are due to a spatially varying phase response, rather than an artifact due to the resonance frequency shifting.

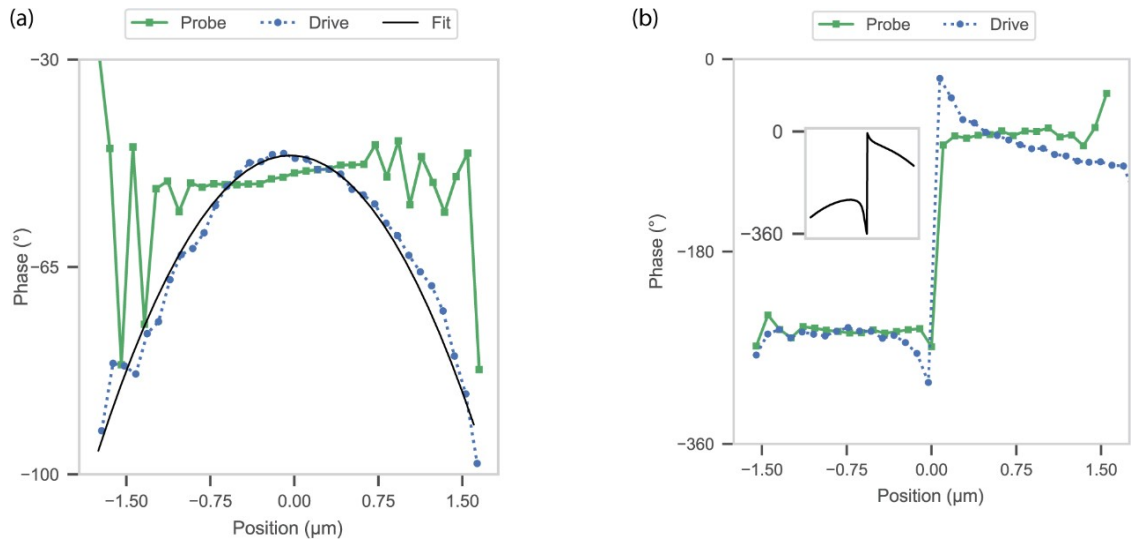

Supplementary Figure C.3: Cross-sections of the phase for (a) $U_{,-}$ (b) and $U_{--^{G}}$.

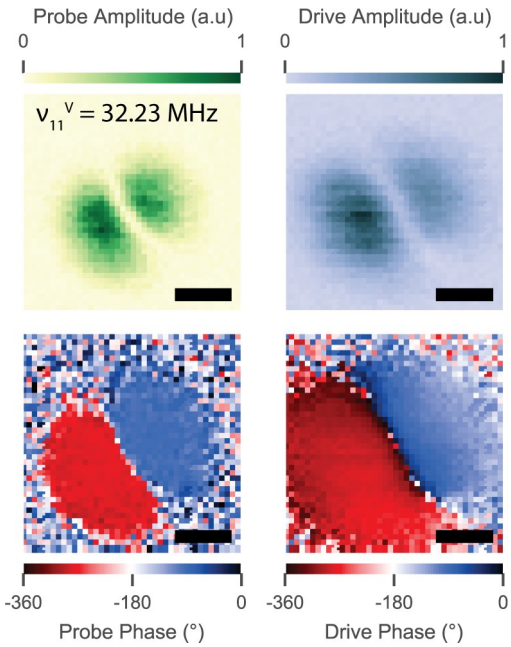

Supplementary Figure C.4: Mode and force maps for the $U_{!!}$" mode. $\nu_{\#} = 31.50$ MHz. (scale = 1 micron).

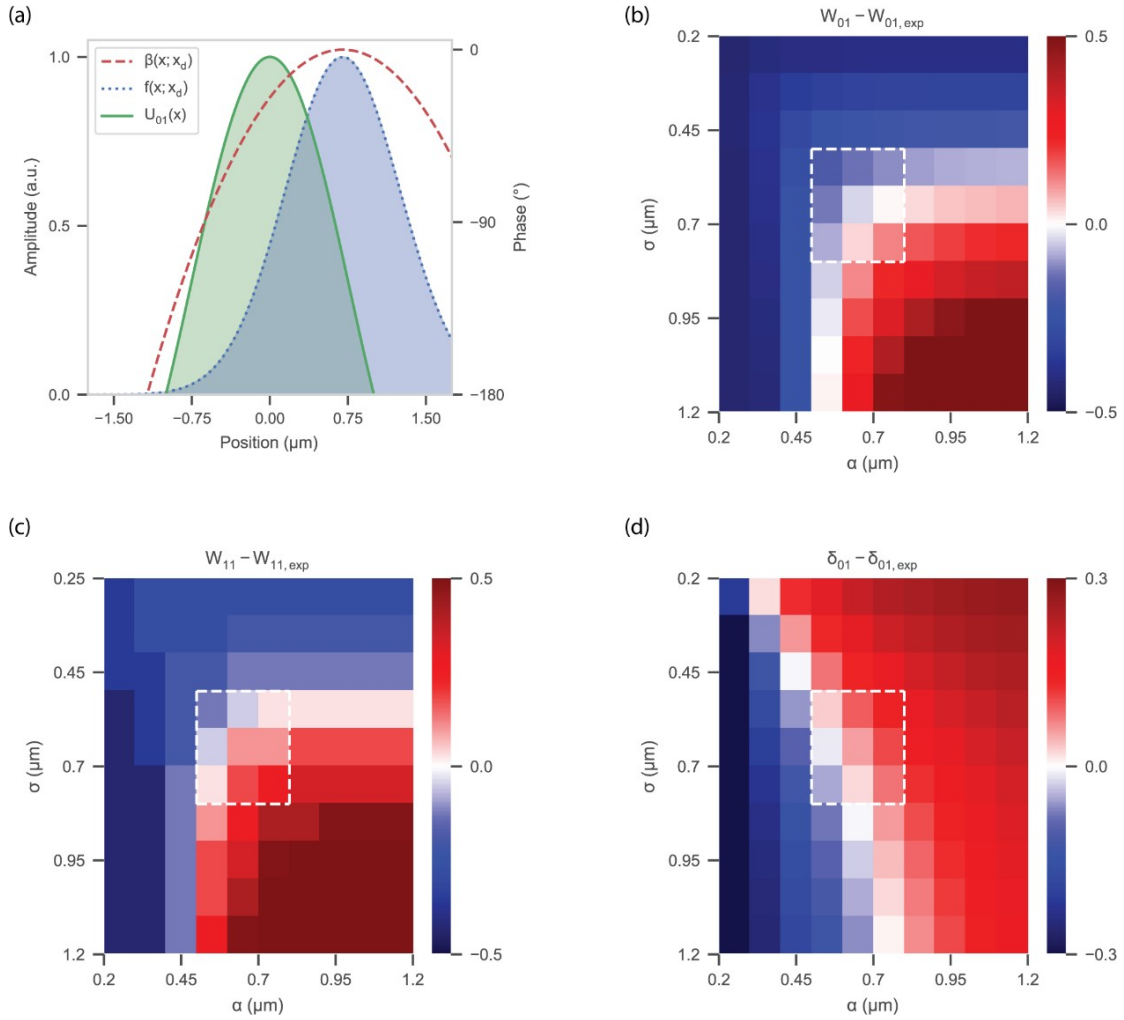

Supplementary Figure C.5: Dependence of $W_{,-}$, W_{--}, and $\delta_{,-}$ as function of σ and α. Combing the results from $U_{,-}$ and U_{--}, we generally find that our experimental data is consistent with values of σ and α between .55 μm and .75 μm, indicated by the dashed box. (a) Cross-section in the x-axis with $y_F = 0$ of the overlap integrals we numerically evaluate in this work, with a mode diameter of 2 μm, $\sigma = .55$ μm, $\alpha = .75$ μm, and $x_F = .7$ μm. (b.) Heatmap showing the experimentally measured $W_{,-}$ subtracted from the numerically evaluated $W_{,-}$, at various values of σ and α. (c.) Heatmap showing the experimentally measured W_{--} subtracted from the numerically evaluated W_{--}, at various values of σ and α. (d.) Heatmap showing the experimentally measured $\delta_{,-}$ subtracted from the numerically evaluated $\delta_{,-}$, at various values of σ and α.

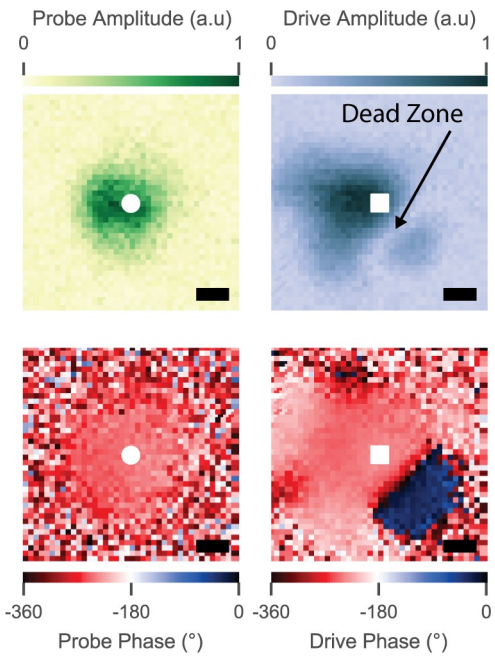

Supplementary Figure C.6: Mode and force maps for the $U_{,-}$ mode of a 5 μm diameter device. Although the mode map is symmetric and consistent with theoretical predictions, the force map is more complex unlike those shown in the main text. We see significant variation in the phase and amplitude response of the device in the force map and observe a "dead-zone", where the drive force disappears and a 180° phase change occurs, much like crossing a nodal line. (Scale = 1 micron).

APPENDIX D

SUPPLEMENTARY INFORMATION FOR CHAPTER VIII

From Miller, D. Blaikie, A., and Alemán, B., Non-volatile rewritable frequency tuning of a nanoelectromechanical resonator using photoinduced doping, *Nano Lett.* **20**, 2378-2386, (2020).

D.1 Methods

Fabrication of 2D drumheads:

gr/hBN mechanical drumhead resonators were fabricated by transferring the 2D sheets over an array of cavities etched into 1 μm wet thermal oxide(20) grown on degenerately doped silicon wafers (University Wafer). The cavities were fabricated using direct-write optical lithography and CHF_3 based reactive ion etching. A ~300 nm layer of oxide was left at the bottom of the cavity to act as a charge trapping layer and to prevent shorting. Ti/Pt electrodes were defined by lithography and deposited by electron-beam evaporation.

To prepare the 2D sheets for transfer, a relatively thick layer (~3 μm) of PMMA A11 was spun onto CVD grown single-layer hBN on Cu foil (Graphene Supermarket) and then a polyamide scaffold with a central hole removed was then placed on the PMMA/hBN/Cu stack. The stack was placed in a bath of Ammonium Persulphate to etch the Cu and then rinsed in deionized water and dried in air. The polyamide/PMMA/hBN was placed on top of CVD graphene grown on Cu foil (Graphenea) and baked at 180 °C for 30 minutes to adhere the hBN and the graphene(61, 79). The etching, rinsing, and drying was repeated leaving a freestanding film of PMMA/hBN/Graphene supported by the polyamide scaffold. To transfer the 2D sheets to the cavity substrates, the PMMA/hBN/Graphene stack was then placed graphene-side-down on top of the pre-patterned cavities and adhered at 155 °C overnight (~15 hours). After removing the polyamide scaffold, the PMMA was removed in flowing Ar/H_2 at 400 °C. The graphene sheet contacts the electrodes from above, resulting in a simultaneous electrical connection to all devices. Graphene-only

devices were fabricated in a similar fashion with both an in-house and a commercial transfer process performed by Graphenea.

Measurement of mechanical motion:

Device motion was measured using optical interferometry, as described previously(71). A 633 nm HeNe laser was focused onto the devices (held at room temperature at 10^{-} torr) using a 40 ×, 0.6 NA objective. The reflected light was detected using a high-sensitivity photodiode and the voltage signal was demodulated using a Zurich Instruments HFLI2 Lock-In amplifier. The incident laser was scanned with a two-axis galvometer and passed through an optical relay system in order to image the mode shape and to maximize transduction sensitivity. We used a low laser power (~1 – 10 μW) to avoid unwanted photodoping by the 633 nm probe laser.

Photodoping:

A separate laser (405 nm, 445 nm, or 532 nm) was used for photodoping. The doping laser was coupled into the beam-path using a dichroic mirror and focused onto the sample using the same 40 ×, 0.6 NA objective lens. A separate two-axis galvometer was used to position the doping laser at the center of the drumheads. The laser power for each color was calibrated using a power meter and maintained using PID control. For dynamic measurements of $V_{!\&TU}$, an acousto-optic modulator was used to supply a well-defined pulse of the doping laser with pulse-widths down to ~10 ns. Prior to all measurements, the doping laser was scanned across the device with $V_{>} = 0$ V to guarantee a uniformly doped initial erased state.

D.2 Measurement of the CNP

Measurement of the mechanical charge neutrality point ($V_{!\&TU}$) has typically been accomplished in previous work by fitting the full frequency tuning curves (such as those shown in Figure 2a), but this approach is too slow for a dynamic measurement of $V_{!\&TU}$. To overcome this, we use a mechanical feedback approach, similar to Kelvin Force Probe Microscopy(169, 171), to rapidly measure $V_{!\&TU}$. The electrostatic force felt by the membrane is:

$$F \approx \frac{1}{2}\frac{dC_S}{dx}\left(V_S - V_{!\&TU}\right)^2 + V_{/\&}\frac{dC_S}{dx}\left(V_S - V_{!\&TU}\right)\cos(2\pi f t + \theta) \qquad \text{(D. 1)}$$

where the first term leads to frequency tuning and the second to electrostatic driving. We use the off-resonant behavior of the second term to measure $V_{!\&TU}$. For low frequencies below both the RC time constant of the electromechanical circuit ($\sim$ 1 μs) and the mechanical resonance frequency ($\sim$0.1 μs), the phase θ will vanish. In this regime, the X-quadrature ($X_{çéI>}$) amplitude measured by the lock-in amplifier is proportional to ($V_S - V_{!\&TU}$), which vanishes when $V_S = V_{!\&TU}$. Thus to measure $V_{!\&TU}$, we feedback on $X_{çéI>}$ with a set point voltage $X_{çéI>} = 0$ V and use V_S as the output variable. The value of V_S that makes $X_{çéI>}$ vanish is equal to $V_{!\&TU}$.

For the dynamic measurements such as those shown in Figure 4, our protocol is as follows. First, we set the drive frequency to $f = 100$ kHz, which is well below the mechanical resonance frequencies of $\sim$10 MHz and turn on the mechanical feedback. After a brief stabilization period, V_S is measured 10 times with the average value taken as $V_{!\&TU}$. V_S is then fixed at $V_>$ and a photodoping optical pulse with a predetermined width (from as low as a few milliseconds to several seconds) is applied to the device. This process is repeated until $V_{!\&TU}$ approaches $V_>$ with both the laser power and pulse time determining the total length of the measurement, which can take several minutes depending on the resolution.

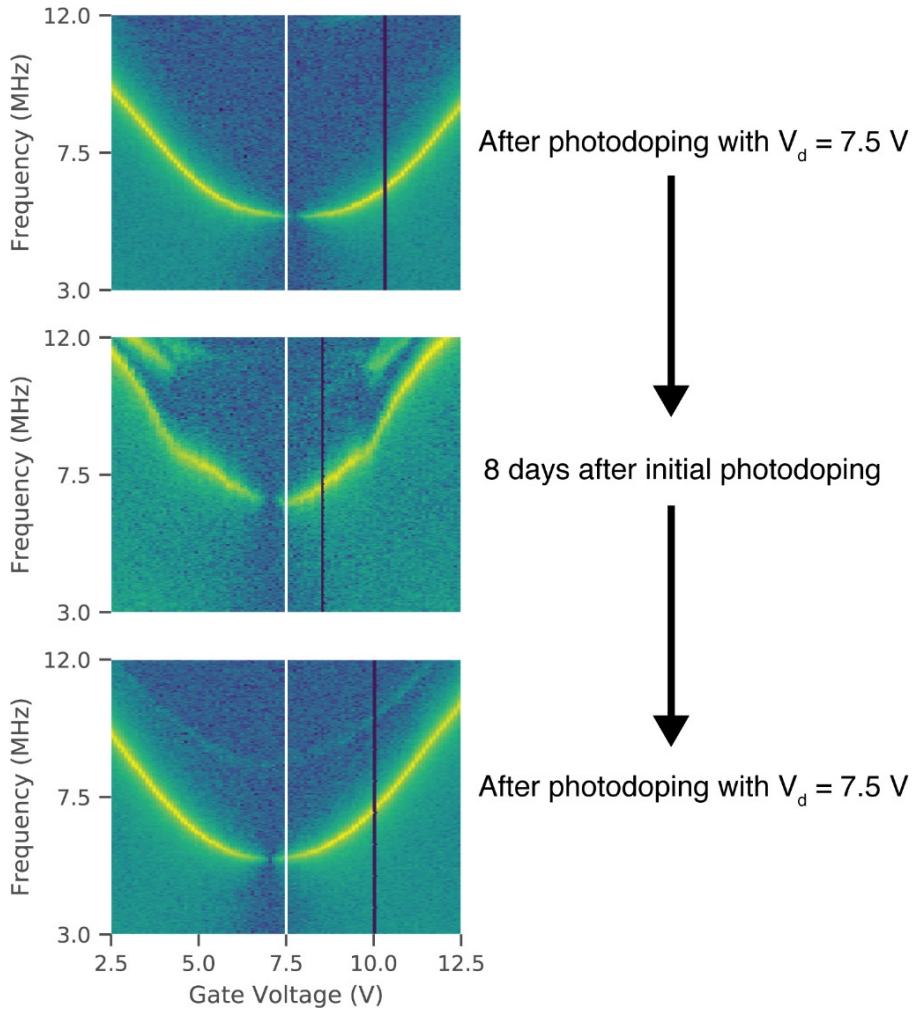

Supplementary Figure D.1: Top: Electrostatic frequency tuning spectra of a gr/hBN device immediately after phototuning with $V_F = 7.5\ V$ (indicated by white line) Middle: Electrostatic frequency tuning spectra of the same device after being left in the dark for 8 days with no bias applied. Significant changes to the tuning spectra are apparent. Bottom: Electrostatic frequency tuning spectra of a gr/hBN device after an additional phototuning step with $V_F = 7.5\ V$. The prisitine tuning spectra is recovered. The dark blue lines correspond to missing data due to a software error.

D.3 Calculation of the photodoping rate

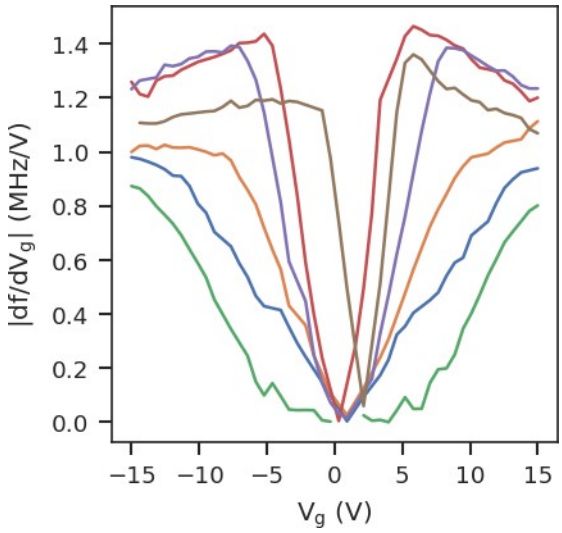

Supplementary Figure D.2: Derivative of the electrostatic frequency tuning curve with respect to the gate voltage for 6 gr/hBN devices. For larger gate voltage values of, $\frac{\text{FN}}{\text{FK\#}}$ is between 0.8 MHz/V and 1.4 MHz/V.

Here, we calculate the temporal frequency tuning rate $\frac{\geq 4\text{Q}}{>\text{R}}$ of our phototuning method. The tuning rate characterizes how quickly a device can be tuned to a new frequency, or equivalently, how many devices can be tuned within a given amount of time. To obtain the tuning rate, we first determine the time required to move $V_{!\&TU}$ by an amount $\Delta V_{!\&TU}$. Substituting the expression $E = P \times$ t into Eq. 1 of the main text gives the time-dependence of the $V_{!\&TU}$ at fixed power P:

$$V_{!\&TU}(t) = \Delta V(1 - e^{-\text{ÄUR}}) + V_{\$} \qquad \text{(D. 2)}$$

If a device is phototuned for a time Δt, then the corresponding change in the $V_{!\&TU}$ will be

$$\Delta V_{!\&TU} \approx \frac{dV_{!\&TU}}{dt}\Delta t = \alpha P \Delta V e^{-\text{ÄUR}}\Delta t \qquad \text{(D. 3)}$$

At the very start of phototuning (*i.e.* at $t = 0$), the shift in $V_{!\&TU}$ is $\Delta V_{!\&TU} = \alpha P \Delta V \Delta t$. Recalling that $V_{344} = V_{S} - V_{!\&TU}$ and defining $f \equiv f_{\$} + \Delta f_{\$}(V_{344})$, the $\Delta V_{!\&TU}$ will shift the entire gate spectrum $fyV_{S}z$ and, thus, will shift the phototuned frequency $f_{|}$

(recall, $f_{|} \equiv fyV_{S} = 0z$). An example of $fyV_{S}z$ is shown Figure 5c of the main text; we extract $f(V_{S})$ curves from the maximum amplitude of gate spectra of the fundamental mode (Figure 2a). The change in the phototuned frequency $f_{|}$ due to $\Delta V_{!\&TU}$ is then,

$$\Delta f_{|} = o\frac{df yV_{S}z}{dV_{S}}p_{|_{L}\ddot{O}\$} \Delta V_{!\&TU} \quad (D.\ 4)$$

or $\not{f}_{|} = {}_{W}\frac{>4\grave{e}|_{L}\hat{e}}{>|_{L}}x_{|_{L}\ddot{O}\$} \alpha P \Delta V \Delta t$. We plot experimental data for $\frac{>4\grave{e}|_{L}\hat{e}}{>|_{L}}$ for $\blacklozenge_{!\&TU} \sim 0$ V in Figure S4. For all devices tested in this work, the derivative $\frac{>4\grave{e}|_{L}\hat{e}}{>|_{L}}$ vanishes at the mechanical charge neutrality point (*i.e.* ${}_{W}\frac{>4\grave{e}|_{L}\hat{e}}{>|_{L}}x_{|_{L}\ddot{O}|\cdot WXY} = 0$) and reaches a maximum between $ºV_{344}º = ºV_{S} - V_{!\&TU}º \sim 5 - 15$ V, which varies between devices and is $\frac{>4\grave{e}|_{L}\hat{e}}{>|_{L}} \sim 0.8 - 1.4$ MHz/V, as seen in Figure 5c and Figure S4. This means that maximum values of $\Delta f_{|}$ can be achieved when $V_{!\&TU}$ is initially set such that $\frac{>4\grave{e}|_{L}\hat{e}}{>|_{L}}$ is a maximum, for example, when $V_{!\&TU}$ is set between $5 - 15\ V$ for the devices in Figure S4.

In the limit of $\Delta t \to dt$, we obtain an expression for the temporal frequency tuning rate,

$$\frac{df_{|}}{dt} = \alpha P \Delta V\ o\frac{df}{dV_{S}}p_{|_{L}\ddot{O}\$} \quad (D.\ 5)$$

The maximum temporal frequency tuning rate is

$$R_{4} \equiv \alpha P \Delta V\ \max\frac{df}{dV_{S}} \quad (D.\ 6)$$

As discussed in main text, the tuning rate varies with illumination wavelength, laser power, and device type (gr/hBN vs. graphene devices).

The tuning rate R_{4} can reach large values that make it possible to tune thousands of devices in less than a second. For a typical gr/hBN device, $\alpha P \sim 50\ s^{-1}$ and $\max\frac{>4}{>|_{L}} \sim 1$ MHz/V. The value of ΔV can be set arbitrarily high, up to the damage threshold or

dielectric breakdown voltage of our devices. In our studies, we set ΔV as high as ~35 V, which corresponds to a tuning rate of $R_4 = 1.75$ GHz/s.

Using R_4 we can calculate the time required to tune a device. A relevant amount of frequency tuning for a device is the resonance linewidth of a membrane, which is of order $\Delta f_{Ü}$~100 kHz. The time required to tune by one linewidth is

$$\tau = \frac{\Delta f_{Ü}}{R_4} \tag{D. 7}$$

With $R_4 = 1$ GHz/s, we obtain $\tau = 100$ μs. This same tuning rate could tune 10,000 devices by a 100 kHz linewidth in one second.

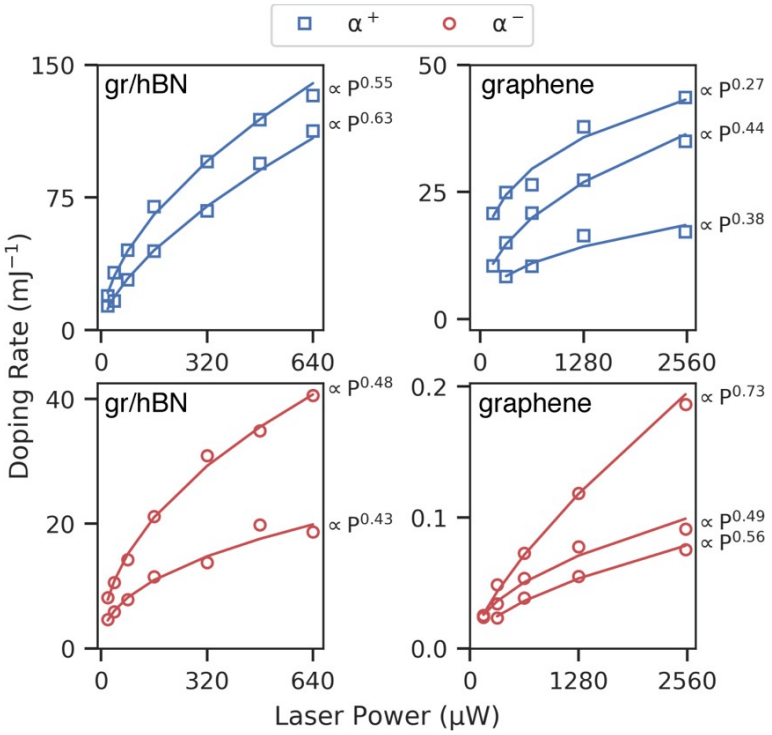

Supplementary Figure D.3: Complete power dependence curves for the α^+ and α^- branch for two gr/hBN devices and three graphene devices with the corresponding exponent for the incident power. This exponent is consistently around 0.5.

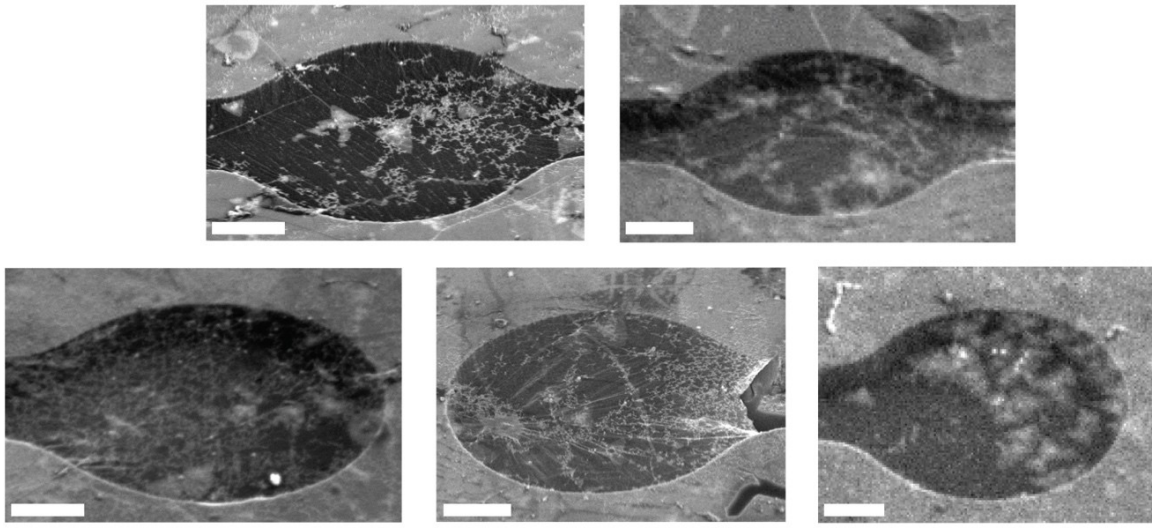

Supplementary Figure D.4: Gallery of gr/hBN devices used in Figure 5(b-c). Various levels of imperfections, defects, and clamping are observed across the devices. Scale = 1 μm.

REFERENCES CITED

1. T. Freeth, A. Jones, J. M. Steele, Y. Bitsakis, Calendars with Olympiad display and eclipse prediction on the Antikythera mechanism. *Nature* **454**, 614–617 (2008).

2. A. G. Bromley, Charles Babbage's Analytical Engine, 1838. *IEEE Ann. Hist. Comput.* **20**, 29–45 (1998).

3. A. Einstein, W. J. de Haas, Experimental proof of the existence of Ampère's molecular currents. *K. Akad. van Wet. te Amsterdam, Proc.* **18**, 696–711 (1915).

4. J. Weber, Gravitational radiation. *Phys. Rev. Lett.* **18**, 498–501 (1967).

5. M. S. Hanay, *et al.*, Inertial imaging with nanomechanical systems. *Nat. Nanotechnol.* **10**, 339–344 (2015).

6. M. Nonnenmacher, M. P. O'Boyle, H. K. Wickramasinghe, Kelvin probe force microscopy. *Appl. Phys. Lett.* **58**, 2921–2923 (1991).

7. H. Okamoto, *et al.*, Coherent phonon manipulation in coupled mechanical resonators. *Nat. Phys.* **9**, 480–484 (2013).

8. A. D. O'Connell, *et al.*, Quantum ground state and single-phonon control of a mechanical resonator. *Nature* **464**, 697–703 (2010).

9. J. Schmöle, M. Dragosits, H. Hepach, M. Aspelmeyer, A micromechanical proof-of-principle experiment for measuring the gravitational force of milligram masses. *Class. Quantum Gravity* **33**, 125031 (2016).

10. Z. Zhou, Z. Wang, L. Lin, *Microsystems and Nanotechnology*, Z. Zhou, Z. Wang, L. Lin, Eds. (Springer Berlin Heidelberg, 2012).

11. H. C. Nathanson, W. E. Newell, R. A. Wickstrom, J. R. Davis, The resonant gate transistor. *IEEE Trans. Electron Devices* **14**, 117–133 (1967).

12. G. Binnig, C. F. Quate, C. Gerber, Atomic Force Microscope. *Phys. Rev. Lett.* **56**, 930–933 (1986).

13. M. Guthold, *et al.*, Following the assembly of RNA polymerase-DNA complexes in aqueous solutions with the scanning force microscope. *Proc. Natl. Acad. Sci. U. S. A.* **91**, 12927–12931 (1994).

14. S. Schmid, L. G. Villanueva, M. L. Roukes, *Fundamentals of Nanomechanical Resonators* (Springer International Publishing, 2016) https:/doi.org/10.1007/978-3-319-28691-4.

15. K. L. Ekinci, M. L. Roukes, Nanoelectromechanical systems. *Rev. Sci. Instrum.* **76**, 061101 (2005).

16. J. D. Teufel, *et al.*, Sideband Cooling Micromechanical Motion to the Quantum Ground State. *Nature* **475**, 359–363 (2011).

17. K. Jensen, K. Kim, A. Zettl, An atomic-resolution nanomechanical mass sensor. *Nat. Nanotechnol.* **3**, 533–537 (2008).

18. C. L. Degen, M. Poggio, H. J. Mamin, C. T. Rettner, D. Rugar, Nanoscale magnetic resonance imaging. *Proc Natl Acad Sci U S A* **106**, 1313–1317 (2009).

19. V. Sazonova, *et al.*, A tunable carbon nanotube electromechanical oscillator. *Nature* **431**, 284–7 (2004).

20. J. S. Bunch, *et al.*, Electromechanical Resonators from Graphene Sheets. *Science* **315**, 490–493 (2007).

21. M. L. Roukes, Mechanical compution, redux? in *IEDM Technical Digest. IEEE International Electron Devices Meeting, 2004.*, (IEEE, 2004), pp. 539–542.

22. S. Dominguez-Medina, *et al.*, Neutral mass spectrometry of virus capsids above 100 megadaltons with nanomechanical resonators. *Science* **362**, 918–922 (2018).

23. A. Rogalski, Next decade in infrared detectors in *Electro-Optical and Infrared Systems: Technology and Applications XIV*, D. A. Huckridge, R. Ebert, H. Bürsing, Eds. (SPIE, 2017), p. 100.

24. X. C. Zhang, E. B. Myers, J. E. Sader, M. L. Roukes, Nanomechanical torsional resonators for frequency-shift infrared thermal sensing. *Nano Lett.* **13**, 1528–1534 (2013).

25. M. H. Matheny, *et al.*, Exotic states in a simple network of nanoelectromechanical oscillators. *Science* **363**, eaav7932 (2019).

26. F. Varela, J. P. Lachaux, E. Rodriguez, J. Martinerie, The brainweb: Phase synchronization and large-scale integration. *Nat. Rev. Neurosci.* **2**, 229–239 (2001).

27. E. Sage, *et al.*, Single-particle mass spectrometry with arrays of frequency-addressed nanomechanical resonators. *Nat. Commun.* **9**, 3283 (2018).

28. H. Arjmandi-Tash, A. Allain, Z. (Vitto) Han, V. Bouchiat, Large scale integration of CVD-graphene based NEMS with narrow distribution of resonance parameters. *2D Mater.* **4**, 025023 (2017).

29. R. De Alba, *et al.*, Tunable phonon-cavity coupling in graphene membranes. *Nat. Nanotechnol.* **11**, 741–746 (2016).

30. R. Fischer, *et al.*, Spin detection with a micromechanical trampoline: Towards magnetic resonance microscopy harnessing cavity optomechanics. *New J. Phys.* **21** (2019).

31. A. N. Cleland, M. L. Roukes, A nanometre-scale mechanical electrometer. *Nature* **392**, 160–162 (1998).

32. S. Olcum, N. Cermak, S. C. Wasserman, S. R. Manalis, High-speed multiple-mode mass-sensing resolves dynamic nanoscale mass distributions. *Nat. Commun.* **6**, 7070 (2015).

33. J. Chaste, *et al.*, A nanomechanical mass sensor with yoctogram resolution. *Nat. Nanotechnol.* **7**, 301–304 (2012).

34. A. H. Ghadimi, *et al.*, Elastic strain engineering for ultralow mechanical dissipation. *Science* **6939**, 764–768 (2018).

35. R. A. Norte, J. P. Moura, S. Gröblacher, Mechanical Resonators for Quantum Optomechanics Experiments at Room Temperature. *Phys. Rev. Lett.* **116**, 147202 (2016).

36. M. Imboden, P. Mohanty, Dissipation in nanoelectromechanical systems. *Phys. Rep.* **534**, 89–146 (2014).

37. S. S. Verbridge, J. M. Parpia, R. B. Reichenbach, L. M. Bellan, H. G. Craighead, High quality factor resonance at room temperature with nanostrings under high tensile stress. *J. Appl. Phys.* **99** (2006).

38. S. Schmid, K. D. Jensen, K. H. Nielsen, A. Boisen, Damping mechanisms in high-Q micro and nanomechanical string resonators. *Phys. Rev. B - Condens. Matter Mater. Phys.* **84**, 1–6 (2011).

39. S. A. Fedorov, *et al.*, Generalized dissipation dilution in strained mechanical resonators. *Phys. Rev. B* **99**, 054107 (2019).

40. Y. Tsaturyan, A. Barg, E. S. Polzik, A. Schliesser, Ultracoherent nanomechanical resonators via soft clamping and dissipation dilution. *Nat. Nanotechnol.* **12**, 776–783 (2017).

41. C. Reinhardt, T. Müller, A. Bourassa, J. C. Sankey, Ultralow-Noise SiN Trampoline Resonators for Sensing and Optomechanics. *Phys. Rev. X* **6**, 021001 (2016).

42. M. Rossi, D. Mason, J. Chen, Y. Tsaturyan, A. Schliesser, Measurement-based quantum control of mechanical motion. *Nature* **563**, 53–58 (2018).

43. K. S. Novoselov, Electric Field Effect in Atomically Thin Carbon Films. *Science* **306**, 666–669 (2004).

44. P. L. Yu, T. P. Purdy, C. A. Regal, Control of material damping in High-Q membrane microresonators. *Phys. Rev. Lett.* **108**, 1–5 (2012).

45. D. Yoon, Y.-W. Son, H. Cheong, Negative thermal expansion coefficient of graphene measured by Raman spectroscopy. *Nano Lett.* **11**, 3227–31 (2011).

46. A. Blaikie, D. Miller, B. J. Alemán, A fast and sensitive room-temperature graphene nanomechanical bolometer. *Nat. Commun.* **10**, 4726 (2019).

47. R. J. Dolleman, *et al.*, Optomechanics for thermal characterization of suspended graphene. *Phys. Rev. B* **96**, 165421 (2017).

48. R. A. Barton, *et al.*, Photothermal self-oscillation and laser cooling of graphene optomechanical systems. *Nano Lett.* **12**, 4681–4686 (2012).

49. D. Akinwande, *et al.*, A review on mechanics and mechanical properties of 2D materials — Graphene and beyond. *Extrem. Mech. Lett.* **13**, 42–77 (2017).

50. R. R. Nair, *et al.*, Fine Structure Constant Defines Visual Transparency of Graphene. *Science* **320**, 1308–1308 (2008).

51. J. S. Bunch, *et al.*, Electromechanical Resonators from Graphene Sheets. *Science* **315**, 490–493 (2007).

52. Q. P. Unterreithmeier, E. M. Weig, J. P. Kotthaus, Universal transduction scheme for nanomechanical systems based on dielectric forces. *Nature* **458**, 1001–1004 (2009).

53. X. Li, *et al.*, Large-area synthesis of high-quality and uniform graphene films on copper foils. *Science* **324**, 1312–1314 (2009).

54. A. M. van der Zande, *et al.*, Large-Scale Arrays of Single-Layer Graphene Resonators. *Nano Lett.* **10**, 4869–4873 (2010).

55. P. Weber, J. Güttinger, I. Tsioutsios, D. E. Chang, A. Bachtold, Coupling Graphene Mechanical Resonators to Superconducting Microwave Cavities. *Nano Lett.* **14**, 2854–2860 (2014).

56. V. Singh, *et al.*, Optomechanical coupling between a multilayer graphene mechanical resonator and a superconducting microwave cavity. *Nat. Nanotechnol.* **9**, 820–4 (2014).

57. J. Güttinger, *et al.*, Energy-dependent path of dissipation in nanomechanical resonators. *Nat. Nanotechnol.* **12**, 631–636 (2017).

58. A. Eichler, *et al.*, Nonlinear damping in mechanical resonators made from carbon nanotubes and graphene. *Nat. Nanotechnol.* **6**, 339–342 (2011).

59. R. J. Dolleman, D. Davidovikj, S. J. Cartamil-Bueno, H. S. J. Van Der Zant, P. G. Steeneken, Graphene Squeeze-Film Pressure Sensors. *Nano Lett.* **16**, 568–571 (2016).

60. D. Davidovikj, P. H. Scheepers, H. S. J. van der Zant, P. G. Steeneken, Static Capacitive Pressure Sensing Using a Single Graphene Drum. *ACS Appl. Mater. Interfaces* **9**, 43205–43210 (2017).

61. R. De Alba, *et al.*, Tunable phonon-cavity coupling in graphene membranes. *Nat. Nanotechnol.* **11**, 741–746 (2016).

62. R. De Alba, *et al.*, Temperature-dependence of stress and elasticity in wet-transferred graphene membranes. *J. Appl. Phys.* **123**, 095109 (2018).

63. F. Ye, J. Lee, P. X.-L. Feng, Electrothermally Tunable Graphene Resonators Operating at Very High Temperature up to 1200 K. *Nano Lett.* **18**, 1678–1685 (2018).

64. L. Ju, *et al.*, Photoinduced doping in heterostructures of graphene and boron nitride. *Nat. Nanotechnol.* **9** (2014).

65. Q. P. Unterreithmeier, T. Faust, J. P. Kotthaus, Damping of nanomechanical resonators. *Phys. Rev. Lett.* **105**, 1–4 (2010).

66. R. A. Barton, *et al.*, High, size-dependent quality factor in an array of graphene mechanical resonators. *Nano Lett.* **11**, 1232–1236 (2011).

67. M. Kumar, H. Bhaskaran, Ultrasensitive Room-Temperature Piezoresistive Transduction in Graphene-Based Nanoelectromechanical Systems. *Nano Lett.* **15**, 2562–2567 (2015).

68. Y. Oshidari, T. Hatakeyama, R. Kometani, S. Warisawa, S. Ishihara, High quality factor graphene resonator fabrication using resist shrinkage-induced strain. *Appl. Phys. Express* **5**, 117201 (2012).

69. D. Miller, B. Alemán, Shape tailoring to enhance and tune the properties of graphene nanomechanical resonators. *2D Mater.* **4** (2017).

70. D. Miller, A. Blaikie, B. Carter, B. Aleman, Engineering the Modal Shape of Graphene Nanoelectromechanical Systems Using Focused Ion Beam Milling. *2018 IEEE 13th Nanotechnol. Mater. Devices Conf.*, 1–4 (2018).

71. D. Miller, B. Alemán, Spatially resolved optical excitation of mechanical modesin graphene NEMS. *Appl. Phys. Lett.* **115**, 193102 (2019).

72. D. Miller, A. Blaikie, B. J. Alemán, Nonvolatile Rewritable Frequency Tuning of a Nanoelectromechanical Resonator Using Photoinduced Doping. *Nano Lett.* **20**, 2378–2386 (2020).

73. T. Wah, Vibration of Circular Plates. *J. Acoust. Soc. Am.* **34**, 275–281 (1962).

74. J. W. Suk, *et al.*, Transfer of CVD-grown monolayer graphene onto arbitrary substrates. *ACS Nano* **5**, 6916–6924 (2011).

75. J. S. Bunch, *et al.*, Impermeable Atomic Membranes from Graphene Sheets. *Nano Lett.* **8**, 2458–2462 (2008).

76. J. Gierak, Focused Ion Beam nano-patterning from traditional applications to single ion implantation perspectives. *Nanofabrication* **1**, 35–52 (2014).

77. D. Ramos, J. Tamayo, J. Mertens, M. Calleja, Photothermal excitation of microcantilevers in liquids. *J. Appl. Phys.* **99**, 124904 (2006).

78. B. Ilic, S. Krylov, K. Aubin, R. Reichenbach, H. G. Craighead, Optical excitation of nanoelectromechanical oscillators. *Appl. Phys. Lett.* **86**, 1–3 (2005).

79. D. Davidovikj, *et al.*, Visualizing the Motion of Graphene Nanodrums. *Nano Lett.* **16**, 2768–2773 (2016).

80. R. A. Barton, *et al.*, Photothermal self-oscillation and laser cooling of graphene optomechanical systems. *Nano Lett.* **12**, 4681–6 (2012).

81. C. Chen, *et al.*, Performance of monolayer graphene nanomechanical resonators with electrical readout. *Nat. Nanotechnol.* **4**, 861–867 (2009).

82. P. Weber, J. Güttinger, A. Noury, J. Vergara-Cruz, A. Bachtold, Force sensitivity of multilayer graphene optomechanical devices. *Nat. Commun.* **7**, 12496 (2016).

83. D. Davidovikj, M. Poot, S. J. Cartamil-Bueno, H. S. J. van der Zant, P. G. Steeneken, On-chip Heaters for Tension Tuning of Graphene Nanodrums. *Nano Lett.* **18**, 2852–2858 (2018).

84. B. Alemán, *et al.*, Polymer-free, low tension graphene mechanical resonators. *Phys. Status Solidi - Rapid Res. Lett.* **7**, 1064–1066 (2013).

85. C. H. Liu, I. S. Kim, L. J. Lauhon, Optical Control of Mechanical Mode-Coupling within a MoS2 Resonator in the Strong-Coupling Regime. *Nano Lett.* **15**, 6727–6731 (2015).

86. F. Schedin, *et al.*, Detection of individual gas molecules adsorbed on graphene. *Nat. Mater.* **6**, 652–655 (2007).

87. D. Karabacak, T. Kouh, K. L. Ekinci, Analysis of optical interferometric displacement detection in nanoelectromechanical systems. *J. Appl. Phys.* **98**, 1–9 (2005).

88. R. J. Dolleman, D. Davidovikj, H. S. J. van der Zant, P. G. Steeneken, Amplitude calibration of 2D mechanical resonators by nonlinear optical transduction. *Appl. Phys. Lett.* **111**, 253104 (2017).

89. D. Garcia-Sanchez, *et al.*, Imaging Mechanical Vibrations in Suspended Graphene Sheets. *Nano Lett.* **8**, 1399–1403 (2008).

90. C. C. Wu, Z. Zhong, Capacitive spring softening in single-walled carbon nanotube nanoelectromechanical resonators. *Nano Lett.* **11**, 1448–1451 (2011).

91. G. A. Steele, *et al.*, Strong Coupling Between Single-Electron Tunneling and Nanomechanical Motion. *Science* **325**, 1103–1107 (2009).

92. J. Chan, *et al.*, Laser cooling of a nanomechanical oscillator into its quantum ground state. *Nature* **478**, 89–92 (2011).

93. M. Li, H. X. Tang, M. L. Roukes, Ultra-sensitive NEMS-based cantilevers for sensing, scanned probe and very high-frequency applications. *Nat. Nanotechnol.* **2**, 114–20 (2007).

94. K. Y. Yasumura, *et al.*, Quality factors in micron- and submicron-thick cantilevers. *J. Microelectromech. Syst* **9**, 117–125 (2000).

95. X. Song, *et al.*, Stamp transferred suspended graphene mechanical resonators for radio frequency electrical readout. *Nano Lett.* **12**, 198–202 (2012).

96. C. Lee, X. Wei, J. W. Kysar, J. Hone, Measurement of the Elastic Properties and Intrinsic Strength of Monolayer Graphene. *Science* **321**, 385–388 (2008).

97. J. T. Robinson, *et al.*, Wafer-scale reduced graphene oxide films for nanomechanical devices. *Nano Lett.* **8**, 3441–3445 (2008).

98. J. Kotakoski, *et al.*, Toward Two-Dimensional All-Carbon Heterostructures via Ion Beam Patterning of Single-Layer Graphene. *Nano Lett.* **15**, 5944–5949 (2015).

99. C. Brand, *et al.*, An atomically thin matter-wave beamsplitter. *Nat. Nanotechnol.* **10**, 845–848 (2015).

100. A. Morin, *et al.*, FIB carving of nanopores into suspended graphene films. *Microelectron. Eng.* **97**, 311–316 (2012).

101. D. Lucot, *et al.*, Deposition and FIB direct patterning of nanowires and nanorings into suspended sheets of graphene. *Microelectron. Eng.* **86**, 882–884 (2009).

102. K. Matsui, *et al.*, Mechanical properties of few layer graphene cantilever.*2014 IEEE 27th Int. Conf. Micro Electro Mech. Syst.*, 1087–1090 (2014).

103. J. Hong, *et al.*, Origin of new broad Raman D and G peaks in annealed graphene. *Sci. Rep.* **3**, 2700 (2013).

104. B. Khanaliloo, *et al.*, Single crystal diamond nanobeam waveguide optomechanics. *Phys. Rev, X.* **5**, 041051 (2015).

105. R. B. Karabalin, M. C. Cross, M. L. Roukes, Nonlinear dynamics and chaos in two coupled nanomechanical resonators. *Phys. Rev. B* **79**, 165309 (2009).

106. W. J. Evans, L. Hu, P. Keblinski, Thermal conductivity of graphene ribbons from equilibrium molecular dynamics: Effect of ribbon width, edge roughness, and hydrogen termination. *Appl. Phys. Lett.* **96**, 203112 (2010).

107. T. Fang, A. Konar, H. Xing, D. Jena, Mobility in semiconducting graphene nanoribbons: Phonon, impurity, and edge roughness scattering. *Phys. Rev. B* **78**, 205403 (2008).

108. S. Y. Kim, H. S. Park, The importance of edge effects on the intrinsic loss mechanisms of graphene nanoresonators. *Nano Lett.* **9**, 969–974 (2009).

109. Z. Liao, *et al.*, Lateral damage in graphene carved by high energy focused gallium ion beams. *Appl. Phys. Lett.* **107**, 013108 (2015).

110. Q. Wang, *et al.*, Effects of Ga ion-beam irradiation on monolayer graphene. *Appl. Phys. Lett.* **103**, 1–5 (2013).

111. A. N. Abbas, *et al.*, Patterning, characterization, and chemical sensing applications of graphene nanoribbon arrays down to 5 nm using helium ion beam lithography. *ACS Nano* **8**, 1538–1546 (2014).

112. B. Sommer, *et al.*, Electron-beam induced nano-etching of suspended graphene. *Sci. Rep.* **5**, 7781 (2015).

113. A. C. Ferrari, *et al.*, Raman spectrum of graphene and graphene layers. *Phys. Rev. Lett.* **97**, 187401 (2006).

114. D. Karabacak, T. Kouh, K. L. Ekinci, Analysis of optical interferometric displacement detection in nanoelectromechanical systems. *J. Appl. Phys.* **98**, 1–4 (2005).

115. L. G. Villanueva, *et al.*, Nonlinearity in nanomechanical cantilevers. *Phys. Rev. B* **87**, 024304 (2013).

116. D. Antonio, D. H. Zanette, D. López, Frequency stabilization in nonlinear micromechanical oscillators. *Nat. Commun.* **3**, 806 (2012).

117. D. S. Greywall, B. Yurke, P. A. Busch, A. N. Pargellis, R. L. Willett, Evading amplifier noise in nonlinear oscillators. *Phys. Rev. Lett.* **72**, 2992–2995 (1994).

118. W. J. Venstra, H. J. R. Westra, H. S. J. Van Der Zant, Q-factor control of a microcantilever by mechanical sideband excitation. *Appl. Phys. Lett.* **99**, 2011–2013 (2011).

119. M. D. Dai, C.-W. Kim, K. Eom, Nonlinear vibration behavior of graphene resonators and their applications in sensitive mass detection. *Nanoscale Res. Lett.* **7**, 499 (2012).

120. D. Miller, B. Alemán, Shape tailoring to enhance and tune the properties of graphene nanomechanical resonators. *2D Mater.* **4**, 025101 (2017).

121. M. Will, *et al.*, High Quality Factor Graphene-Based Two-Dimensional Heterostructure Mechanical Resonator. *Nano Lett.* **17**, 5950–5955 (2017).

122. T. Larsen, *et al.*, Ultrasensitive string-based temperature sensors. *Appl. Phys. Lett.* **98**, 121901 (2011).

123. J. Moser, *et al.*, Ultrasensitive force detection with a nanotube mechanical resonator. *Nat. Nanotechnol.* **8**, 493–496 (2013).

124. L. G. Villanueva, S. Schmid, Evidence of Surface Loss as Ubiquitous Limiting Damping Mechanism in SiN Micro- and Nanomechanical Resonators. *Phys. Rev. Lett.* **113**, 227201 (2014).

125. G. Wang, *et al.*, Bending of Multilayer van der Waals Materials. *Phys. Rev. Lett.* **123**, 116101 (2019).

126. A. R. Ruyack, *et al.*, Graphene kirigami. *Nature* **524**, 204–207 (2015).

127. A. Kosmrlj, D. R. Nelson, Mechanical Properties of Warped Membranes. **012136**, 1–12 (2013).

128. R. J. T. Nicholl, *et al.*, The effect of intrinsic crumpling on the mechanics of free-standing graphene. *Nat. Commun.* **6**, 8789 (2015).

129. N. Lindahl, *et al.*, Determination of the Bending Rigidity of Graphene via Electrostatic Actuation of Buckled Membranes. *Nano Lett.* **12**, 3526–3531 (2012).

130. M. Will, *et al.*, High Quality Factor Graphene-Based Two-Dimensional Heterostructure Mechanical Resonator. *Nano Lett.* **17**, 5950–5955 (2017).

131. R. J. T. Nicholl, *et al.*, The effect of intrinsic crumpling on the mechanics of free-standing graphene. *Nat. Commun.* **6**, 8789 (2015).

132. C. Seoánez, F. Guinea, A. H. Castro Neto, Dissipation in graphene and nanotube resonators. *Phys. Rev. B - Condens. Matter Mater. Phys.* **76** (2007).

133. W. Bao, *et al.*, Controlled ripple texturing of suspended graphene and ultrathin graphite membranes. *Nat. Nanotechnol.* **4**, 562–566 (2009).

134. N. Clark, A. Oikonomou, A. Vijayaraghavan, Ultrafast quantitative nanomechanical mapping of suspended graphene. *Phys. Status Solidi Basic Res.* **250**, 2672–2677 (2013).

135. G. López-Polín, *et al.*, Increasing the elastic modulus of graphene by controlled defect creation. *Nat. Phys.* **11**, 26–31 (2015).

136. D. R. Nelson, L. Peliti, Fluctuations in Membranes With Crystalline and Hexatic Order. *J. Phys. Paris* **48**, 1085–1092 (1987).

137. J. T. Robinson, *et al.*, Graphene Strained by Defects. *ACS Nano* **11**, 4745–4752 (2017).

138. M. Yuan, M. A. Cohen, G. A. Steele, Silicon nitride membrane resonators at millikelvin temperatures with quality factors exceeding 108. *Appl. Phys. Lett.* **107** (2015).

139. K. Cao, *et al.*, Elastic straining of free-standing monolayer graphene. *Nat. Commun.* **11**, 1–7 (2020).

140. A. Castellanos-Gomez, *et al.*, Single-layer MoS2 mechanical resonators. *Adv. Mater.* **25**, 6719–6723 (2013).

141. S. J. Cartamil-Bueno, *et al.*, Mechanical characterization and cleaning of CVD single-layer h-BN resonators. *npj 2D Mater. Appl.* **1**, 16 (2017).

142. A. Castellanos-Gomez, *et al.*, Single-layer MoS2 mechanical resonators. *Adv. Mater.* **25**, 6719–6723 (2013).

143. A. Stark, *et al.*, Neutral mass spectrometry of virus capsids above 100 megadaltons with nanomechanical resonators. *Science* **922**, 918–922 (2018).

144. C. Schwarz, *et al.*, Deviation from the Normal Mode Expansion in a Coupled Graphene-Nanomechanical System. *Phys. Rev. Appl.* **6**, 064021 (2016).

145. M. Vassalli, V. Pini, B. Tiribilli, Role of the driving laser position on atomic force microscopy cantilevers excited by photothermal and radiation pressure effects. *Appl. Phys. Lett.* **97**, 1–4 (2010).

146. C. Schwarz, "Ph.D. thesis, Université Grenoble Alpes, France." (2017).

147. Z. Wang, *et al.*, Black phosphorus nanoelectromechanical resonators vibrating at very high frequencies. *Nanoscale* **7**, 877–884 (2015).

148. Z. Wang, *et al.*, Resolving and Tuning Mechanical Anisotropy in Black Phosphorus via Nanomechanical Multimode Resonance Spectromicroscopy. *Nano Lett.* **16**, 5394–5400 (2016).

149. I. Bargatin, I. Kozinsky, M. L. Roukes, Efficient electrothermal actuation of multiple modes of high-frequency nanoelectromechanical resonators. *Appl. Phys. Lett.* **90**, 10–13 (2007).

150. J. Cha, C. Daraio, Electrical tuning of elastic wave propagation in nanomechanical lattices at MHz frequencies. *Nat. Nanotechnol.* **13**, 1016–1020 (2018).

151. D. Hatanaka, I. Mahboob, K. Onomitsu, H. Yamaguchi, Phonon waveguides for electromechanical circuits. *Nat. Nanotechnol.* **9**, 520–4 (2014).

152. J. D. Teufel, *et al.*, Circuit cavity electromechanics in the strong-coupling regime. *Nature* **471**, 204–208 (2011).

153. L. Laurent, J.-J. Yon, J.-S. Moulet, M. Roukes, L. Duraffourg, 12-μm-Pitch Electromechanical Resonator for Thermal Sensing. *Phys. Rev. Appl.* **9**, 024016 (2018).

154. A. Yao, T. Hikihara, Logic-memory device of a mechanical resonator. *Appl. Phys. Lett.* **105**, 123104 (2014).

155. S. Masmanidis, *et al.*, Multifunctional Nanomechanical Systems via Tunably Coupled Piezoelectric Actuation. *Science* **317**, 780–783 (2007).

156. M. A. A. Hafiz, L. Kosuru, M. I. Younis, Towards electromechanical computation: An alternative approach to realize complex logic circuits. *J. Appl. Phys.* **120** (2016).

157. M. L. Roukes, Mechanical compution, redux? *IEDM Tech. Dig. IEEE Int. Electron Devices Meet. 2004.*, 539–542 (2004).

158. R. H. Olsson III, I. El-Kady, Microfabricated phononic crystal devices and applications. *Meas. Sci. Technol.* **20**, 012002 (2009).

159. Y. Wang, *et al.*, Observation of Nonreciprocal Wave Propagation in a Dynamic Phononic Lattice. *Phys. Rev. Lett.* **121**, 194301 (2018).

160. J. Cha, K. W. Kim, C. Daraio, Experimental realization of on-chip topological nanoelectromechanical metamaterials. *Nature* **564**, 229–233 (2018).

161. F. C. Hoppensteadt, E. M. Izhikevich, Synchronization of MEMS resonators and mechanical neurocomputing. *IEEE Trans. Circuits Syst. I Fundam. Theory Appl.* **48**, 133–138 (2001).

162. A. Kumar, P. Mohanty, Autoassociative Memory and Pattern Recognition in Micromechanical Oscillator Network. *Sci. Rep.* **7**, 1–9 (2017).

163. W.-M. Zhang, K.-M. Hu, Z.-K. Peng, G. Meng, Tunable Micro- and Nanomechanical Resonators. *Sensors (Basel).* **15**, 26478–566 (2015).

164. E. Merced, R. Cabrera, N. Dávila, F. E. Fernández, N. Sepúlveda, A micro-mechanical resonator with programmable frequency capability. *Smart Mater. Struct.* **21** (2012).

165. M. Chiao, L. Lin, Post-packaging frequency tuning of microresonators by pulsed laser deposition. *J. Micromechanics Microengineering* **14**, 1742–1747 (2004).

166. S. Enderling, *et al.*, Characterization of frequency tuning using focused ion beam platinum deposition. *J. Micromechanics Microengineering* **17**, 213–219 (2007).

167. K. Kim, K. Jensen, A. Zettl, Tuning nanoelectromechanical resonators with mass migration. *Nano Lett.* **9**, 3209–3213 (2009).

168. J. Chang, *et al.*, Synthesis and bidirectional frequency tuning of cantilever-shape nano resonators using a focused ion beam. *ACS Appl. Mater. Interfaces* **5**, 9684–9690 (2013).

169. L. Ju, *et al.*, Photoinduced doping in heterostructures of graphene and boron nitride. *Nat. Nanotechnol.* **9**, 348–352 (2014).

170. Y. D. Kim, *et al.*, Focused-Laser-Enabled p–n Junctions in Graphene Field-Effect Transistors. *ACS Nano* **7**, 5850–5857 (2013).

171. H. H. Choi, *et al.*, Photoelectric Memory Effect in Graphene Heterostructure Field-Effect Transistors Based on Dual Dielectrics. *ACS Photonics* **5**, 329–336 (2018).

172. C. Neumann, *et al.*, Spatial Control of Laser-Induced Doping Profiles in Graphene on Hexagonal Boron Nitride. *ACS Appl. Mater. Interfaces* **8**, 9377–9383 (2016).

173. J. Velasco, *et al.*, Nanoscale Control of Rewriteable Doping Patterns in Pristine Graphene/Boron Nitride Heterostructures. *Nano Lett.* **16**, 1620–1625 (2016).

174. D. Hatanaka, A. Bachtold, H. Yamaguchi, Electrostatically Induced Phononic Crystal. *Phys. Rev. Appl.* **11**, 024024 (2019).

175. I. Mahboob, H. Yamaguchi, Bit storage and bit flip operations in an electromechanical oscillator. *Nat. Nanotechnol.* **3**, 275–279 (2008).

176. W. W. Koelmans, *et al.*, Projected phase-change memory devices. *Nat. Commun.* **6**, 8181 (2015).

177. L. Wang, *et al.*, Monolayer hexagonal boron nitride films with large domain size and clean interface for enhancing the mobility of graphene-based field-effect transistors. *Adv. Mater.* **26**, 1559–1564 (2014).

178. J. Lee, M. J. Krupcale, P. X. L. Feng, Effects of γ-ray radiation on two-dimensional molybdenum disulfide (MoS2) nanomechanical resonators. *Appl. Phys. Lett.* **108** (2016).

179. P.-H. Ho, *et al.*, Precisely Controlled Ultrastrong Photoinduced Doping at Graphene-Heterostructures Assisted by Trap-State-Mediated Charge Transfer. *Adv. Mater.* **27**, 7809–7815 (2015).

180. A. L. Yeats, *et al.*, Persistent optical gating of a topological insulator. *Sci. Adv.* **1**, e1500640 (2015).

181. R. J. T. Nicholl, N. V Lavrik, I. Vlassiouk, B. R. Srijanto, K. I. Bolotin, Hidden Area and Mechanical Nonlinearities in Freestanding Graphene. **266101**, 1–6 (2017).

182. G. López-Polín, *et al.*, Increasing the elastic modulus of graphene by controlled defect creation. *Nat. Phys.* **11**, 26–31 (2014).

183. A. Reserbat-Plantey, *et al.*, Strain Superlattices and Macroscale Suspension of Graphene Induced by Corrugated Substrates. *Nano Lett.* **14**, 5044–5051 (2014).